INFORMATION TO USERS

This manuscript has been reproduced from the microfilm master. UMI films the text directly from the original or copy submitted. Thus, some thesis and dissertation copies are in typewriter face, while others may be from any type of computer printer.

The quality of this reproduction is dependent upon the quality of the copy submitted. Broken or indistinct print, colored or poor quality illustrations and photographs, print bleedthrough, substandard margins, and improper alignment can adversely affect reproduction.

In the unlikely event that the author did not send UMI a complete manuscript and there are missing pages, these will be noted. Also, if unauthorized copyright material had to be removed, a note will indicate the deletion.

Oversize materials (e.g., maps, drawings, charts) are reproduced by sectioning the original, beginning at the upper left-hand corner and continuing from left to right in equal sections with small overlaps. Each original is also photographed in one exposure and is included in reduced form at the back of the book.

Photographs included in the original manuscript have been reproduced xerographically in this copy. Higher quality 6" x 9" black and white photographic prints are available for any photographs or illustrations appearing in this copy for an additional charge. Contact UMI directly to order.

UMI

BLACK CARBON: ATMOSPHERIC MEASUREMENTS AND RADIATIVE EFFECT

By

Linhong Kou

Canada

DALHOUSIE UNIVERSITY

FACULTY OF GRADUATE STUDIES

The undersigned hereby certify that they have read and recommend to the Faculty of

Graduate Studies for acceptance a thesis entitled   "Black Carbon: Atmospheric

Measurements and Radiative Effect"

by _____ Linhong Kou

in partial fulfillment of the requirements for the degree of Doctor of Philosophy.

Dated: ____ October 30, 1996

External Examiner

Research Supervisor

Examining Committee
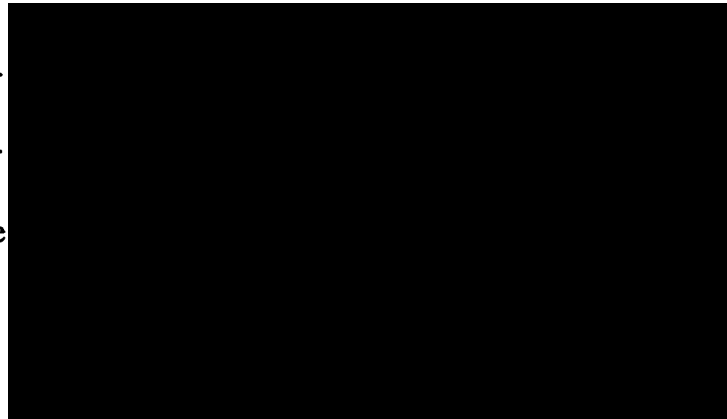
DALHOUSIE UNIVERSITY

Date: **October, 1996**
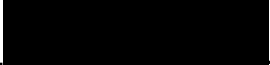
Author: **Linhong Kou**

Title: **Black Carbon: Atmospheric Measurements and Radiative Effect**

Department: **Physics**

Degree: **Ph.D.**   Convocation: **May**   Year: **1997**

Permission is herewith granted to Dalhousie University to circulate and to have copied for non-commercial purposes, at its discretion, the above title upon the request of individuals or institutions.

_____
Signature of Author

iii

To my parents, Zhongquan Kou and Peiqiu Liu.
You listen, you love, you care...

敬献给亲爱的父母亲，寇忠权和刘佩秋。

我身上还留有您们的体温，
我脉搏里奔腾着您们的血液，
我性格上烙有您们的印记，
我思想里有您们的智慧......

Contents

List of Tables

List of Figures

xii

Abstract

Atmospheric black carbon concentrations have been measured in air, cloud, rain and snow samples collected over Nova Scotia during the Radiation, Aerosol, Cloud Experiment (RACE) of 1995. Atmospheric aerosol samples for black carbon analyses were collected by filtering a known amount of air or liquid dispersons (cloud water, rain or melted snow) through quartz filters, and the filters were later subjected to thermo-optical analyses for black carbon determination. The average black carbon atmospheric concentration found in air was $0.13\pm0.01\mu g/m^3$ at an altitude between 100 and 1700m; $0.22\pm0.02\mu g/m^3$ at near-sea surface; and $0.54\pm0.03\mu g/m^3$ in summer and $1.69\pm0.08\mu g/m^3$ in winter over Halifax area. The black carbon to SO_4^{-2} mass mixing ratio was found to be 14% over all the samples collected during RACE and the typical black carbon mass fraction in total aerosol is 1-2%. About 6% of black carbon was in the form of an internal mixture inside cloud droplets. The average black carbon content found in cloud water was about $26\pm3\mu g/kg$. The average black carbon content was $3.2\pm0.2\mu g/kg$ in rain, and $8.8\pm0.4\mu g/kg$ in snow over all the samples collected in both rural and urban areas.

The radiative effect of black carbon is discussed in the present study. The black carbon radiative effect is significant compared with sulfate aerosol effect. Black carbon aerosols act to reduce the cooling effect of sulfate aerosols. The reduction of the cooling depends on both the black carbon fraction and the surface albedo. For instances of high surface albedo or high black carbon loading a net heating can result. The results for the Quebec forest fire day show that the black carbon aerosol decreases the sulfate aerosol cooling effect by 20 to 50%. The impact of black carbon aerosol on the radiative properties of clouds is insignificant over the Nova Scotia region.

List of Symbols

A   -   absorbtance of cloud

B   -   back sattering fraction of aerosols

F   -   flux of radiation

ΔF   -   radiative forcing

g   -   asymmetry parameter

G   -   integrated asymmetry parameter

I   -   intensity of radiation

K_{abs} -   absorption coefficient

K_{ext} -   extinction coefficient

K_{sca} -   scattering coefficient

L   -   aerosol loading

M   -   mass density

m_i -   imaginary part of the refractive index

m_r -   real part of the refractive index

n(r)   -   Size distribution

N_c -   fractional cloud cover

ω -   single scattering albedo

Ω -   solid angle

R_a -   albedo of earth-atmosphere-aerosol system

R_s -   surface albedo

r	-	particle radius
r_g	-	geometric mean radius of the size distribution
r_{eff}	-	effective radius
S_o	-	solar constant
T_a	-	atmospheric transmittance
Θ	-	solar zenith angle
θ	-	scattering angle
σ	-	standard deviation in the log-normal distribution
σ_{abs}	-	absorption cross section
σ_{ext}	-	extinction cross section
σ_{sca}	-	scattering cross section
τ	-	optical depth
Ψ_{abs}	-	specific absorption coefficient
Ψ_{abs}	-	specific extinction coefficient
Ψ_{abs}	-	specific scattering coefficient
ΔZ	-	aerosol layer depth

Acknowledgements

Thanks goes to Regine Maass, Alex Feargrieve, Jim Chisholm, Andy George, Ralph Deveau, Barbara Winter, Dr. Muyin Wang, Steven Dobbie, Peter Damiano, Jeff Jardine, Dr. Owen Hertzman, and Dr. Qiang Fu for the help they gave to me during the past several years. I have been blessed by having all these wonderful people around me. Space prohibits me from listing the details. Thank you all!

Grateful acknowledgement is also give to the staff and faculty of the physics department of Hebei University, and Beijing Polytechnic University for the excellent education I obtained in China. I also like to thank the teachers in Weishui Middle school, China, where I initiated an appreciation for physics elegance.

Finally, I would like to thank my husband, Bing Xiao, for his love, understanding, patience, encouragement, and support. He deserves half of the credit I got in my academic career. I also thank my brother, Linsong Kou and his wife Hongmei Ni for their enthusiastic encouragment for my work. It gives me the greatest pride and pleasure to dedicate this manuscript to my parents.

Chapter 1

Introduction

Aerosol particles play an important role in climate change. They exert a direct radiation effect on climate through their interaction with solar and terrestrial radiation, and an indirect effect through their function as cloud condensation nuclei. In the direct radiative aerosol effect the interaction with solar radiation dominates over the terrestrial radiation.

Aerosol both absorbs and scatters the solar radiation. The global aerosol effect on climate depends on the ratio of aerosol absorption to the fraction of the radiation scattered to the upper hemisphere (Chylek and Coakley, 1974; Coakley and Chylek 1975). Most of the natural and man made aerosols are only slightly absorbing at solar wavelengths. Such aerosols tend to cool the global climate. Only black carbon (soot) and to a lesser extend some clays and minerals (hematite) absorb solar radiation in a significant manner. The dominant aerosol component responsible for absorption of solar radiation in the earth's atmosphere is black carbon under most

conditions (Pinnick et al., 1993; Hansen et al., 1993; Warren and Clark, 1990; Heintzenberg, 1982; Weiss and Waggoner, 1982). This property of black carbon may lead to influences on regional climate through warming of the atmosphere, reduction in the amount of the solar radiation reaching the ground, and the albedo of clouds and snow. Therefore black carbon plays a key role in radiative transfer in the atmosphere and has resulting climatic effects (Ackerman and Toon, 1981; Hansen et al, 1980).

Natural sources of black carbon have probably decreased during the past hundred years due to forest fire suppression activities. On the other hand the anthropogenic sources have increased significantly mainly due to fossil fuel and biomass burning. Comparison of black carbon concentration in the recent and several thousand years old ice cores (Chylek et al., 1995a) suggests that the total amount of black carbon transported to polar regions has not changed by more than a factor of two within the last several thousand years. This indicates at least some compensating effect between fire suppression activities and fossil fuel and biomass burning.

To evaluate the possible impact of black carbon on climate, an understanding of its sources and global distribution through the atmosphere is required (Penner et al. 1993; Chylek and Wong, 1995). Although there have been several measurements of atmospheric black carbon concentrations (Rosen et al., 1981; Heintzenberg, 1982; Ogren and Charlson, 1983; Ohta and Okita 1984; Cass et al., 1984; Chuan and Woods, 1984, Shah et al, 1986; Hansen et al., 1988; Larson

et al., 1989; Pinnick et al., 1993; Chylek et al., 1996) the observational data are far from complete and no clear global or regional picture can be yet deduced.

The goals of the present work are to contribute to the pool of available data on the black carbon global distribution, and to evaluate the possible radiative effects on the earth-atmosphere radiation balance with the measured amount of black carbon loading over the Nova Scotia region. Since any significant radiative effect of black carbon aerosol will occur in the solar spectral region rather than the terrestrial spectrum, the radiative effect discussion in the present study is restricted to the solar spectral region (wavelength range of 0.3 to 4.0μm).

After a brief review of what is presently known about black carbon in Chapter 2, Chapter 3 provides a detailed description of the measurements of atmospheric black carbon distribution including sample collection and black carbon analyses. The results obtained from the measurements are used in a radiation model in Chapter 4 to estimate the radiative effect of black carbon aerosols. In Chapter 5, the impact of black carbon on the radiative properties of clouds is examined. Finally in Chapter 6 conclusions drawn from this study are summarized.

Chapter 2

Black Carbon aerosols

2.1 Background of Black Carbon Aerosol

The main sources of black carbon in the atmosphere are forest fires and anthropogenic combustion processes such as power generation, vehicular emission, residential heating and biomass burning.

The total amount of black carbon released to the atmosphere from all sources is estimated to be (Crutzen and Andreae, 1990) around 6 - 30×10^{12} g per year, with approximately half of this amount released by biosphere burning (including forest fires) and half by fossil fuels.

Aside from the climatic effect caused by its high specific absorption in the visible spectrum, black carbon has a chemical importance as well. Because of its low reactivity, black carbon is inert in the atmosphere and remains chemically unchanged for a long period of time even when mixed with other compounds. Wet and dry deposition are the main sinks of black carbon in the atmosphere. Due to its hydrophobic character, the fine particulate (less than $1 \mu m$ in size) black carbon in the atmosphere is less effectively scavenged

by precipitation which is the main removal mechanism for fine particles. Hence, in the absence of physical removal mechanisms, this fine fraction of black carbon can be transported over large distances and have long residence times in the atmosphere. However, there is considerable uncertainty in the residence time of fine black carbon particles in the atmosphere. Though no direct measurements of the black carbon atmospheric lifetimes are available, Smoke from forest fires is known to propagate through the atmosphere for at least a few days. The fact that black carbon is found in polar regions suggests an atmospheric life time of at least a week or more. The chemical stability of black carbon might make it useful as an inert tracer for air masses that originate near combustion sources.

Black carbon aerosols have large surface area. They offer an airborne surface for adsorption of other trace atmospheric species and condensation processes and surface reactions such as the formation of major air pollutant sulfates through the catalytic oxidation of SO_2 (Benner et al., 1982).

2.2 Previous Measurements of Atmospheric Black Carbon

2.2.1 Black Carbon Concentration in Air

Determination of the distribution of black carbon in the atmosphere is necessary to understand the transport and life cycle of black carbon aerosol. A number of quantitative measurements of black carbon concentration from various locations can be found in the literature and are listed in Table 2.1. It has become evident that black carbon aerosols, emitted from combustion, can be carried very far from source regions. They are found all over the globe, not only in urban air, but also in remote areas. Typical concentrations of black carbon range from 3-10 $\mu g/m^3$ in urban areas, to $0.1\text{-}1\mu g/m^3$ in rural areas, to $0.001\text{-}0.1\mu g/m^3$ in remote regions. The highest concentrations ($\sim 20\mu g/m^3$) occur over densely populated continental regions, and the mass fraction of black carbon in urban aerosols is typically a few percent (Heintzenberg and Winkler, 1984a).

Table 2.1 Previous measurements of atmospheric black carbon concentrations at various locations (BC)

Site Classification	Location	Reference	Concentration of BC ($\mu g/m^3$)
Urban	Detroit, MI	Dasch & Cadle, 1989	2.2
Urban	Newark, NJ	Gaffiney et al., 1984	3.5
Urban	Denver, CO	Countess et al., 1980	6.6
Urban	Los Angeles, CA	Cass et al., 1984	6.4
Urban	Ave of 46 urban sites	Shah et al., 1986	3.8
Urban	Pasadena, CA	Larson et al., 1989	3.95
Urban	Athens, GR	Valaoras et al.,1988	10.7
Urban	Beijing, China	Parungo et al., 1994	5.1
Urban	Sapporo, Japan	Ohta & Okita, 1984	5.1
Urban	Paris, FR	Cachier et al., 1989	4.6
Urban	Hamburg, RDA	Heintzenberg et al.,1984a	2.4
Urban	Ohio River Valley	Huntzicker et al., 1986	1.5
Urban	Dearborn, MI	Adams et al., 1989	1.2
Rural	Ave 20 sites in USA	Shah et al., 1986	1.3
Rural	Northern MI	Cadle and Dasch, 1988	0.6
Rural	Lewes, DE	Wolff et al., 1986	1.2
Rural	Southwestern PA	Keeler et al., 1990	1.3
Rural	Barrow, AK	Bodhaine et al., 1989	0.1-0.2
Remote	North Atlantic, Canada	Chylek et al., 1996	0.11
Remote	Alert, Canada	Hopper et al., 1994	0.3
Remote	Orogrande, New Mexico	Pinnick et al., 1993	0.15
Remote	Arctic	Clarke & Noone, 1985	0.2
Remote	Arctic	Rosen et al., 1981	0.3
Remote	Arctic	Heintzenberg, 1982	0.07
Remote	South pole	Hansen et al., 1988	0.0001- 0.002
Remote	Central Pacific Ocean	Clarke, 1989	0.0015

2.2.2 Black Carbon Content in Cloud Water, Rain and Snow

Black carbon effects on climate not only depend on the amount of black carbon injected into the atmosphere but also on the rate at which it is removed. Larger particles, which are greater than a few microns in diameter, are effectively removed by sedimentation, and wet deposition is the dominant removal mechanism for black carbon aerosols under most conditions (Ogren and Charlson, 1983; Cadle and Dasch, 1988). It is widely recognized that the efficiency of wet deposition depends on the hygroscopic properties of the aerosols which are determined by the chemical composition and the surface structure of individual aerosols. Freshly emitted black carbon particles are expected to be hydrophobic and not likely to be cloud condensation nuclei (CCN) by themselves, but they may increase in hygroscopicity if they become coated with some substances such as sulfate (SO_4^{2-}). Hence they can become efficient CCN and subsequently be removed by precipitation. Diffusion to and collision with cloud and rain droplets are other pathways by which black carbon is incorporated into precipitation. Indeed black carbon has been observed in cloud and rain droplets. Table 2.2a, and 2.2b list some of the published measurements of black carbon content in precipitation and cloud water. The values vary from a few micrograms to hundreds of micrograms of black carbon per kilogram of precipitation.

Table 2.2a Previous measurements of black carbon content in precipitation (rain & snow)

Sample Classi- fication	Location	Reference	Concentration of BC (μg/l)
Rain	Seattle & Sweden	Ogren et al., 1983	100 (20 - 600)
Snow	Cascade Mountains, Washington,	Grenfell et al., 1981	(22-59)
Snow	South New Mexico & West Texas	Chylek et al., 1987	(4.9-15.9)
Snow	Northern MI	Cadle & Dash, 1988	72 (28-210)
Snow	Detroit, MI	Dasch & Cadle, 1989	160
Snow	Antarctic	Warren & Clarke, 1990	0.2
Snow	Arctic	Clarke & Noone, 1985	25 (0.6-127)
Ice core	Greenland (89-90 snow)	Chylek et al., 1995a	2.0
Ice core	Greenland (320-330AD)	Chylek et al., 1995a	2.1
Ice core	Greeland Dye-3	Chylek et al., 1992	1.5

( )- data range

Table 2.2b Previous measurements of black carbon content in cloud water

Sampling Site	LWC g/m^3	Reference	Concentration of BC (μg/l)
Eastern Pacific	0.24-0.31	Twohy, et al., 1989	23-79
Aereskutan,Sweden		Heinzenberg, 1988	100
North Atlantic, Canada	0.16-0.27	Chylek et al., 1996	40 (10-60)

2.2.3 Scavenging Ratios

An assessment of the removal of atmospheric black carbon to cloud or snowpack is expressed by the scavenging ratio. The scavenging ratio is defined as the mass mixing ratio of black carbon in precipitation (cloud water, melted snow water) divided by the mass mixing ratio of black carbon in air (Warren & Clarke, 1990; Penner et al. 1993). Table 2.3 lists some reported scavenging ratios. Since black carbon incorporated into cloud or snowpack must originate in the atmosphere, a relationship between these two concentrations is expected.

Table 2.3   Previously   reported Scavenging Ratio

Location	Reference	Scavenging Ratio
Northern MI (snow)	Cadle & Dasch, 1988	160 (49-1260)
Detroit, MI (snow)	Dasch & Cadle, 1989	250 (6-890)
Detroit, MI (rain)	Dasch & Cadle, 1989	180 (18-650)
Antarctic(snow)	Warren & Clarke, 1990	150
Abisko,Sweden (snow) (Arctic)	Clarke, 1989	100 (60-160)
North Atlantic (cloud)	Chylek et al., 1996	108-1075

( )- data range

2.3 Refractive Index of Black Carbon Aerosol

2.3.1 Refractive Index of Black Carbon Particle

The optical properties of a particle depend on its size, shape and its complex refractive index. The complex refractive index of a given material is denoted $m = m_r - im_i$, where the real part, m_r, is a measure of the refraction of light entering a material, and the imaginary part, m_i, characterizes the amount of absorption of light by the material. Previous measurements of the refractive index of black carbon can be divided into three categories: (1) scattering and extinction measurements in flames (Vaglieco et al, 1990; Bockhorn, et al, 1981; Lee and Tien, 1981; Chippet and Gray, 1978; Charalampopoulos & Felske, 1987); (2) specular reflectance of light by a surface of black carbon pellets (Stagg and Charalampopoulos, 1993; Dalzell and Sarofim, 1969; Mullins and Williams, 1987); and (3) light attenuation by a dispersion of black carbon particles in liquid (d'Alessio et al., 1977).

The refractive index of black carbon in the visible region obtained by a number of investigators is given in Table 2.4. Few measurements have been made at infrared wavelengths (Foster and Howarth, 1967; Dalzell and Sarofim, 1969; Lee and Tien, 1981). A large range of reported values can be seen in Table 2.4. The real part of the refractive index varies between 1.5 and 2.0 and the imaginary part varies between 0.4 and 0.8 in visible wavelengths.

These values depend on both the original form of the burned material and on the burning process itself (Charalampopoulos et al., 1989; Bockhorn, et al, 1981; Dalzell and Sarofim, 1969). A commonly adopted black carbon index used for numerical calculations is m=1.75-0.44i (Chylek et al., 1995; d'Almeida et al., 1991). Which will be used in later calculations.

Table 2.4 Previous measurements of complex Refractive Index of Black Carbon

$\lambda_0(\mu m)$	m_r	m_i	Reference
visible	1.9	0.55	Vaglieco et al, 1990
0.567	1.54	0.37	Stagg & Charalampopoulos,1993
0.633	1.1	0.37	Bockhorn, et al, 1981
0.55	1.57	0.53	Dalzell, & Sarofim, 1969
visible	1.9 ± 0.1	0.55 ± 0.1	Lee & Tien, 1981
visible	1.9 ± 0.1	0.35 ± 0.05	Chippet & Gray, 1978
0.488	1.6	0.59	Charalampopoulos & Felske, 1987
visible	1.8 - 1.95	0.5-0.8	Mullins & Williams, 1987

λ_0 -- center wavelength

m_r -- real part of the refractive index

m_i -- imaginary part of the refractive index

2.3.2 Refractive index of black-carbon-containing aerosols

As a result of coagulation, gas-to-particle conversion, and the multitude of the sources in the atmosphere, some degree of internal mixing of black carbon with other compounds can be expected (Pinnick et al., 1993; Ogren & Charlson, 1984). The chemical composition of a black-carbon-containing aerosol depends on the source and on the processes that contribute to its formation.

Since anthropogenic sulfate aerosols are produced mostly by gas-to-particle conversion of sulfur-containing gases which are released in to the atmosphere primarily through fossil fuel burning, there is a very high chance for anthropogenic sulfate aerosol and black carbon to be mixed. High correlations of sulfate aerosol and black carbon aerosol concentrations have been reported (Ogren & Charlson, 1984; Cadle & Dasch, 1988; Pinnick et al., 1993; Chylek et al., 1996). Further evidence for the mixing of sulfates and black carbon has also been found in analyses of impactor samples by X-ray dispersion electron microscopy (Pinnick et al., 1993). Table 2.5 shows some of the measured mass mixing ratios of black carbon to sulfate in air, snow and rain.

Table 2.5   Previous measurements of mass mixing ratios of BC/SO_4^{2-} in air, snow and rain

Location	Reference	BC $\mu g/m^3$	SO_4^{2-} $\mu g/m^3$	Ratio %
Northern MI	Cadle & Dasch, 1988	0.6	2.59	23
Southwestern PA	Keeler, 1990	1.3	19.3	6.7
36 continental sites in US	Sisler & Malm, 1994			16
K-puszta, Hungarian	Heintzenberg, 1985	0.8	3.2	25
North Atlantic, Canada	Chylek et al., 1996	0.11	2.65	4
Sweden (rain)	Ogren & Charlson, 1984			7
Northern MI (snow)	Cadle & Dasch, 1988	72 $\mu g/l$	1070 $\mu g/l$	6.7

The refractive index   of a two-component mixture   can be   estimated by using the Bruggeman effective medium approximation (Chylek et al., 1995b; Chylek et al., 1983), which is expressed by the following formula,

$$v_0 \frac{m_o^2 - m_e^2}{m_o^2 + 2m_e^2} + v_A \frac{m_A^2 - m_e^2}{m_A^2 + 2m_e^2} = 0 \qquad (2\text{-}1)$$

where m_e is the effective refractive index of the composite material, m_0 and m_A are the complex refractive indices of a nonabsorbing matrix   and absorbing inclusions   respectively,   and v_0 and v_A are corresponding volume fractions with $v_0 + v_A = 1$.

2.4 Size Distribution of Black Carbon Aerosols

The size distribution of aerosols plays a sensitive role in their optical properties. In order to evaluate the contribution of black carbon aerosols to the radiation budget, it is important to have information on their size distribution. However few measurements of black carbon particle size distributions in the atmosphere have been made. One difficulty is that the size distributions of black carbon aerosols are influenced by the nature of the sources, the fuel, the type of combustion, dilution factors, residence time and condensation processes of the particles.

Among the few published investigations on black carbon size distributions, Heintzenberg and Winkler (1991) and Heintzenberg and Covert (1984) have reported that at the rim of the combustion zone, very high concentrations of primary black carbon particles occur with radii below $0.01\mu m$. These particles rapidly coagulate forming atmospheric black carbon particles with a mass mean size lying mostly between 0.2 to $0.4\mu m$.

One measurement of black carbon aerosols in the lower stratosphere and upper troposphere at an altitude of 11km shows the size distribution of black carbon aerosols to be represented by a log-normal distribution with a geometric mean radius of $0.07\mu m$ and a standard deviation of 1.5 (Pusechel et al., 1992).

A black carbon size measurement carried out in urban areas of Italy shows that the regression of the data to a log-normal function yields a geometric mean radius of $0.037\mu m$ and a standard deviation of 1.87 (Chylek, 1996).

Based on available information, most black carbon aerosols in the atmosphere appear to have a mean size in the range of $0.1\text{-}0.5\mu m$ (Clarke et al, 1987; Whitby, 1979; McMurry and Zhang, 1989). For the purpose of numerical calculations, a log-normal distribution function can be used for the black carbon aerosol size distribution with a geometric mean radius, r_g, in the range of $0.05\text{-}0.3\mu m$ and a standard deviation about 1.5. Written in terms of number density per radius interval, the log-normal distribution is commonly expressed as

$$n(r) = \frac{N_0}{r \ln\sigma \sqrt{2\pi}} \exp\left[-\frac{(\ln r - \ln r_g)^2}{2\ln^2\sigma}\right] \qquad (2\text{-}2)$$

where, r is the radius of the particle in units of μm; N_0 is the total number density in units of particle number per cm^3; r_g is the geometric mean radius; σ is the standard deviation; $n(r)$ is the size distribution in units of particle number per cm^3 per μm.

Chapter 3

Experimental Measurements

The usual method of quantitatively determining the amount of black carbon in the atmosphere involves collecting black carbon on a filter, either in gaseous or liquid dispersions, and then measuring light transmittance of the filter (Malissa et al.1976; Chylek et al., 1987; Chylek et al., 1992). In our measurement, a quartz filter (QAO-2500, Pallflex Products Corperation) is used for filtration. It is heated in an electric furnace at 700°C for two hours before sampling to remove carbonaceous contamination. In order to get a relatively clear understanding of black carbon distributions throughout the atmosphere, samples over a wide range of sources including air, cloud, rain, and snow in different locations have been collected. Table 3.1 shows a list of our sampling.

3.1 Field Measurements - Sample Collection

3.1.1 Radiation, Aerosol and Cloud Experiment (RACE)

Organized by the Atmospheric Environment Service (AES), the Radiation, Aerosol and Cloud Experiment (RACE) was carried out from August 13 to September 9, 1995, and based in Greenwood, Nova Scotia. The airborne observations were conducted near and in marine stratus clouds over the Gulf of Maine and Bay of Fundy. The primary objective of RACE was to improve the understanding of processes involving the interaction between aerosols and low stratiform clouds by gathering quantitative information on cloud microphysics, cloud radiative properties, and aerosol particles. Five observational platforms were used in this experiment. The first two were on aircrafts: the National Research Council (NRC) of Canada

Table 3.1 Sampling List

Sample type	Site class- fication	Season	Height	Sample number
Air	urban	s	ground	1 5
Air	urban	w	ground	1 3
Rain	urban	s	ground	1 0
Rain	urban	w	ground	5
snow	urban	w	ground	1 1
Rain	rural	s	ground	2 3
snow	rural	w	ground	3
Air	remote	s	0.1-2km	1 6
Air	remote	s	near sea surface	1 3
C water	remote	s	0.3-2.5km	1 5

Note: C water-cloud water
        s-summer
        w-winter

Convair 580 and DHC-6 Twin Otter; the other two were on the Ferries: the Bluenose and Prince of Fundy; and the last one was on a ground site near Yarmouth Lighthouse. Both aircrafts were equipped with instrumentation for cloud microphysical measurements, measurements of the concentration of atmospheric aerosol constituents and important trace gases, and for the collection of cloud water. All the samples for black carbon studies were collected from the Twin Otter airplane and the Bluenose Ferry.

3.1.1 A) Air Sampling from the Twin Otter

Aerosol sampling for black carbon studies was performed from the NRC DHC-6 Twin Otter aircraft, with an operating airspeed of 50-60m/s. The aerosol intake on the Twin Otter consisted of a forward facing nearly-isokinetic diffuser cone, followed by a 1m long 4cm ID stainless steel tube, the end of which was branched to accommodate three filter packs. One of the filters was made of Teflon (Gelman-47mm) and was used to determine the major organic and inorganic species; another acid-washed Teflon filter was used for trace metal analyses; and the third filter made of quartz (QAO-2500, Pallflex) for black carbon studies. The third filter holder was designed slightly differently from the other two so that only the 10mm center diameter area was exposed for aerosol collection.

Aerosol samples were obtained by exposing the filters in level flights at a single altitude between 0.1 and 2km in the cloud free atmosphere for a time period of 10 to 70min. A rotary vacuum pump was employed to provide air flow through the filter and the flow was monitored by a mass flow meter. The flow rates through the filters were set to match the flow through the inlet opening based on an airspeed of 60 m/s (Li et al, 1996). In general, three seperate filter packs were exposed simultaneously and one or two samples collected for each on most flights. Filters were packed and unpacked in a particle-free, laminar flow workstation. The intake tube was carefully cleaned with methanol before the flight.

There were 16 samples available for black carbon analysis collected over 15 flights during RACE. The total sampling air volume varied from 0.2 to $1.8m^3$ with a flow rate of approximately 24 liters per minute. Because the maritime region was covered by smoke from a Quebec forest fire on August 22, 1995, the samples from Flight 5, provided very valuable and unexpected information on the effect of the forest fire smoke plume. On that day the smoke was mixed from the surface to about 1.5km, with a maximum particle number concentration of $10,000/cm^3$ over a horizontal distance of 150 kilometers.

The blank filters on the Twin Otter were handled on the flight in the same way as aerosol sampling filters except that the vacuum pump was off and no air was filtered.

3.1.1 B) Air Sampling from Ferry

In addition to the aircraft, a platform for aerosol study was placed on board the Bluenose Ferry which runs between Yarmouth, Nova Scotia and Bar Harbour, Maine, USA. Just as on the Twin Otter, there were three intakes for aerosol sampling, one for major organic and inorganic species study, another for trace metal study, and a third for black carbon. The filters were mounted separately in the filter holders, which had designs similar to the ones on the Twin Otter. The mount hung facing downward at a height of approximately 25m above the sea level. A lampshade-plastic shield protected the filter packs from rain both from above and from the side. A single high-volume vacuum pump supplied ambient air to the filters at an average flow rate of 12 liters per minute. Thirteen samples were collected for black carbon analyses. Each filter was exposed on board the Bluenose during journeys between Yarmouth and Bar Harbour, with a total air sampling volume ranging from 2 to 5 m^3 and sampling duration of 2 to 4 hours.

3.1.1 C) Cloud Water Sampling

Cloud water samples were collected using the modified slotted-rod Teflon or delrin collectors (Leaitch et al., 1992). The collector was deployed out of the top of the fuselage ahead of the propellers. Cloud water samples once collected were stored in a cooler for the duration of the flight, weighed on an electronic balance after the

flight, and separated into individual samples for a variety of species analyses: major inorganic and organic ions, H_2O_2, trace metals, dissolved HCHO and black carbon. Finally, samples were stored in a refrigerator at -4°C before further analysis. Before each flight, the cloud water collector was rinsed with filtered, deionized, distilled water obtained from the Millipore Super-Q water system (referred to as Super-Q water hereafter). Two blank samples were obtained by spraying the water into each notch of the cloud collector rod and collecting all of the rinse water, which amounted to about 15 ml. Sixteen cloud water samples were obtained for black carbon studies. The liquid water content (LWC) of the cloud sampled ranged from 0.10 to 0.55 g/m^3. The length of time required to collect a single cloud water sample varied from 2 to 20min, which was equivalent to a distance of 7 to 70km.

3.1.2 Air Sampling in Downtown Halifax

During the summer of 1995 and the winter of 1995-1996, aerosol samples near ground level were collected on the Roy Building located in downtown Halifax, Nova Scotia, a site with a high level of man-made pollution. The instrumentation was set up in a room on the second floor. The aerosol sampling line (1cm ID) was inserted vertically into the main sampling tube which extended outside a window and faced downward at a height of about 15 meters. A vacuum pump was used to supply ambient air to the filter. Only the center 10mm diameter portion of the filter was exposed to air by

placing a mask inside the filter holder. Fifteen aerosol samples were collected from June to August, 1995 with an average total sampling volume of approximately $5m^3$, at a flow rate of about 0.5 liter/min. The sampling duration was about one week in the summer. Thirteen samples were collected from January to March, 1996 with an average total sampling volume of approximately $3m^3$ and flow rate of about 1 liter/min. The sampling duration varied from 7 hours to 4 days in the winter.

In some cases, the total aerosol mass was also studied. The filter was heated at $90^{\circ}C$ for one hour to remove water vapour, then weighed using a Fisher Scientific Mettler H54 electronic balance (accuracy $10\mu g$) and kept in a desiccator before sampling. The same procedure was repeated after the sample was loaded on the filter. The total aerosol mass was calculated from the difference of the filter weight before and after sampling. In some filters, fiber loss occurred when the filter was removed from the holder. This was more common in the summertime.

3.1.3 Rain Sample Collection

More than 40 rain samples were collected using a 20cm diameter polyethylene funnel, located at three sites in Halifax, and one rural site in Bridgewater, Nova Scotia during the summer of 1995 and the winter of 1995-1996. The sampling duration ranged from 20min to several hours, and the total weight varied from 20g to

200g. Consecutive sampling was made in some cases to study the systematic variation of black carbon content during rainfall. Most of the rain samples were processed shortly after collection; the others were kept refrigerated at -4°C before further processing. The funnel collector was rinsed with Super-Q water before and after sampling. Some of the rinse water was also collected and handled in the same manner as the rain samples and then analyzed as blank filters for the rain samples.

3.1.4 Snow Sample Collection

Snow sample collection was made in Halifax (urban area) and Bridgewater (rural area) during the 1995-1996 winter. Fresh snow was either collected on a 50 x 60 mm polyethylene container and transferred to a glass bottle or scooped directly into bottles. More than 20 samples were obtained, with some of them consecutively collected during a snowfall. The sampling duration varied from 30min to several hours and the total weight ranged from 50g to 250g. Samples were kept refrigerated. Just before further processing, the snow samples were melted in a microwave oven.

3.1.5 Liquid Phase Sample Processing - Filtration Procedure

All of the liquid phase samples went through a filtration procedure in order to separate the insoluble aerosols from the liquid phase. As

in air sampling, the Pallflex QAO-2500 47mm quartz filter was used. Filtration was performed through each filter three times in a polyethylene filtration device placed under gentle vacuum. All snow samples and part of the rain samples were pre-filtered by a 10μm-pore-size Millipore filter to remove the large particles, such as leaves, insects, and pollen. A mask of polyester sheet with a center hole of 10mm diameter was placed above and below the filter during the filtration. Therefore, all insoluble aerosols were concentrated in a 10mm diameter spot in the center of the quartz filter after the filtration procedure. The sample filters for the black carbon analysis were dried in an oven at 30°C for about 24 hours, and then kept in a petri-dish separately until ready for analysis.

3.2 Black Carbon Analysis

There is a wide range of methods used for measuring atmospheric black carbon (Malissa et al., 1976; Hansen et al., 1982; 1984; Clark, 1982; Gundel et al., 1984; Chylek et al., 1987). A variation of the thermo-optical method, originally developed by Malissa et al. (1976), has been employed for the analysis of black carbon aerosols collected on the quartz filters (Johnson et al., 1996; Wu, 1992). The method is based on light absorption by black carbon. The amount of black carbon is determined from the transmission of a laser beam, $\lambda=0.6328\mu m$ (He-Ne), through a quartz filter containing the black carbon at room temperature, and after heating the filter to 700°C where the black carbon oxidizes into carbon dioxide.

Figure 3.1 shows the experimental apparatus used to determine the amount of black carbon. The filter, located inside a stainless steel holder, is placed inside a furnace consisting of a 5cm ID quartz tube wrapped with two NiChrome V heating wires. The furnace is insulated with quartz fiber cloth and placed inside a stainless steel housing. The furnace heating power is 800 watts and can provide a temperature inside the furnace of approximately 700°C within 20 minutes of heating. In operation, light from a 5mW He-Ne laser ($\lambda=$ 0.6328μm) is passed through a chopper (frequency= 700Hz) and split by a partially silvered mirror. The reflected beam is detected by a silicon photodiode, and used as a reference. The transmitted beam passes through the front quartz window of the furnace and onto the quartz filter. Emerging from the back quartz window of the furnace, the transmitted beam is then passed through an optical telescope and focused onto another silicon photodiode. An amplifier is attached to each photodiode to amplify the reference and sample signals. Both signals are then sent to a lock-in amplifier locked at the chopper frequency. The sample and reference signals are subtracted out by the lock-in amplifier and the resulting output is then further amplified. The output of the lock-in amplifier is recorded by a chart recorder and monitored by an oscilloscope parallel to the recorder.

A thermoprobe (Cole Parmer Inconel exposed junction heavy-duty thermocouple probe) is employed to measure the temperature near
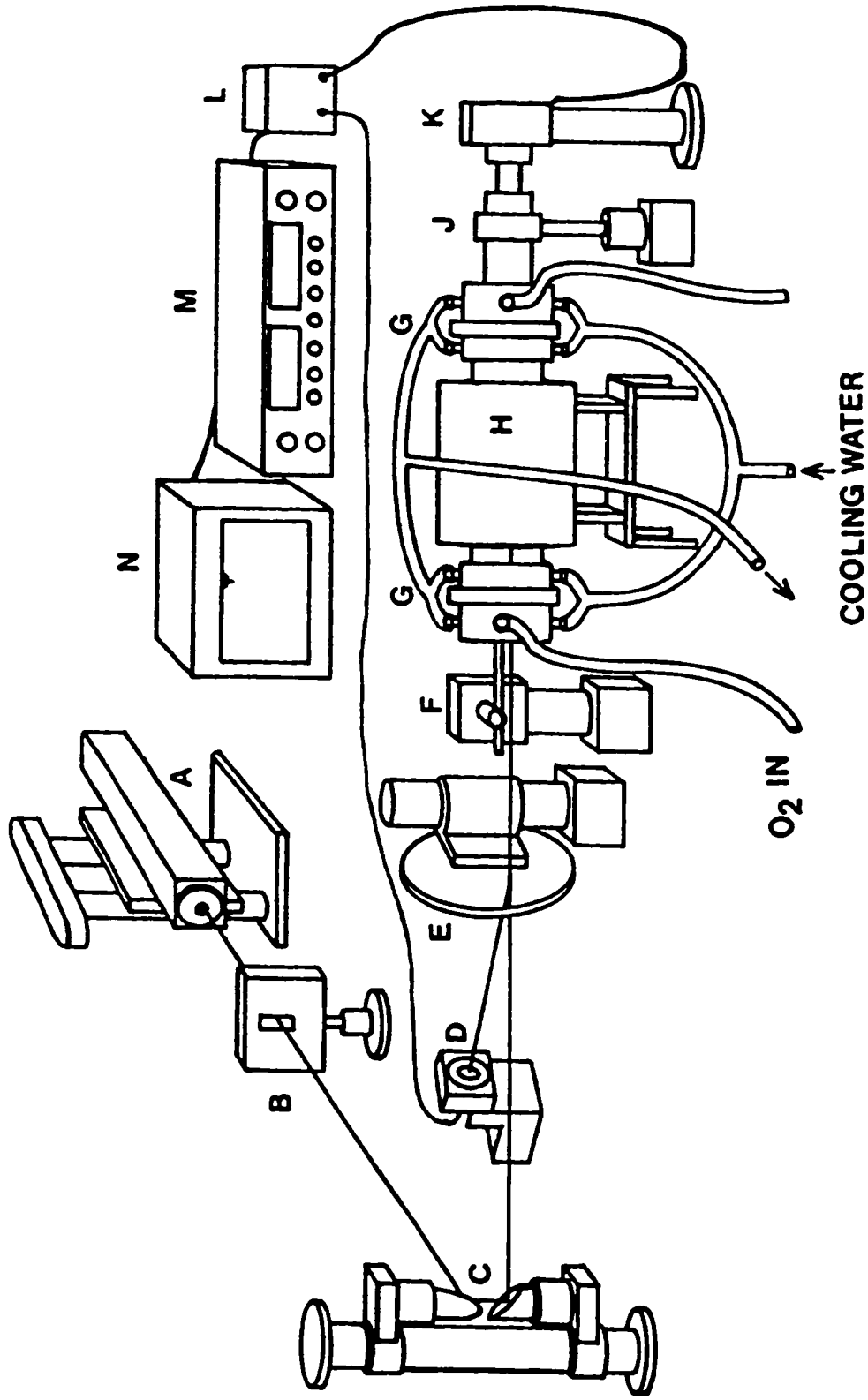
Figure 3.1 Experimental apparatus of the thermo-optical method.

A-laser; B-chopper; C-beam steerer; D-detector for the reference beam; E-beam splitter; F-gear motor; G-end caps and window; H-furnace; J-telescope; K-detector for the sample beam; L-amplifier; M-lock-in amplifier; N-chart recorder.

the filter holder inside the furnace. A stream of pure O_2 is introduced into the furnace to purge CO_2 and to facilitate oxidization of black carbon.

A mechanism is used to translate the quartz filter holder continuously up and down inside the furnace. This translation allows the laser to scan from the blank portion (edge) to the aerosol-loaded portion (central spot) of the filter at a frequency of 0.2Hz. The difference in the transmittance contrast (between the center and edge) of the filter before and after heating is proportional to the amount of black carbon content on the filter. Because the blank is on the same filter and burned with the sample, errors associated with filter-to-filter variation in homogeneity can be reduced. Furthermore, using the same path length and detector for both the sample and the blank minimizes errors associated with electronic instability and window transparency fluctuation.

Figure 3.2 shows a typical signal recorded on the chart recorder. It is in the form of peaks and troughs corresponding respectively to light passing through the blank region of the filter where the transmittance is maximum, the center spot of the filter where the transmittance is minimum. The transmittance contrast of each filter is measured before heating the furnace and after carbon combustion when the temperature inside the furnace has returned to room temperature. The heating process takes about 30min and cooling takes about 2 hours.
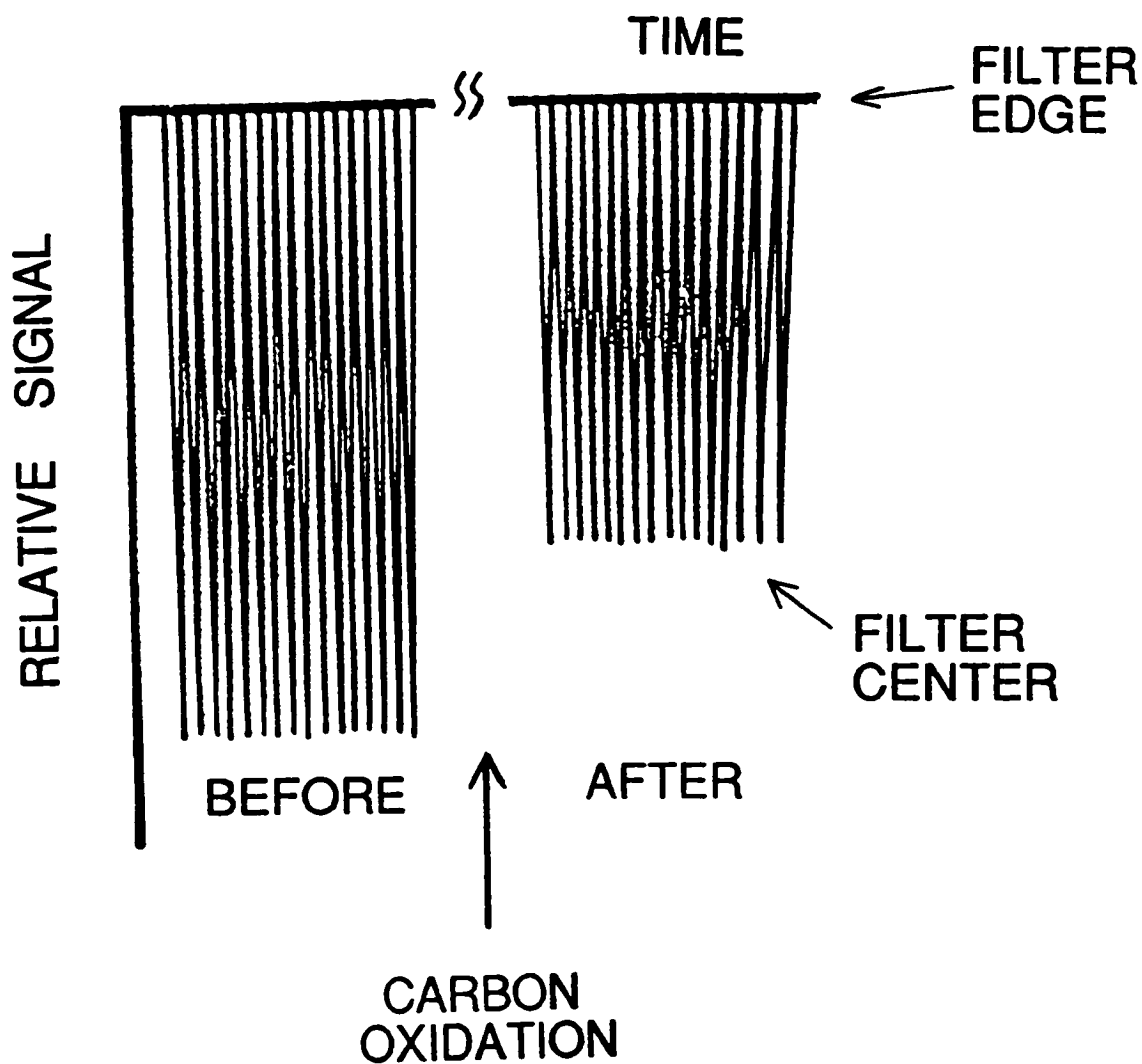
Figure 3.2 A typical signal of black carbon analysis in the thermo-optical method. The time interval between each peak is $\Delta t = 5$ sec.

Generally 50 peaks are averaged for each measurement. In order to insure alignment of the system and to compensate for any drift in gain, a standard reference, which is not burned, is scanned between samples (Section 3.3).

The burning process is necessary to determine the contribution of black carbon to light absorption. It has been observed that some sample filters still absorb a noticeable amount of the light after burning, which is likely caused by the noncombustible residual aerosols that remain on the sample portion of the filter.

3.3 Calibration of Black Carbon Standard Reference

Two different polydispersions of black carbon particles are used for standard reference calibration. One has mean radius of $0.048\mu m$, hereafter referred to as VM, another one has mean radius of $0.09\mu m$ hereafter referred to as ST.

3.3.1 Standard Reference Making

Making a uniformly dispersed black carbon suspension is a key part of the calibration procedure. An amount of 1mg to 100mg of black

carbon is weighed on a Fisher Scientific Mettler H54 electronic balance (accuracy $10\mu g$) and mixed with about 800 ml of Super-Q water in a glass container. The suspension of black carbon is then agitated in an ultrasonic bath for about 3 hours in order to increase homogeneity and to break up aggregates of black carbon particles. In some cases, it is necessary to add about $20\mu l$ of surfactant (photo-flo) into the suspension in order to break up the black carbon film formed on the surface of the suspension. Adequate dispersal of black carbon in the ultrasonic bath treatment has been confirmed by examining the particles collected on the filter using a microscope. Few aggregates of black carbon remained.

Suspensions of black carbon with concentrations of 100mg/l, 10mg/l and 1mg/l are prepared initially. With successive dilutions using Super-Q water lower concentrations of black carbon suspension are obtained.

In order to minimize the error associated with filter inhomogeneities, filters are selected by examining the transmittance of the filter at different orientations using the He-Ne laser beam. Standard references are prepared with these filters using the uniformly dispersed black carbon suspensions. Each standard reference is filtered twice to ensure maximum filtration efficiency (details in Section 3.3.3). About 10ml of Super-Q water is used to rinse each container of the suspension and the rinsed water is also passed through the reference filter. Residual levels of black carbon remaining after the second filtration are examined by analyzing the

third filtration filter (see Table 3.3 in Section 3.3.3). After the filters are dried in the electric oven at 30°C for about 24 hours, the standard reference filters are ready for analysis.

3.3.2 Calibration Results

The standard references are examined in the optics lab. In order to reduce the errors associated with the variation in homogeneity from filter to filter, the calibration results are obtained by burning the standard reference filters. The transmittance of each standard filter is measured and recorded in the form of a series of peaks before and after burning. Nine VM and six ST standard references have been examined and the results are listed in Table 3.2. The black carbon amount on the standard filters ranged from 0.3 to 2.0μg. The change of the peak height before and after burning as a function of the amount of black carbon content for both VM(*) and ST(o) references are plotted on Figure 3.3. Intercomparison between the independent original suspensions are made with RC-21, RC-23, RC-27, and RC-28 and the results show very good agreement (see Figure 3.3). One noteworthy feature in Figure 3.3 is that there is a linear relationship between black carbon content and the change in peak height from burning.

3.3.3 Errors in Calibration

Errors in calibration arise from the suspension making, filtration and burning processes. An absolute error in scanning the peak height, $\delta(\Delta PH) = \pm 1mm$ leads to a relative error of 0.6% to 4%. The principal error source is the uncertainty in black carbon amount on the standard filter which arises from the filtration process. The estimated error in the suspension-making process, including weighing black carbon (<2%) and diluting with water (<1%), is approximately 2%.

The filtration efficiency of the quartz filter, defined as the percentage of mass collected by the filter, was confirmed by passing the suspension successively through three separate filters. The results are listed in Table 3.3 and indicate that two filtrations should be sufficient to capture 95% of black carbon particles. The same type of quartz filter (Pallflex 2500 QAO) was used by Chylek et al. (1987), when they studied the filtration efficiencies of the quartz filter using aluminum oxide particles with mean sizes of 0.05, 0.3 and $1.0 \mu m$. They obtained collection efficiencies of single-pass filtration ranging from 66 to 85%. They suggest the efficiency of two to four filtrations should be greater than 90%. Based on the filtration efficiency studies and other uncertainties such as black carbon particles adhering to the wall of the container, we estimate the uncertainty to be 5 -10% in the filtration process. The blank filters in calibration are obtained by filtering one liter of Super-Q

Table 3.2 The results of black carbon reference calibration

Type	Filter	M_{bc} (µg) ± 5~10%	Δ(PH) (mm) ± 1mm	Source of suspension	Amount of surfactant
VM	RC-84	0.39	25	BC-S-4A	N/A
VM	RC-82	0.65	54	BC-S-4B	N/A
VM	RC-83	0.65	64	BC-S-4B	N/A
VM	RC-28	1.30	76	BC-S-4C	N/A
VM	RC-27	1.30	84	BC-S-4C	N/A
VM	RC-23	1.33	73	BC-S-3A	20µl
VM	RC-21	1.33	76	BC-S-3A	20µl
VM	RC-89	1.56	134	BC-S-4A	N/A
VM	RC-87	1.95	139	BC-S-4A	N/A
ST	RC-45	0.64	41	BC-S-7A	20µl
ST	RC-46	0.64	49	BC-S-7A	20µl
ST	RC-43	1.27	116	BC-S-7B	20µl
ST	RC-49	1.27	77	BC-S-7B	20µl
ST	RC-50	1.91	120	BC-S-7C	20µl
ST	RC-42	1.91	163	BC-S-7C	20µl

Note:

BC-S-4* : The dilutions of the black carbon suspension BC-S-4, which has a concentration of 1.30 ± 0.01 mg/l.

BC-S-3* : The dilutions of the black carbon suspension BC-S-3, which has a concentration of 13.30 ± 0.01 mg/l.

BC-S-7* : The dilutions of the black carbon suspension BC-S-7, which has a concentration of 6.36 ± 0.01 mg/l.
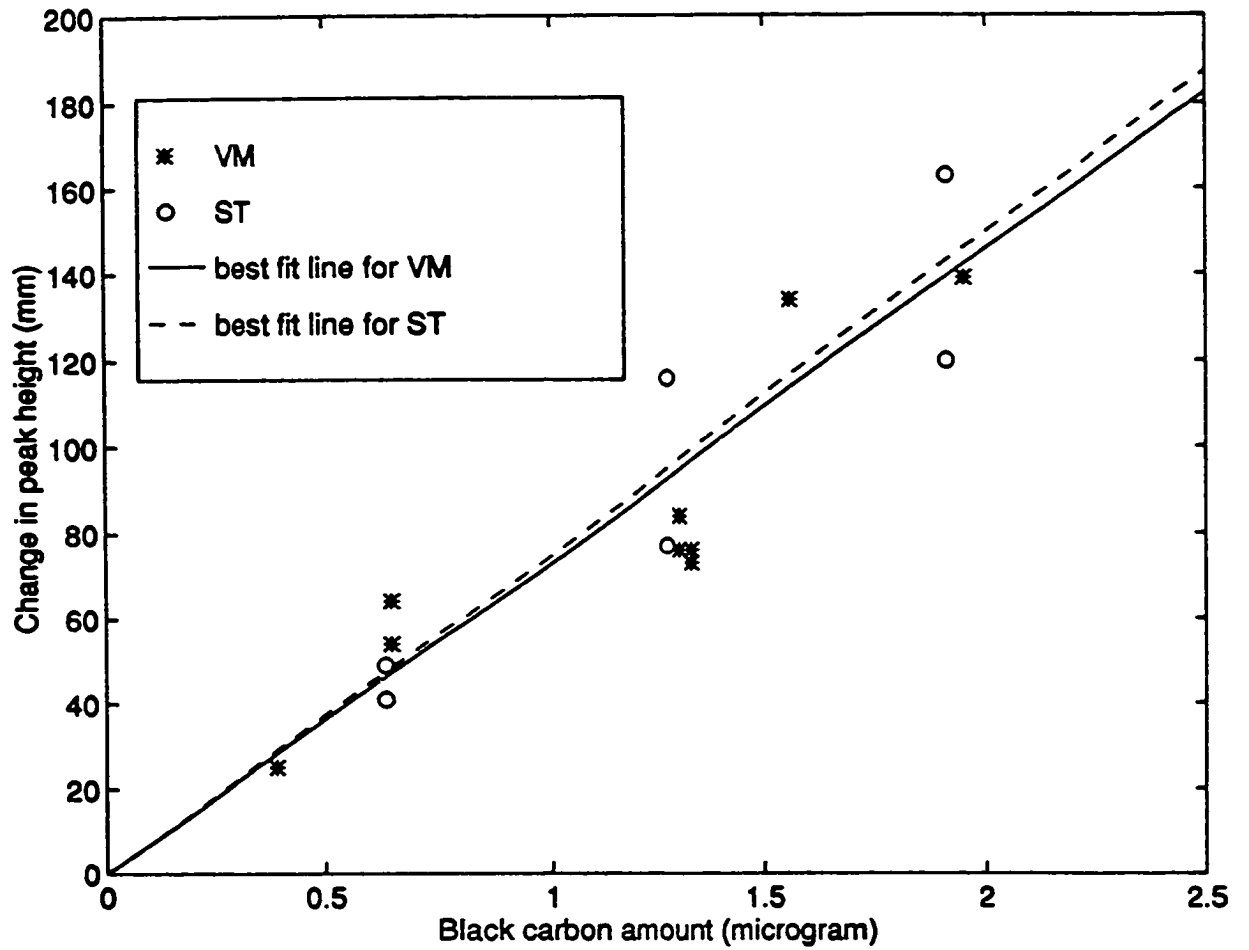
Figure 3.3   The black carbon reference calibration curve. The dashed line is   the best fit line for ST (r=0.09μm)   standard (o),   and the solid line is the best fit line for the   VM (r=0.048μm) standard (*).

Table 3.3 Efficiency of quartz filter for collection of

black carbon particles

Filter	source of BC	filtration	BC collected on the filter (μg)	filtration efficiency
RC-4	VM	1st	0.25	71%
RC-5	VM	2nd	0.103	
RC-6	VM	3rd	0.0	
RC-7	VM	1st	0.41	95%
RC-8	VM	2nd	0.013	
RC-9	VM	3rd	0.01	
RC-28	VM	1st+2nd	1.1	99%
RC-28C	VM	3rd	0.01	
RD-8A	Rain sample	1st	0.50	94%
RD-8B	Rain sample	2nd	0.0	
RD-8C	Rain sample	3rd	0.01	
C47-1-A	Ice core sample	1st	1.79	88%
C47-1-B	Ice core sample	2nd	0.24	
C47-1-C	Ice core sample	3rd	0.0	
D5-2-A	Ice core sample	1st	0.49	86%
D5-2-B	Ice core sample	2nd	0.08	
D5-2-C	Ice core sample	3rd	0.0	

water through the individual quartz filters. Laboratory black carbon analysis of four blanks yields black carbon amounts on the filter ranging from zero to $0.032\mu g$, with an average amount of black carbon of $0.017\mu g$ and standard deviation of $0.016\mu g$.

Table 3.4 Blank Filters (Super-Q water testing)

Filter	SQ-1	SQ-2	SQ-3	SQ-4	Average
$M_{bc}(\mu g)$	0.032	0.00	0.00	0.02	0.017 ± 0.016

If a 10% error in each standard reference is assumed, the average result of the VM standard references is represented by linear regression in Figure 3.3, which can be expressed by

$$\Delta (PH) = (73 \pm 3) \ (mm/\mu g) \ M_{bc} \ - (0.1 \pm 0.7) \ (mm), \tag{3-1}$$

where $\Delta(PH)$ is the peak height in mm measured before and after burning; and M_{bc} is the black carbon content in μg.

The best fit line for the ST standard references is

$$\Delta (PH) = (75 \pm 3) \ (mm/\mu g) \ M_{bc} \ - (0.2 \pm 0.8) \ (mm) \tag{3-2}$$

Equations 3-1 and 3-2 indicate that there is essentially no difference between the VM and ST references within the experimental uncertainty range.

Finally, it is concluded that the accuracy of the calibration is approximately ± 5% and the detection level is ≥ $0.02\mu g$. The VM calibration curve expressed as Equation 3-1 is used as the final black carbon standard reference calibration.

3.3.4 Discussion of the Calibration Curve

The similar shape of the VM and ST calibration curves can be explained theoretically. In our model, a beam of light passes through the sample filter before burning (Figure 3.4a) and after burning (Figure 3.4b).

(a)

$$I_0 \qquad I_{bb}$$

Quartz filter

black carbon particles

(b)

$$I_0 \qquad I_{ab}$$
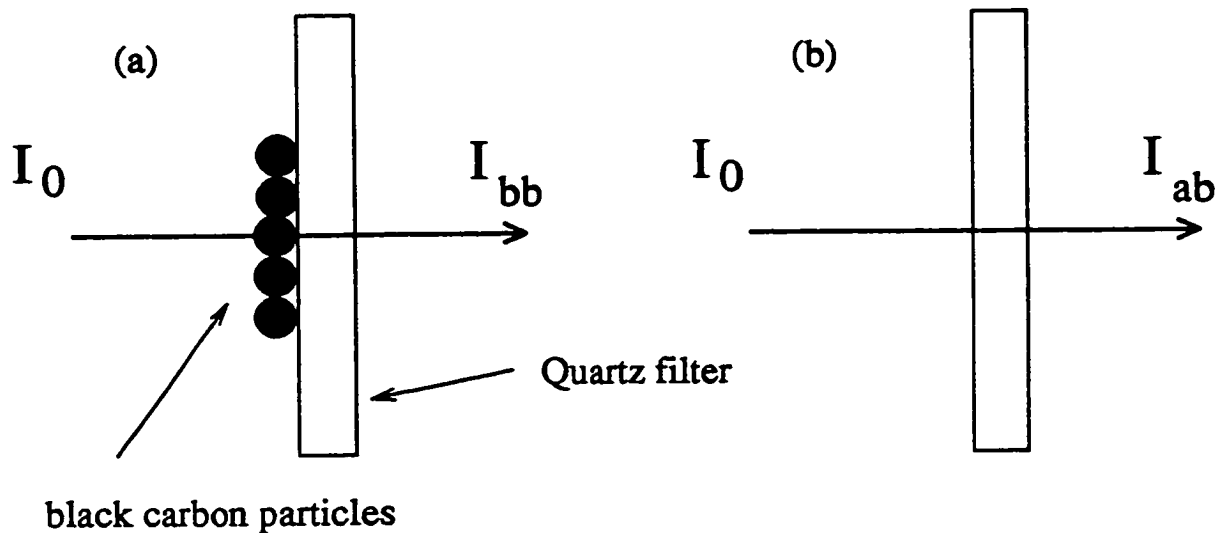
Figure 3.4: Schematic diagram of a light beam passing through the sample filter before burning (a) and after burning (b).

The intensity of the transmitted light beam is attenuated from I_0 to I_{bb} (before burning) or I_{ab} (after burning). The attenuation is due to the absorption and scattering of black carbon particles as well as

the filter. The intensity removed, ΔI, from the incident beam can be expressed as

$$\Delta I_{bb} = I_0 - I_{bb} = \Delta I_{abs}^{bc} + \Delta I_{sca}^{bc} + \Delta I_{abs}^{fil} + \Delta I_{sca}^{fil} \qquad (3\text{-}3)$$

$$\Delta I_{ab} = I_0 - I_{ab} = \Delta I_{abs}^{'fil} + \Delta I_{sca}^{'fil} \qquad (3\text{-}4)$$

Where ΔI_{sca} denotes the intensity removed by scattering; and ΔI_{abs} denotes the intensity removed by absorption. The subscript indicates whether the measurement is made before burning (bb) or after burning (ab). The superscript denotes whether the intensity is scattered or absorbed from the black carbon (bc) or the filter (fil). We assume no multiple scattering effect occurs.

In general, the absorption caused by the filter is very small in the visible spectral region compared with the black carbon absorption. If the absorption term associated with the filter is neglected, the change of the light intensity removed from the incident beam before and after burning, δI_{ext}, can be written as

$$\delta I_{ext} = \Delta I_{bb} - \Delta I_{ab} = \Delta I_{abs}^{bc} + \Delta I_{sca}^{bc} + \Delta I_{sca}^{fil} - \Delta I_{sca}^{'fil} \qquad (3\text{-}5)$$

The intensity removed by the scattering of the filter before burning, ΔI_{sca}^{fil}, is lower than the value after burning, $\Delta I_{sca}^{'fil}$, because the unburned black carbon particles shade the surface of the filter. Since there is no evidence of preference between the scattering due to the filter and that due to the black carbon particles plus the filter, a plausible hypothesis is made that

$$\Delta I_{sca}^{bc} + \Delta I_{sca}^{fil} \approx \Delta I_{sca}^{'fil} \tag{3-6}$$

Therefore, the change in the extinction before and after burning is dominated by the absorption of the black carbon:

$$\delta I_{ext} = \Delta I_{bb} - \Delta I_{ab} \approx \Delta I_{abs}^{bc} \tag{3-7}$$

and the contribution of scattering from black carbon particles and the filter can be neglected.

The size-dependent mass specific absorption cross section, σ_{abs}/m, can be calculated by using an adapted Mie scattering program (Bohren and Huffman, 1983) under the following assumptions:

1. the refractive index of black carbon is 1.75 - 0.44i;

2. the black carbon particles on the filter are spherical in shape and are distributed in the same plane;

3. multiple scattering can be neglected; and

4. the mass density of black carbon is $\rho=1.8g/cm^3$.

The calculated mass specific absorption cross section as a function of particle size is plotted in Figure 3.5. The values for the VM and ST particles are listed in Table 3.5. Figure 3.5 shows that the ST $(r=0.09\mu m)$ particle is closer to the peak of the specific absorption than the VM $(r=0.048\mu m)$ particle. The ratio of σ_{abs}/m for ST to VM particle is 1.20, consequently a single sized ST particle is
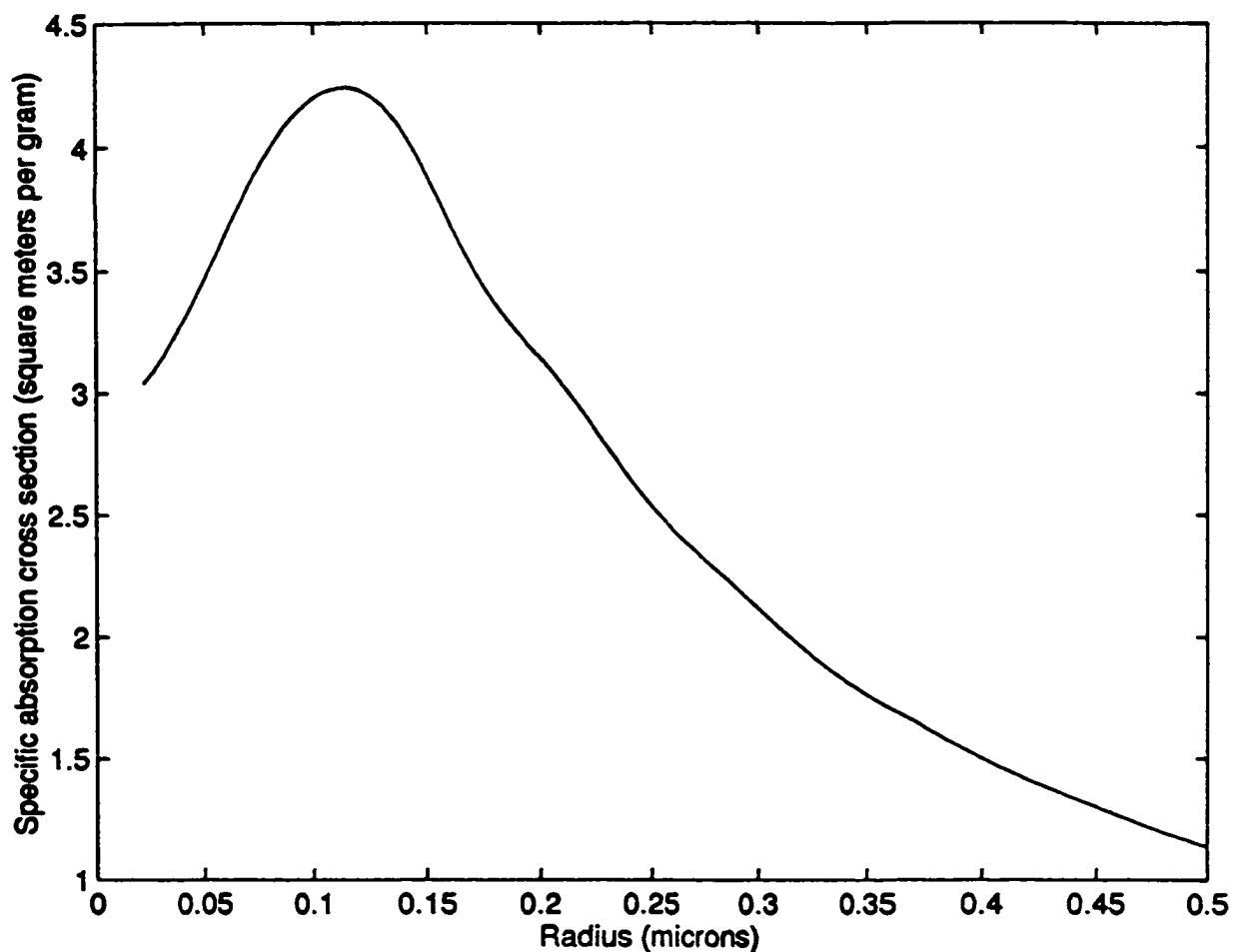
Figure 3.5   The size dependence of the specific absorption (m^2/g) of black   carbon particle at wavelength of $0.6328\mu m$, $\rho = 1.8 g/cm^3$, and refractive index $m = 1.75 - 0.44i$.

expected to display a slightly stronger absorption than the equivalent VM particle.

Since both ST and VM particles are polydispersed, the size distribution function is necessary to estimate the absorption behavior of ST and VM particles. Therefore we further assume that both VM and ST have log-normal size distributions, i.e.,

$$n(r) = \frac{N_o}{r\ln\sigma\sqrt{2\pi}} \exp[-\frac{(\ln r - \ln r_g)^2}{2\ln^2\sigma}]$$

(3-8)

where, r is the radius of the particle (μm), N_o is the total number density (cm^{-3}); r_g is the geometric mean radius (μm); σ is the standard deviation; $n(r)$ is the size distribution in units of particle number per cm^3 per μm.

The absorption coefficient, K_{abs}, can be obtained by integrating σ_{abs} over the size distribution. i.e.,

$$K_{abs} = \int \sigma_{abs} n(r) dr$$

(3-9)

K_{abs} has dimensions of inverse length (m^{-1}) and indicates the amount of radiation removed from the incident beam by absorption. The specific absorption coefficient, ψ_{abs}, can be calculated by dividing K_{abs} by the mass density M, which is defined as

$$M= \frac{4\pi\rho}{3} \int r^3 n(r)dr \tag{3-10}$$

Here, ρ is the mass density of the absorbing material and the units for M are μg per cm^3. Hence,

$$\Psi_{abs}= \frac{K_{abs}}{M} = \frac{\int \sigma_{abs} n(r)dr}{\frac{4\pi\rho}{3} \int r^3 n(r)dr} \tag{3-11}$$

The calculated results are listed in Table 3.5, where standard deviations of $\ln\sigma = 0.1$ ($\sigma=1.1$) and $\ln\sigma = 0.4$ ($\sigma = 1.5$) are used due to the uncertainty of this parameter for VM and ST particles, and because these values are commonly used in the literature.

Table 3.5 The specific absorption cross sections and coefficients for VM and ST particles

	r_g (μm)	σ_{abs}/m (m^2/g)	Ψ_{abs} (m^2/g) $\ln\sigma = 0.1$	Ψ_{abs} (m^2/g) $\ln\sigma =0.4$
VM	0.05	3.43	3.46×10^3	3.81×10^3
ST	0.09	4.12	4.13×10^3	3.60×10^3
$\frac{ST}{VM}$		1.20	1.19	0.95

From the calculated results listed in table 3.5,   the ratio of the two specific absorption coefficients   varies from 1.19 for   the narrow size distribution ($\ln\sigma = 0.1$)   to 0.95 for the wider dispersion ($\ln\sigma = 0.4$). The conclusion is that VM and ST black carbon particles   have very similar   absorption characteristics at $\lambda=0.6328\mu m$ for   particle size distributions   within $\ln\sigma = 0.1$ to 0.4.

As discussed above,   the peak height   change, ΔPH, on   the calibration curves (Figure 3.3) is directly related to   the black carbon absorption. Consequently,   the slope of the calibration curve   is proportional to the specific absorption. Then the ratio of the two   specific absorption coefficients   can be   obtained experimentally from   the calibration curves:

$$\frac{(\Psi_{abs})_{ST}}{(\Psi_{abs})_{VM}} \approx 1.03$$

This result   falls in   the theoretical prediction   range (1.19 ~ 0.95).

3.4 Measurement Results and Discussion

The total black carbon content   on the sample filters has been measured   using   the thermal-optical method. The total   air volume passed through the filter can be obtained from the   sampling duration and flow rate. Consequently the black carbon concentration of the air sample can be   calculated. Since the total weight of each liquid sample has been measured, the concentration of black carbon

in the liquid sample can be obtained as well. In the following section, all the information about RACE samples, such as altitude of sampling, sampling duration, flow rate, temperature, pressure, etc., have been provided by AES. All the values of the concentration, flow rate and volume, have been calibrated at a standard temperature (0°C) and pressure (1 atm = 1013.25 mb).

3.4.1 Black Carbon in Air

3.4.1 A) Results from Twin Otter Flights

Table 3.6 shows the black carbon concentrations measured from the Twin Otter. The concentration of black carbon generally ranges from zero to $0.49\pm0.03\mu g$ /m^3 with two exceptionally high values (1.08 ± 0.06 and $1.00\pm0.05\mu g/m^3$), which were obtained on the smoky day when the study region was covered by smoke from a forest fire in Quebec. The average black carbon concentration over all the samples collected is about $0.13\pm0.01\mu g/m^3$, which is comparable to measurement results (0.12 ± 0.01 $\mu g/m^3$) found in the North Atlantic Region Experiment (NARE) in 1993 (Chylek et al. 1996).

The size distribution of aerosols is determined using a Particle Measuring System's (PMS) Passive Cavity Aerosol Spectrometer Probe (PCASP) which sizes particles into one of fifteen size bins from 0.135 to 3.0μm diameter and was mounted under the wing of the Twin Otter. Table 3.6 (Column 8) shows the total aerosol particle

Table 3.6 Black carbon in air samples collected from Twin-Otter

Sample	Date	Altitude average (m)	Sampling Duration (min)	Flow rate (l / min)	Total Volume (m³)	PCASP conc (cm⁻³)	CNconc (cm⁻³)	Pressue (mb)	Temprature (C°)	Total B.C. (µg)	B.C. conc. (µg/m³)
T04-C2	Aug-21	1709	29.45	24.62	0.725	66	848	817.99	17.23	0.01±0.01	0.01±0.01
T05-C1	Aug-22*	1230	10.30	18.13	0.187	6827	N/A	866.62	8.77	0.20*±0.01	1.08*±0.06
T05-C2	Aug-22*	873	11.33	26.70	0.303	7278	8885	907.85	13.20	0.30*±0.02	1.00*±0.05
T06-C1	Aug-24	130	23.38	25.89	0.605	2143	N/A	989.63	17.89	0.15±0.01	0.25±0.02
T09-C1	Aug-29	466	62.97	25.32	1.594	268	2059	960.13	17.96	0.04±0.01	0.03±0.00
T11-C1	Aug-30	520	34.45	23.52	0.810	260	1216	950.79	11.91	0.00±0.01	0.00±0.01
T12-C1	Aug-30	1132	35.38	21.24	0.751	488	1715	882.92	9.28	0.04±0.01	0.05±0.01
T13-C1	Sept-01	369	25.92	24.62	0.638	938	2362	958.95	17.03	0.11±0.01	0.18±0.02
T16-C1	Sept-05	359	41.75	25.10	1.048	426	2585	980.07	20.41	0.03±0.01	0.03±0.01
T16-C2	Sept-05	106	11.92	28.09	0.335	902	3026	1009.9	17.84	0.16±0.01	0.49±0.03
T16-C3	Sept-05	697	78.15	23.17	1.812	617	3006	943.04	15.89	0.01±0.01	0.01±0.00
T17-C1	Sept-07	1329	70.00	22.81	1.597	1619	5372	866.06	14.35	0.24±0.01	0.15±0.01
T18-C1	Sept-08	1522	15.08	24.30	0.366	58	692	845.81	10.83	0.04±0.01	0.11±0.01
T20-C1	Sept-09	472	21.33	24.72	0.527	975	1370	960.26	18.19	0.09±0.01	0.16±0.01
Average											0.13±0.01

Note: * -- Smoky Day   N/A -- Data is not available.
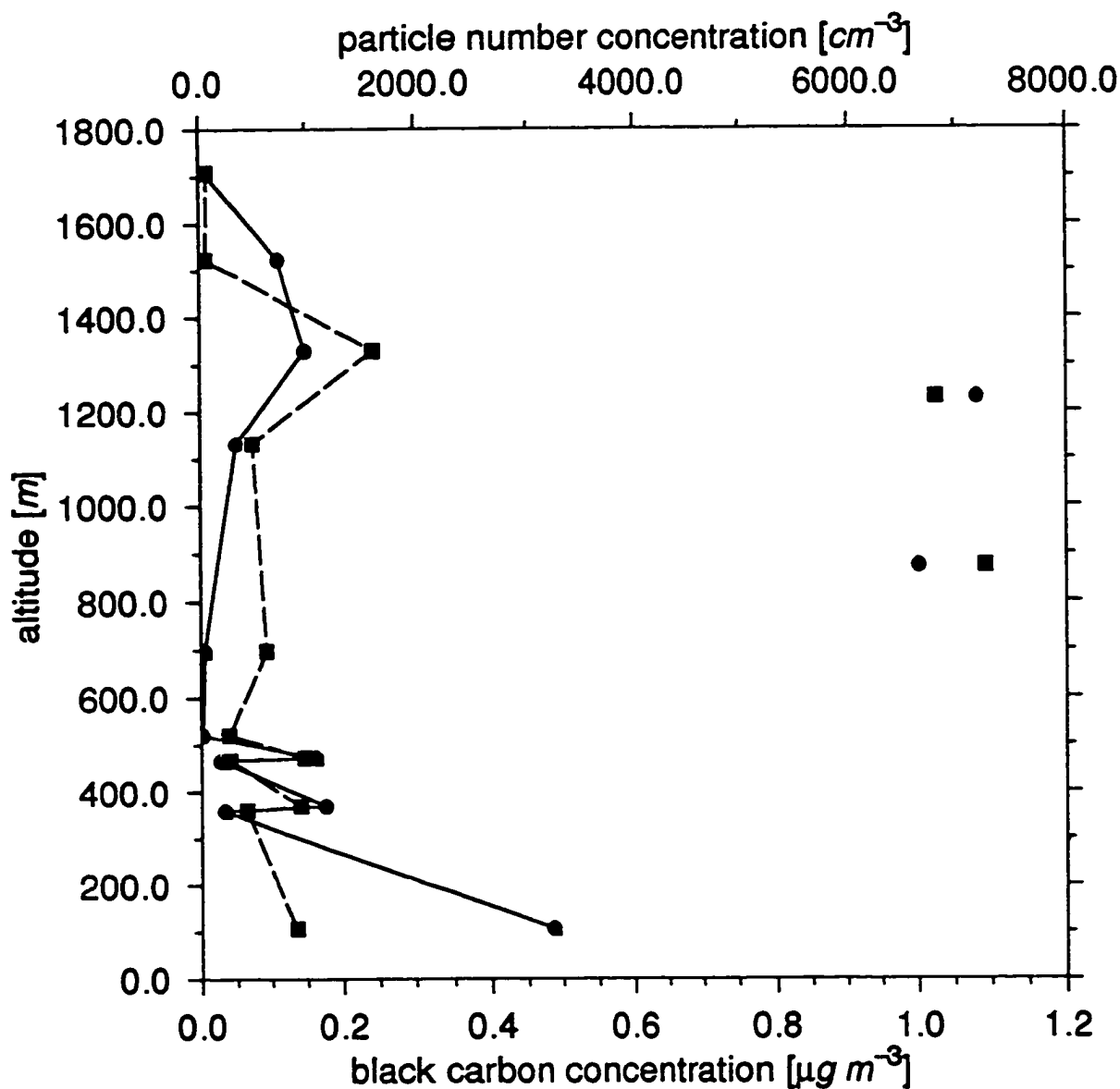
Figure 3.6 The measurement results of the black carbon concentration (dots connected with solid line), and particle number concentration (PCASP; squares connected with dashed line) for Twin Otter air samples during RACE. The extreme data points were collected on the day of the forest fire.

number concentration of the sampling air from the PCASP. Column 9 shows the condensation nuclei number concentration (CN Con.), which is measured with a TSI condensation particle counter. Details about the CN counter and PCASP are described in Leaitch et al., 1996, and Liu et al., 1996. The measurement results of the black carbon concentration and particle number concentration are shown on Figure 3.6. Generally a positive correlation is expected between the two concentrations since more aerosol loading is expected to lead to more black carbon on the filter.

The aerosol composition has been obtained by AES through chemical analysis of the Teflon filters which were exposed at the same time as the quartz filters on the Twin Otter. The major inorganic chemical species concentration of the aerosol, such as SO_4^{-2}, NH_4^+, and K^+, are listed in Table 3.7. The value listed in column 4 of Table 3.7 is the total concentration of SO_4^{-2}. The non-sea-salt SO_4^{-2} ($nss-SO_4^{-2}$) can be obtained by subtracting the fraction of SO_4^{-2} from the contribution of sea salt (Li et al., 1996; Broecker and Peng, 1982), which generally is a very small part of the total SO_4^{-2}. The average concentration of SO_4^{-2} is $1.27\mu g/m^3$. Figure 3.7 shows the comparison of SO_4^{-2}, NH_4^+, and black carbon concentrations. Both SO_4^{-2} and NH_4^+ show a positive correlation with black carbon concentrations in general, especially on the forest fire day. Because potassium is highly enriched in atmospheric particles produced by biomass burning (Warneck,1988; Levine,1990), the concentration of K^+ has been used as an indicator for biomass burning in ice core

Table 3.7 Major inorganic chemical species concentrations of the aerosol samples from Twin Otter

Sample	Altitude (m)	B.C. $\mu g/m^3$	SO_4^{-2} $\mu g/m^3$	NH_4^+ $\mu g/m^3$	K^+ $\mu g/m^3$	BC/ $SO4^{-2}$	TPM $\mu g/m^3$	BC/ TPM
T04-C2	1709	0.01	0.06	0.35	0.0	17%	0.26	3.8%
T05-C1	1230	1.08	1.27	1.70	0.22	85%	N/A	N/A
T05-C2	873	1.00	3.31	2.71	0.31	30%	N/A	N/A
T06-C1	130	0.25	N/A	N/A	N/A	N/A	N/A	N/A
T09-C1	466	0.03	0.41	0.18	0.0	7%	2.06	1.4%
T11-C1	520	0.00	0.50	0.30	0.0	0%	2.02	0.0%
T12-C1	1132	0.05	0.62	0.32	0.0	8%	6.31	0.8%
T13-C1	369	0.18	2.39	0.75	0.0	7%	8.21	2.2%
T16-C1	359	0.03	0.46	0.27	0.01	6%	2.85	1.1%
T16-C2	106	0.49	1.02	0.79	0.0	48%	5.97	8.2%
T16-C3	697	0.01	0.86	0.33	0.10	1%	4.00	0.2%
T17-C1	1329	0.15	4.13	2.09	0.04	4%	13.34	1.1%
T18-C1	1522	0.11	0.17	0.43	0.0	65%	0.36	30.6%
T20-C1	472	0.16	8.60	1.55	0.03	2%	14.84	1.1%

Note: BC-black carbon

TPM-total particle mass

N/A-Data are not availabel
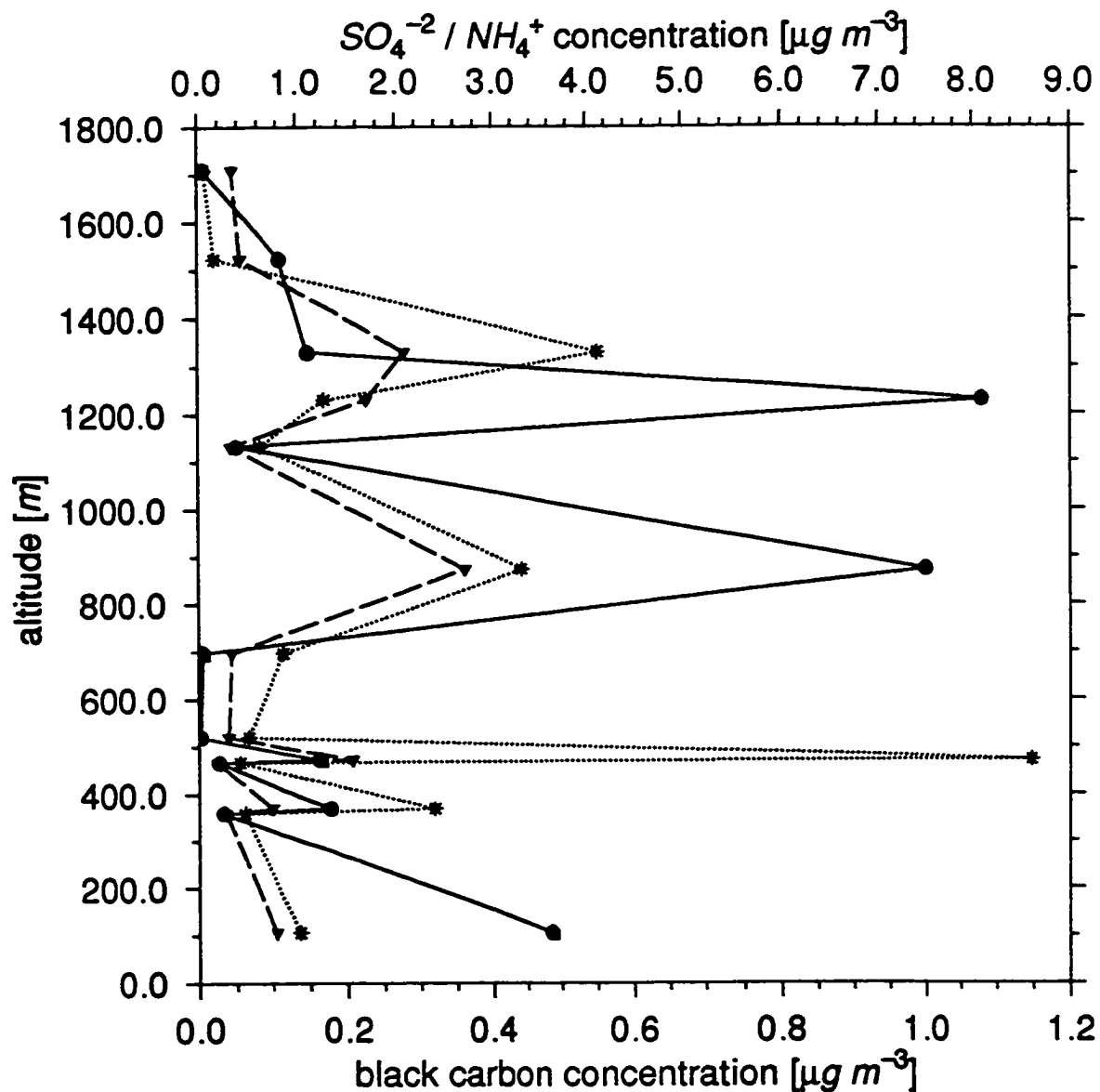
Figure 3.7 Comparison of black carbon concentration (dots connected with solid line), SO_4^{-2} concentration (stars connected with dotted line), and NH_4^+ concentration (triangles connected with dashed line) for Twin Otter air samples during RACE.
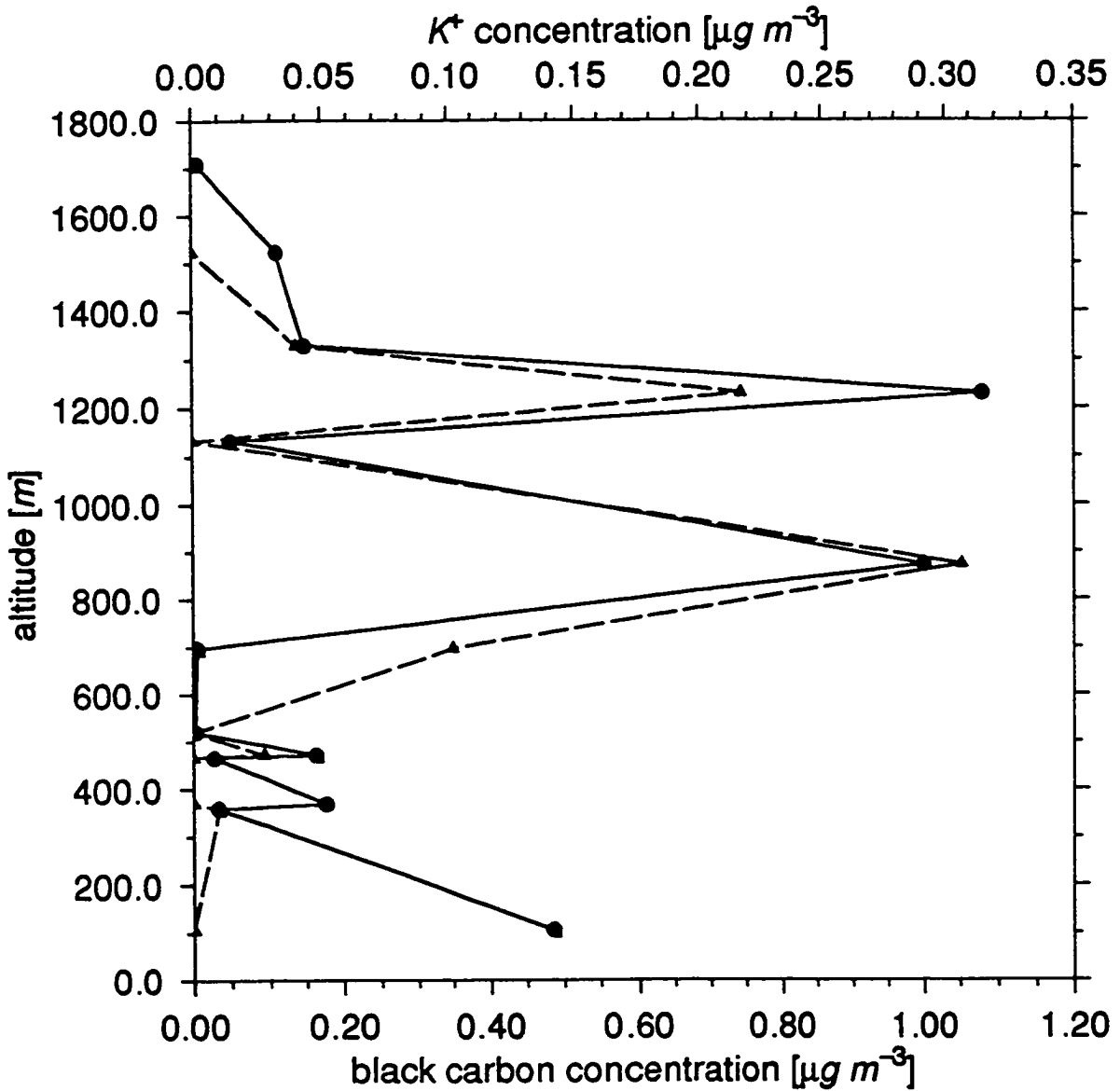
Figure 3.8 Comparison of black carbon concentration (dots connected with solid line), and K+ concentration (triangles connected with dashed line) for Twin Otter air samples during RACE.

studies (Wu, 1992). A clear positive association of K^+ with the peak of black carbon concentration on the forest fire day can be seen from Figure 3.8. Table 3.7 also shows the mass mixing ratio of black carbon to SO_4^{-2}, which varies from 1% to 85%. The average is 14% over all samples and 6% for samples excluding the samples obtained on the forest fire day (T05-C1 and T05-C2). The results are within the range of previous measurement.

The total particle volume (TPV) for each filter sample is calculated by integrating the particle volume in each size range. The total particle mass (TPM) for each filter sample is then calculated from the TPV. An average composite density value of 1.8 g/cm^3 (Liu et al., 1996; Li et al., 1996) is used when the TPM is calculated in Table 3.7. The ratio of black carbon to total aerosol generally varies between 0.1% to 3% for all Twin Otter aerosol samples except for T16-C2 where it was 8% and T18-C1 where it was 30%.

3.4.1 B) Near- Sea Surface Measurement on Ferry

The black carbon concentrations in the near-sea surface air are shown in Table 3.8. These vary between 0.06±0.01 to 0.96±0.05μg/m^3. The exceptionally high value 0.96μg/m^3, corresponding to a CN concentration of 1.2x10^4/cm^3, obtained on Aug. 25 at the Ferry from Bar Harbour to Yarmouth is most likely due to the pollution from the Ferry's exhaust. The average value of black carbon concentration in air above the sea surface is

Table 3.8 Black carbon in air samples collected from Ferry

Sample	Date	Ferry	Duration (min)	Flow rate (l / min)	Volume (m³)	CN conc (cm⁻³)	Total B.C. (µg)	B.C.conc (µg /m³)
F01-C1	Aug-23	F1 (B-Y)	255	19.64	5.008	3780	1.01±0.05	0.20±0.01
F03-C1	Aug-25	F3 (B-Y)	171	14.41	2.464	11724*	2.4*±0.1	0.96*±0.05
F06-C1	Aug-29	F6 (B-Y)	156	11.43	1.783	2333	0.26±0.02	0.15±0.01
F07-C1	Aug-30	F7 (B-Y)	230	13.22	3.041	5061	0.38±0.02	0.13±0.01
F08-C1	Sept-01	F8 (B-Y)	246	13.30	3.272	4196	2.3±0.1	0.69±0.03
F09-C1	Sept-01	F9 (Y-B)	156	13.49	2.104	3792	1.24±0.06	0.59±0.03
F10-C1	Sept-05	F10 (B-Y)	228	10.78	2.458	3240	0.34±0.02	0.14±0.01
F11-C1	Sept-05	F11 (Y-B)	223	11.82	2.636	3749	0.66±0.03	0.25±0.01
F12-C1	Sept-07	F12 (B-Y)	241	10.63	2.562	2020	0.15±0.01	0.06±0.01
F13-C1	Sept-07	F13 (Y-B)	180	11.37	2.047	6930	0.34±0.02	0.17±0.01
F14-C1	Sept-08	F14 (B-Y)	228	11.94	2.722	5209	0.17±0.01	0.06±0.01
F15-C1	Sept-09	F15 (B-Y)	240	12.19	2.926	3177	0.61±0.03	0.21±0.01
F16-C1	Sept-09	F16 (Y-B)	195	10.53	2.053	2506	0.35±0.02	0.17±0.01
Average (without*)								0.22±0.02
Average (with*)								0.29±0.03

$0.22\pm0.02\mu g/m^3$ for samples excluding the polluted one, which is slightly higher than the average value of samples from Twin Otter.

3.4.1 C) Near-Surface Measurements at Halifax Downtown

The black carbon concentration found in the urban region (Halifax city area) during summer and winter are given in Table 3.9a and 3.9b. The concentration varies between 0.43 ± 0.02 $\mu g/m^3$ and 0.68 ± 0.03 $\mu g/m^3$ in summer, and between $1.14\pm0.06\mu g/m^3$ and $3.1\pm0.2\mu g/m^3$ in winter, which is an increase of a factor of 3 over the same region. Very likely the residential heating in winter contributes the additional black carbon.

The observed average black carbon concentration is about 0.54 ± 0.03 $\mu g/m^3$ in summer and 1.69 ± 0.08 $\mu g/m^3$ in winter. These are comparable to the black carbon concentrations found in other North American urban and rural areas as shown in Table 2.1 in Section 2.2. The mass fraction of black carbon to the total aerosol for the air samples in the Halifax area is about $0.9\pm0.2\%$ in summer, and $1.8\pm0.3\%$ in winter.

Table 3.9a   Black carbon in air samples from   Downtown
Halifax in   summer (1995)

Sample	Duration (min.)	Flowrate (l/min)	Total Volume (m^3)	Total B. C. (µg)	B.C. Conc. (µg/m^3)	TAM* (µg)	B.C / TAM*
aug-06-05	10022	0.578	5.79	3.9±0.2	0.68±0.03		
aug-06-12	10261	0.568	5.83	3.1±0.2	0.52±0.03		
aug-06-19	9845	0.534	5.25	3.0±0.2	0.57±0.03		
aug-06-26	11491	0.552	6.34	3.6±0.2	0.57±0.03		
aug-07-04	14397	0.517	7.44	3.6±0.2	0.48±0.02	449±40	0.80±0.05%
aug-07-14	10349	0.527	5.46	3.0±0.2	0.55±0.03		
aug-07-21	8349	0.522	4.36	2.9±0.2	0.66±0.03		
aug-07-27	11508	0.526	6.05	2.7±0.1	0.45±0.02		
aug-08-04	10063	0.523	5.26	3.2±0.2	0.60±0.03		
aug-08-11	10100	0.521	5.26	2.9±0.2	0.55±0.03	270±40	1.1±0.2%
aug-08-25	10093	0.522	5.27	2.3±0.1	0.43±0.02	292±40	0.8±0.1%
aug-09-01	10071	0.520	5.24	2.9±0.2	0.55±0.03		
aug-09-08	10177	0.520	5.29	2.4±0.1	0.46±0.02		
aug-09-15	9946	0.520	5.17	2.5±0.1	0.47±0.02		
aug-09-22	10193	0.520	5.30	2.7±0.1	0.51±0.03		
Average					0.54±0.03		0.9±0.2%

aug-:   Air sample from urban   area (downtown Halifax)   on ground level.

-06-05: Sampling date /-month-date

TAM*: Total Aerosol Mass

Table 3.9b Black carbon in air samples from Downtown Halifax in winter (1996)

Sample	Duration (min.)	Flowrate (l/min)	Total Volume (m³)	Total B. C. (μg)	B.C. Conc. (μg/m³)	TAM* (μg)	B.C. / TAM*
aug-02-05	10067	0.414	4.168	7.8±0.4	1.87±0.09		
aug-02-22	5669	1.139	6.457	8.3±0.4	1.29±0.06		
aug-03-11	4368	1.029	4.492	8.8±0.4	2.0±0.1		
aug-03-14	5677	1.012	5.742	8.3±0.4	1.45±0.07	720±15	1.20±0.06%
aug-03-19	1316	1.031	1.357	3.0±0.2	2.2±0.1		
aug-03-20	1464	1.031	1.509	3.0±0.1	2.0±0.1		
aug-03-21	1555	1.026	1.595	2.8±0.1	1.77±0.09	110±15	2.6±0.4%
aug-03-22	4139	1.038	4.296	7.2±0.4	1.68±0.08		
aug-03-25	1567	1.032	1.617	5.0±0.3	3.1±0.2	160±15	3.1±0.3%
aug-03-26	2855	1.023	2.921	5.0±0.3	1.70±0.08	140±15	3.5±0.4%
aug-03-28	1300	1.010	1.313	1.6±0.1	1.17±0.06	120±15	1.3±0.2%
aug-04-03	429	1.000	0.429	0.55±0.03	1.27±0.06		
aug-04-04	1096	1.010	1.104	1.26±0.07	1.14±0.06		
Average					1.69±0.08		1.8±0.3%

aug-s: Air sample from urban area (downtown Halifax) on ground level.

-02-05: Sampling date /-month-date

TAM*: Total Aerosol Mass

3.4.1 D) Effective Refractive Index of the Sampling Aerosols

The effective refractive index of the sampling aerosol can be estimated using the Bruggeman effective medium approximation expressed as Equation 2.1. Assuming the aerosols consist of black carbon, and soil represented by a refractive index of $m=1.5 - 8 \times 10^{-4}i$ (Pollack et al., 1976), and the black carbon particles are assumed randomly distributed among the soil particles, the effective refractive indices of this soil-black-carbon aerosol for different black carbon fractions at $\lambda = 0.55 \mu m$ are calculated and the results are listed in Table 3.10. The density difference between black carbon and the soil is neglected in the calculation, therefore the volume fraction of black carbon is the same as the mass fraction.

Table 3.10 Effective refractive index of the soil-black-carbon aerosol at different black carbon volume fractions (f_{bc})

f_{bc}	0.0	0.1%	0.5%	1%	2%
m_r	1.50	1.50	1.50	1.50	1.51
m_i	0.001	0.001	0.003	0.005	0.009

The imaginary effective refractive index of the aerosol ranges between 1.0×10^{-3} and 9.0×10^{-3} for the measured black carbon fractions (0.1% - 2%). These values fall in the range of the reported imaginary refractive index of the aerosols by various investigators (Patterson et al., 1977; Lindbergh and Laude, 1974).

3.4.2 Black Carbon Cloud Water Content from Twin Otter Flights

The black carbon concentration in marine stratus clouds listed in Table 3.11 generally varies from 4.0 ± 0.6 to 60 ± 3 μg/kg. The average value of black carbon in all cloud water samples collected is about $26 \pm 3 \mu$g of black carbon per kilogram of cloud water. The exceptionally high value of $220 \pm 10 \mu$g/kg was obtained from a cloud-haze mixed sample on September 9, 1996, which was a relatively high pollution day.

Columns 6 (FSSP) and 7 (FSSP Reff) in Table 3.11 show cloud droplet number density and the effective radius of the cloud droplets. The effective radius is defined as $r_{eff} = \int r^3 n(r) dr \, / \int r^2 n(r) dr$. The cloud droplet size distribution is measured with a PMS Forward scattering Spectrometer Probe (FSSP), which was mounted under the wing of the Twin Otter. Column 8 in Table 3.11 is the cloud liquid water content, which is measured with a PMS King heated-wire probe (Leaitch et al, 1996) mounted under the wing of the aircraft as well. The liquid water content ranges from 0.10 to 0.56g/m^3 over all the sampled clouds and the droplet number density varies from 40 to 483/cm^3.

The percentage of black carbon incorporated into clouds in the form of internal mixture can be obtained by comparing the black carbon concentration within the cloud water with the black carbon concentration in the near-sea surface air as measured on the Ferry at

Table 3.11 Black carbon in cloud water samples collected from Twin Otter

Sample	Date	Weight (g)	Average Altitude (m)	FSSP (cm⁻³)	FSSP Reff (µm)	King LWC (gm⁻³)	Pressue (mb)	Temp (C°)	Total B.C. (µg)	B.C. Conc. (µg / kg)
T04-C2	Aug-21	17.46	292	64	12.98	0.23	971.68	23.12	0.14±0.01	8.1±0.5
T04-C5	Aug-21	11.51	297	67	13.53	0.24	971.06	22.77	0.17±0.01	14.8±0.9
T06-C1	Aug-24	25.14	2482	483	7.82	0.56	741.5	4.03	0.27±0.01	10.9±0.6
T06-C2	Aug-24	27.13	2476	492	7.33	0.49	742.07	3.98	0.36±0.02	13.4±0.7
T08-C2	Aug-27	20.28	2386	114	9.68	0.30	757.51	7.85	0.13±0.01	6.5±0.4
T13-C8	Sept-01	7.95	924	318	7.35	0.18	896.41	14.11	0.26±0.02	33±2
T18-C1	Sept-08	5.72	1231	40	11.32	0.10	896.77	10.26	0.05±0.01	7.7±0.9
T18-C2	Sept-08	9.91	474	73	11.61	0.16	960.43	9.59	0.04±0.01	4.0±0.6
T19-C1*	Sept-09	16.29	650	200	9.20	0.24	940	15.60	0.67*±0.03	41*±2
T19-C2**	Sept-09	7.25	N/A	N/A	N/A	N/A	N/A	N/A	1.58***±0.08	220**±10
T21-C2	Sept-09	10.45	1401	367	8.08	0.33	856.69	12.68	0.35±0.02	34±2
T21-C5**	Sept-09	5.17	887	282	6.05	0.18	913.6	14.96	0.31**±0.02	60***±3
Average1 (without**)										16 ± 2
Average 2 (with **)										26 ± 3

Note: * -- Mixed sample of T19-C1, T19-C5, T19-C6 & T19-C7   ** -- Mixed haze & cloud sample   N/A -- Data are not available.

the same time.   Table 3.12 shows that only 1 to 5%   of black carbon is incorporated into clouds, which agrees with the NARE's result (Chylek et al., 1996) where an average of 9% was obtained. The results indicate that more than 90% of the black carbon is not internally mixed in the particles activated in cloud; i.e., most of the black carbon is outside of the water droplets. This fact has been observed before (Noone et al., 1992; Hallberg et al., 1992).

The cloud scavenging ratio, as defined in Section 2.2, can be use to quantify   the effectiveness of scavenging action of clouds. The scavenging ratio for the marine stratus cloud samples listed in the last column of Table 3.12 varies between 50 and 1050, which is well within the range of previous observations listed in   Table 2.3. The two maximum values of 1050   and 290 were obtained from   the haze-cloud mixture samples. This suggets that black carbon could be internally mixed in   particles too small   to be activated in cloud, such as in sulfate aerosol.

Table 3.12 Cloud scavenging ratio

Date	Flight	LWC g/m^3	BC in Cloud µg/kg	BC* LWC µg/m^3	Ferry Filter	BC in air µg/m^3	BC in an internal mixture	Scaveng -ing ratio
09-01	T13-C8	0.18	33	6.09E-3	F08-C1	0.69	0.9%	50
09-08	T18-C1	0.10	7.7	0.80E-3	F14-C1	0.06	1.3%	120
09-08	T18-C2	0.16	4.0	0.64E-3	F14-C1	0.06	1.0%	60
09-09	T19-C1	0.27	41	11.03E-3	F15-C1	0.21	5.3%	200
09-09	T19-C2	N/A	220	N/A	F15-C1	0.21	N/A	1050
09-09	T21-C2	0.33	33	11.04E-3	F15-C1	0.21	5.3%	160
09-09	T21-C5	0.18	60	10.71E-3	F15-C1	0.21	5.1%	290

3.4.3   Black Carbon   Rain Water Content

The black carbon concentrations in rain are given in Table 3.13a for the urban area and Table 3.13b   for the rural area.   The values fluctuate between an undetectable amount of black   carbon and 11.0 $\pm 0.6 \mu g/kg$.   Both results in Table 3.13a and b   show that there is no obvious trend in   the variation of black carbon concentration   during rainfall.   Averaging over all rain samples collected from the urban area yields a black carbon content about $3.8 \pm 0.3 \mu g/kg$, whereas the average   over all of the   rain   samples   collected in the rural area is $2.7 \pm 0.2 \mu g/kg$.   The black carbon concentration difference   between these two category rain samples   is likely caused by   local area pollution in the urban area.

By averaging over all of the rain samples,   the black carbon concentration   in rain is about $3.2 \pm 0.2 \mu g/kg$, which is considerably lower than the average black carbon concentration in cloud water $(26 \pm 3 \mu g/kg$: see Table 3.11).   It is also relatively low compared with the results $(20 - 600 \mu g/kg)$ obtained in Seattle and Sweden (Orgren et al., 1983; see Table 2.2a in Section 2.2).

The following shows the scheme for naming the rain and snow samples:

RG —   -10-   -15-   -02 -   - B   (A)

location / month   /date   /sample sequence /   with pre-filtration

(without pre-filtration)

Table 3.13a   Black carbon in rain samples from urban area

Sample	Date of sampling	Weight (g)	T.B.C. (μg)	B.C. C. (μg/kg)	Pre-filtration	Time sequence	Sample Duration
RL-06-07-02-A	June-07-95	39.25	0.16±0.01	4.1±0.3	N	N	20 min
RD-06-07-01-A	June-07-95	53.62	0.22±0.01	4.2±0.2	N	N	5h10min
RO-06-08-01-A	June-08-95	73.42	0.24±0.01	3.3±0.2	N	1	56 min
RO-06-08-02-A	June-08-95	72.92	0.67±0.03	9.2±0.5	N	2	55 min
RD-06-13-01-A	June-13-95	30.22	0.0±0.02	0.0	N	1	1h15min
RD-06-13-02-A	June-13-95	20.88	0.090±0.006	4.3±0.3	N	2	1h15min
RO-09-14-01-A	Sept-14-95	82.31	0.148±0.008	1.8±0.1	N	1	2h30min
RO-09-14-02-A	Sept-14-95	65.03	0.19±0.01	2.9±0.2	N	2	1h6min
RO-10-06-02-A	Oct-06-95	97.31	0.121±0.008	1.24±0.08	N	1	35 min
RO-10-06-03-A	Oct-06-95	57.45	0.64±0.03	11.1±0.6	N	2	1h20min
RO-04-02-01-B	April-02-96	75.03	0.26±0.02	3.5±0.2	Y	1	50 min
RO-04-02-02-B	April-02-96	169.16	0.79±0.04	4.7±0.2	Y	2	1h
RO-04-02-03-B	April-02-96	122.8	0.18±0.02	1.4±0.1	Y	3	40 min
RO-04-02-04-B	April-02-96	131.3	0.64±0.03	4.9±0.3	Y	4	35 min
RO-04-02-05-B	April-02-96	196.67	0.58±0.03	2.9±0.2	Y	5	45 min
Average				3.8±0.3			

Notation of rain sample:

RO -- rain sample from the roof of Dalhousie Oceanography building, Halifax, NS

RD -- rain sample from Dartmouth, NS

RL -- rain sample from LOYOLA Building, Halifax, NS

T.B.C. -- Total Black Carbon

B.C.C. -- Black Carbon Concentration

Table 3.13b Black carbon in rain samples from rural area

Sample	Date of sampling	Weight (g)	T.B.C. (μg)	B.C.C. (μg/kg)	Pre-filtration	Time sequence	Sample Duration
RG-08-24-01-A	Aug-24-95	42.3	0.17±0.01	4.1±0.2	N	N	58 min
RG-09-17-03-A	Sept-17-95	45.81	0.19±0.01	4.2±0.2	N	N	27/2 min
RG-09-17-03-B	Sept-17-95	45.16	0.112±0.007	2.5±0.2	Y	N	27/2 min
RG-10-06-01-A	Oct-06-95	21.94	0.00±0.02	0.0	N	1	1h18min
RG-10-06-02-A	Oct-06-95	69.03	0.00±0.01	0.0	N	2	4h17min
RG-10-06-05-A	Oct-06-95	83.22	0.00±0.02	0.0	N	3	49 min
RG-10-15-01-B	Oct-15-95	35.28	0.153±0.009	4.3±0.2	Y	1	1h21min
RG-10-15-02-B	Oct-15-95	73.09	0.00±0.02	0.0	Y	2	1h12min
RG-10-15-03-B	Oct-15-95	105.39	0.80±0.04	7.6±0.4	Y	3	26 min
RG-10-15-05-B	Oct-15-95	88.91	0.50±0.03	5.6±0.3	Y	4	33 min
RG-10-15-07-B	Oct-15-95	100.78	0.107±0.007	1.06±0.07	Y	5	1h10min
RG-10-15-09-B	Oct-15-95	48.04	0.149±0.009	3.10±0.2	Y	6	11h48min
RG-10-15-04-A	Oct-15-95	100.42	0.82±0.04	8.2±0.4	N	1	24 min
RG-10-15-06-A	Oct-15-95	85.46	0.060±0.005	0.70±0.06	N	2	49 min
RG-10-15-08-A	Oct-15-95	98.75	0.19±0.01	1.9±0.1	N	3	5h30min
RG-10-22-01-B	Oct-22-95	91.96	0.146±0.009	1.6±0.1	Y	1	23 min
RG-10-22-02-B	Oct-22-95	60.25	0.090±0.007	1.5±0.1	Y	2	~5h
RG-10-28-01-B	Oct-28-95	28.40	0.145±0.009	5.1±0.3	Y	N	~8h
RG-11-08-01-B	Nov-08-95	71.94	0.005±0.005	0.07±0.07	Y	N	31 min
RG-11-12-01-B	Nov-12-95	90.57	0.067±0.006	0.74±0.06	Y	N	~2.5h
Average				2.7±0.2			

Notation of rain sample:

RG -- rain sample from Bridgewater, NS
T.B.C. -- Total Black Carbon
B.C.C. -- Black Carbon Concentration

3.4.4 Black Carbon Content in Snow Samples

Table 3.14 shows the measured black carbon concentration in melted snow over both urban and rural areas. The value varies from $0.8\pm0.1\mu g/kg$ to $32\pm2\mu g/kg$ and the average over all the snow samples is $8.8\pm0.4\mu g/kg$, which is comparable to previously published data listed in Table 2.2a.

The scavenging ratio of snow, as defined in section 2.2, can be obtained by dividing the black carbon concentration in snow by the black carbon concentration in air. On average, the scavenging ratio of snow samples collected is about 10, which is lower than other previous measurements shown in Table 2.3. As in the rainfall case, it is hard to draw any conclusion about trend in variations of the black carbon concentration during snowfall from the available data in table 3.14, but it is noted that the average black carbon concentration in snow in the urban area $(10.1\pm0.5\mu g/m^3)$ is much higher than in the rural area $(1.7\pm0.2\mu g/m^3)$. The difference between the urban and rural is larger than for rain.

It should be mentioned that the snow samples, except SO-11-29-03-A and SO-01-30-03-A, are pre-filtered before passing through the quartz filter. There are some large $(>10\mu m)$ black carbon particles observed on the pre-filter when pre-filtering the urban snow samples. The final results shown on Table 3.14 do not include these large particles in the black carbon mass.

Table 3.14 Black carbon in snow samples

Sample	Date of sampling	Weight (g)	Total B.C. (μg)	B.C.conc. (μg/kg)	Pre-filtration	Time sequence
SO-11-29-01-B	Nov-29-95	159.47	1.9±0.1	12.1±0.6	Y	1
SO-11-29-02-B	Nov-29-95	92.56	0.90±0.05	9.7±0.5	Y	2
SO-11-29-03-A	Nov-29-95	138.03	1.52±0.08	11.0±0.6	N	3
SO-01-30-01-B	Jan-30-96	106.17	0.66±0.04	6.2±0.3	Y	N
SO-01-30-02-B	Jan-30-96	81.49	0.61±0.03	7.4±0.4	Y	N
SO-01-30-03-A	Jan-30-96	51.55	0.98±0.06	19±1	N	N
SO-02-03-03-B	Feb-03-96	254.63	1.10±0.06	4.3±0.2	Y	N
SO-02-06-01-B	Feb-06-96	147.08	4.7±0.2	32±2	Y	N
SO-03-08-01-B	Mar-08-96	176.28	1.05±0.05	6.0±0.3	Y	1
SO-03-08-02-B	Mar-08-96	218.05	1.77±0.09	8.1±0.4	Y	2
SO-03-08-03-B	Mar-08-96	152.28	0.76±0.05	5.0±0.3	Y	3
Average				10.1±0.5		
SG-01-30-01B	Jan-30-96	93.17	0.14±0.01	1.5±0.2	Y	N
SG-02-03-01-B	Feb-03-96	96.16	0.27±0.02	2.8±0.2	Y	N
SG-02-03-02B	Feb-03-96	102.15	0.08±0.01	0.8±0.1	Y	N
Average				1.7±0.2		

Notation of snow sample:

SO -- snow sample from the roof of Dalhousie Oceanography building, Halifax, NS.
SG -- snow sample from Bridgewater, NS.

Chapter 4

Radiative Effect: Black Carbon and Aerosols

4.1 Optical Properties of a Single Particle

A small particle interacts with incoming solar radiation through absorption and scattering of electromagnetic energy. The strength of this interaction is characterized by the absorption and scattering cross sections, σ_{abs} and σ_{sca}, which are determined by the complex refractive index, the size and the shape of the particle. The extinction cross section, σ_{ext}, is the sum of the absorption and scattering cross section:

$$\sigma_{ext} = \sigma_{abs} + \sigma_{sca} \qquad (4-1)$$

The single- scattering albedo, ω, is defined as

$$\omega = \frac{\sigma_{sca}}{\sigma_{ext}} \qquad (4-2)$$

which indicates the ratio of scattered radiation to the total extinction. The average cosine of the scattering angle (θ), or the asymmetry parameter g, is defined as

$$g = <\cos\theta> = \int_{4\pi} p(\theta)\cos\theta d\Omega \qquad (4\text{-}3)$$

where $p(\theta)$ is the scattering phase function, which specifies the angular distribution of scattered light and it is normalized as $\int_{4\pi} pd\Omega = 1$.

All the above parameters can be calculated exactly for homogeneous spheres using Mie scattering theory (Bohren and Huffman, 1983).

4.1.1 Single Scattering Properties of a Black Carbon Particle

The important property of black carbon in the atmosphere is its absorption of solar radiation. The strength of this absorption is commonly expressed in the form of specific absorption, which is defined as the absorption cross section of a given carbon particle divided by its mass (σ_{abs}/m). The measurements reported in the literature show that black carbon particles have a large specific absorption cross section of the order of $10m^2/g$ (Roessler and Faxvog, 1979; 1980; Truex and Anderson, 1979; Szkarlat and Japar, 1981).

The single scattering properties of a black carbon particle, including σ_{abs}/m, σ_{sca}/m, σ_{ext}/m, g and ω, can be calculated using a standard Mie scattering program if the black carbon particle is assumed to be spherical. Figure 4.1a and Figure 4.2a show the numerical results of σ_{abs}/m, σ_{sca}/m, and σ_{ext}/m as a function of the black carbon radius for different refractive index values. A black carbon density of

Figure 4.1a   Specific absorption cross section, specific scattering cross section and specific extinction cross section (in units of m^2/g) of black carbon particle as a function of radius for different imaginary refractive indices: $m_i=0.44$ (solid line), $m_i=0.60$ (dashed line), $m_i=0.80$ (dotted line), and $m_i=1.0$ (dashdot line) at $m_r=1.75$, $\rho=1.8g/cm^3$, and $\lambda=0.55\mu m$.

Figure 4.1b   Single scattering albedo and asymmetry parameter   of black carbon particle   as a function of   radius for   different imaginary refractive   index: m_i=0.44 (solid   line), m_i=0.60   (dashed   line), m_i=0.80 (dotted   line),   and m_i=1.0   (dashdot line)   at m_r=1.75, ρ= 1.8g/cm³, and λ=0.55μm.
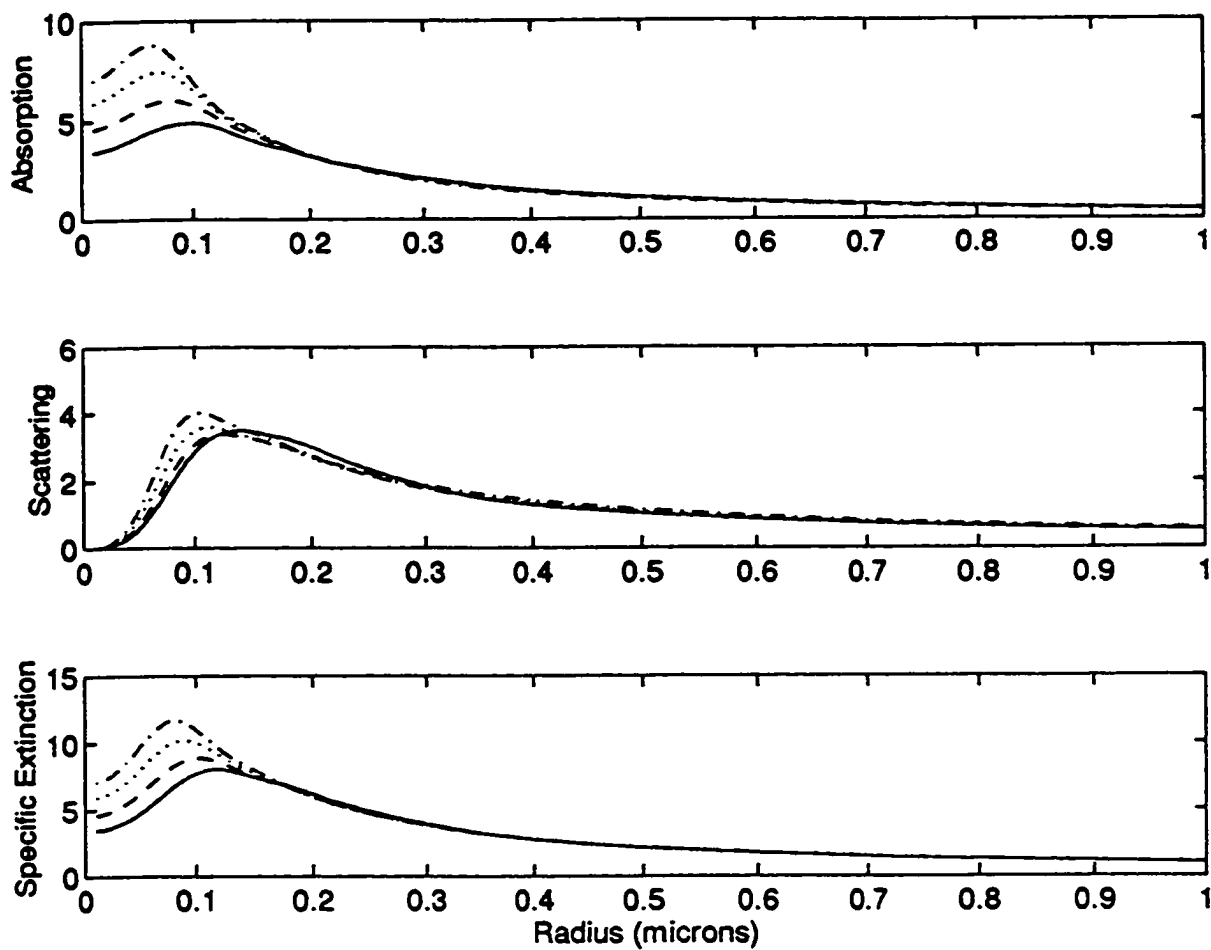
Figure 4.2a   Specific absorption cross section, specific scattering cross section and specific extinction cross section (in units of m^2/g) of black carbon particle as a function of radius for different   real refractive indices: $m_r=1.50$ (solid line), $m_r=1.75$ (dashed line),   and $m_r=1.85$ (dotted line) at $m_i=0.44$, $\rho=$ $1.8g/cm^3$, and $\lambda=0.55\mu m$.
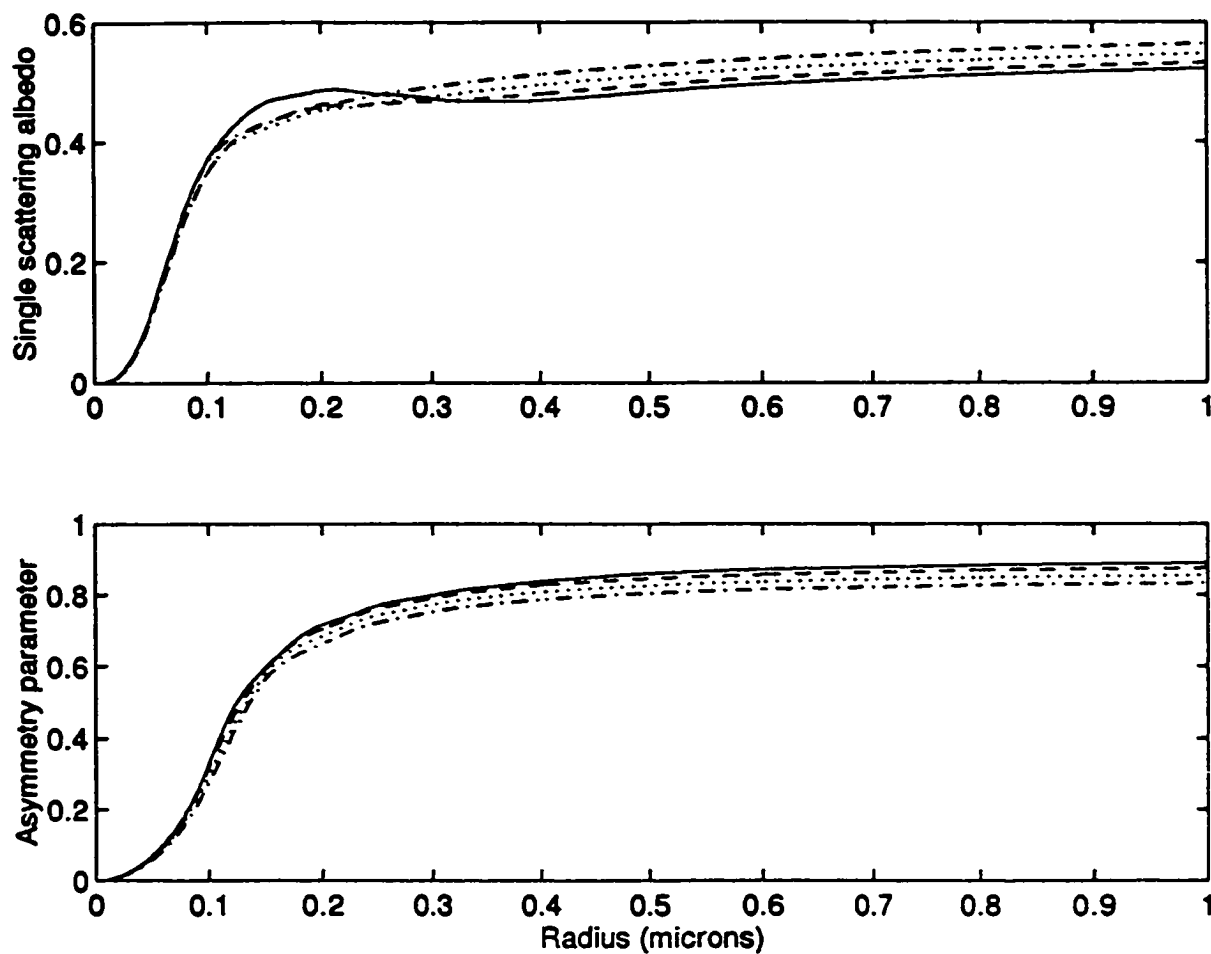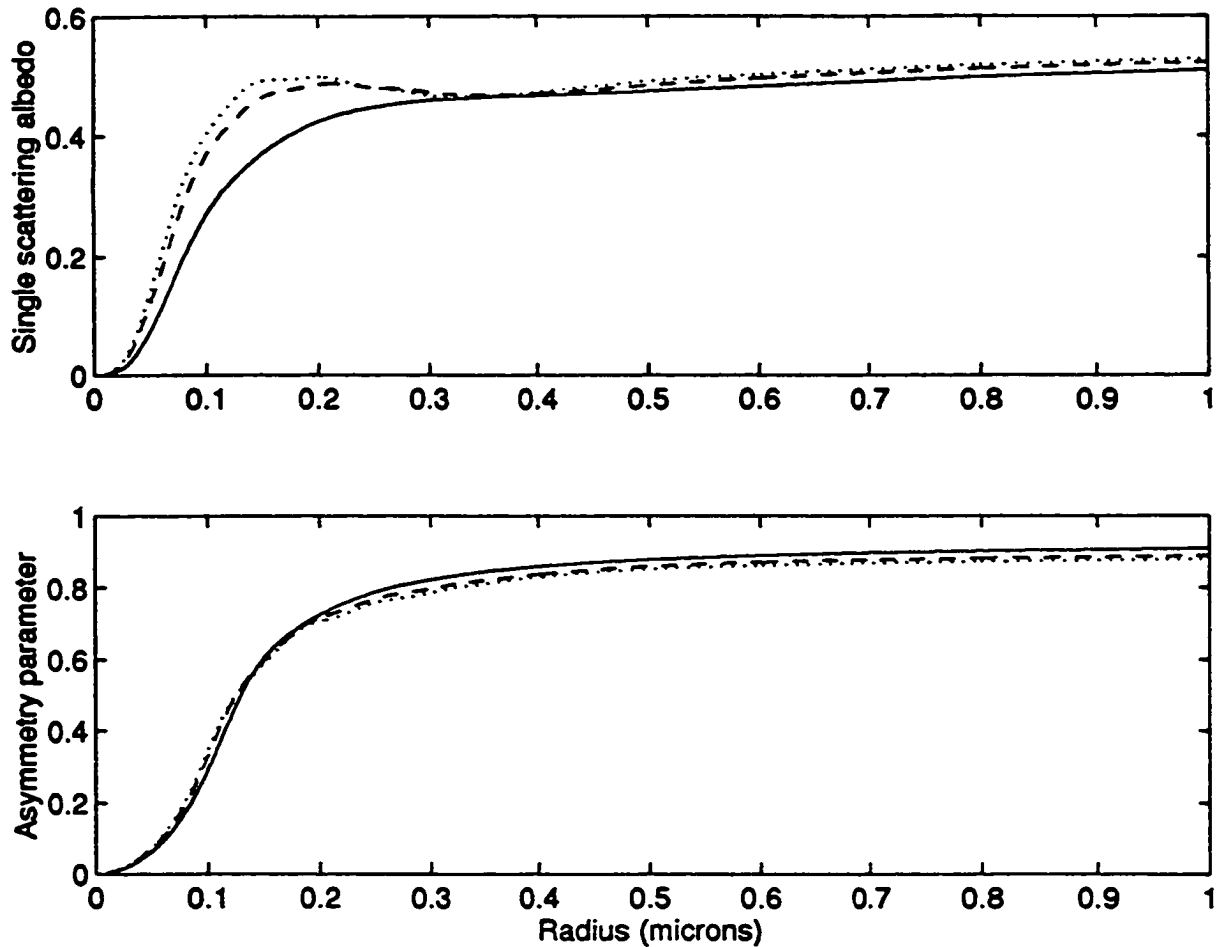
Figure 4.2b Single scattering albedo and asymmetry parameter of black carbon particle as a function of radius for different real refractive indices: m_r=1.50 (solid line), m_r=1.75 (dashed line), and m_r=1.85 (dotted line)   at m_i=0.44, ρ= $1.8g/cm^3$, and λ=0.55μm.

1.8g/cm^3 and a wavelength of $\lambda=$ 0.55μm are used in the calculations. It can be seen from the Figures that the position of the absorption peak and the peak value are more sensitive to the imaginary part of the refractive index than the real part. With higher imaginary refractive index, the peak moves toward the smaller size particles and has higher value. The specific absorption of the black carbon particle decreases very rapidly with increasing radius after the peak (around 0.1μm) until r = 1μm. It remains almost constant for the larger radius (r>1μm) section. Thus, larger homogeneous spherical black carbon particles are much less efficient absorbers of solar radiation. This effect is due to the small skin depth ($\delta= \lambda/2\pi m_i$) of black carbon.

For particles much larger than the skin depth, the efficiency of absorbing light is reduced. It can be seen from Figure 4.1b and Figure 4.2b that both single scattering albedo and asymmetry parameter show very small dependence with the refractive index.

The dependence of specific absorption, scattering and extinction cross sections on the mass density of black carbon is shown in Figure 4.3. The lower mass density of black carbon yields the higher specific absorption and scattering cross section. The single scattering albedo and asymmetry parameter only depend on the radius, wavelength and the refractive index. Therefore, there is no variation of ω and g expected with the different values of mass density. It can be seen from Figure 4.4a and Figure 4.4b that σ_{abs}/m, σ_{sca}/m, σ_{ext}/m, g and ω, show a very sensitive dependence on the incident wavelengths. All the parameters have the highest values at visible wavelengths.
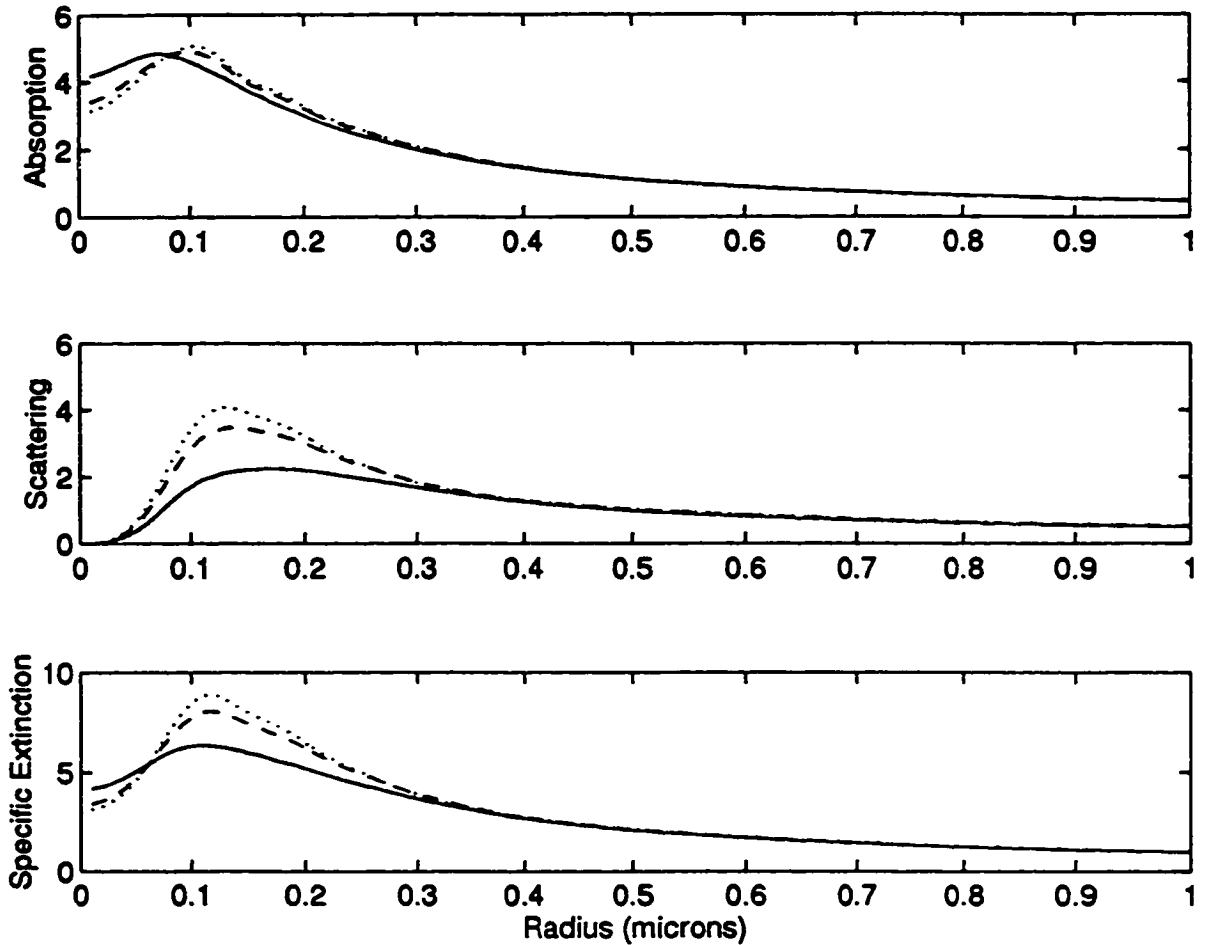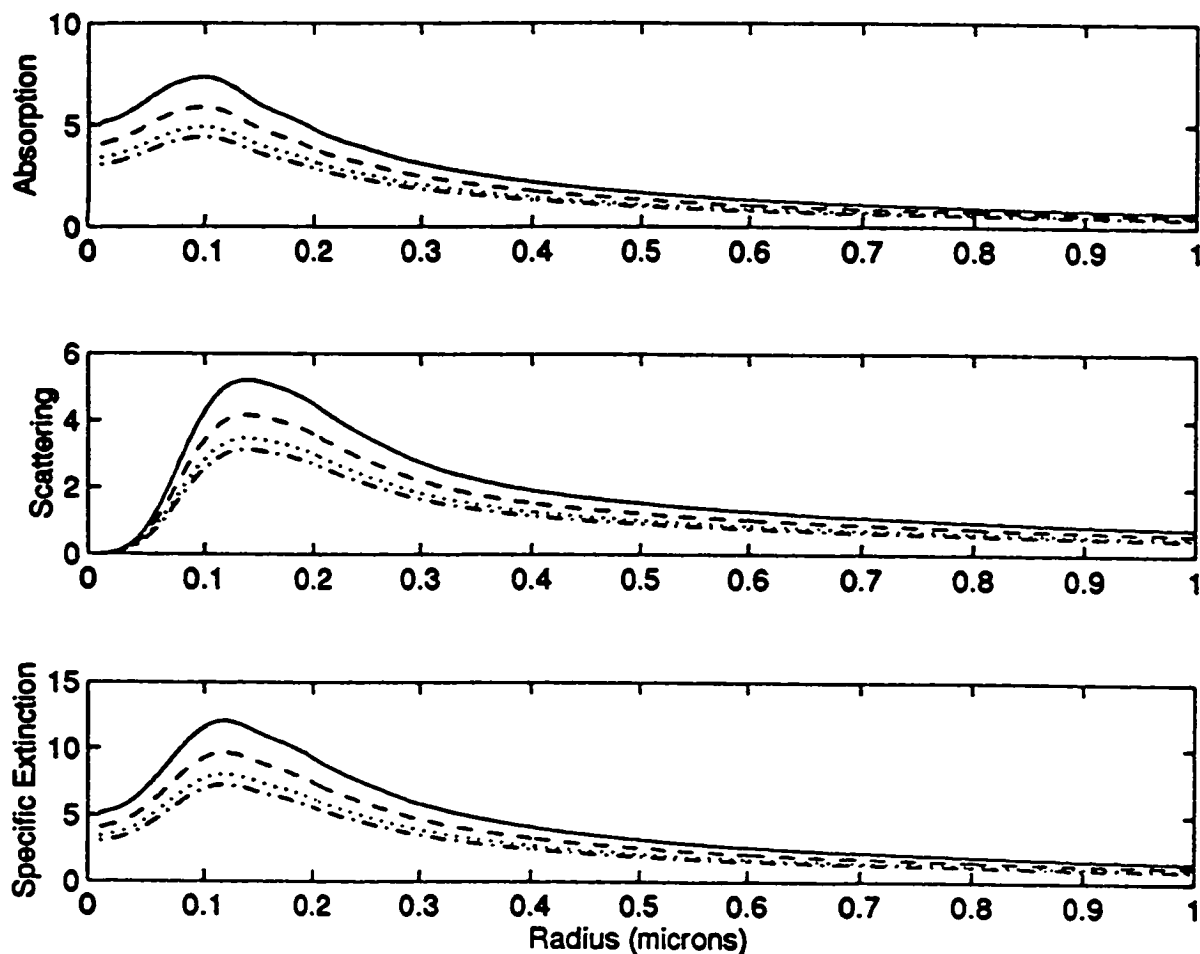
Figure 4.3 Specific absorption cross section, specific scattering cross section and specific extinction cross section (in units of m^2/g) of black carbon particle as a function of radius for different black carbon mass densities: $\rho=1.2g/cm^3$ (solid line), $\rho=1.5g/cm^3$ (dashed line), $\rho=1.8g/cm^3$ (dotted line) and $\rho=2.0g/cm^3$ (dashdot line) at m= 1.75 - 0.44i and $\lambda=0.55\mu m$.
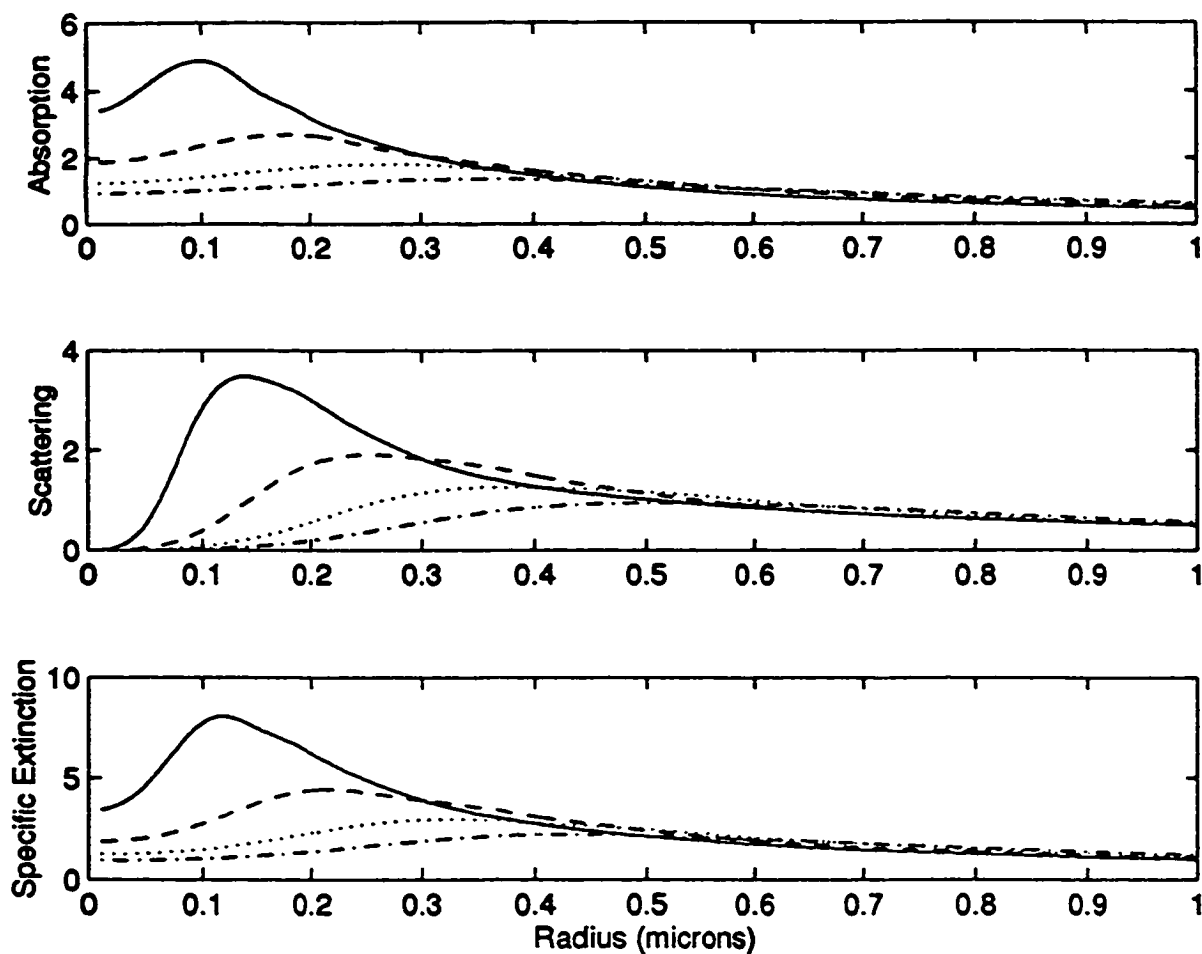
Figure 4.4a   Specific absorption cross section, specific scattering cross section and specific extinction cross section (in units of m^2/g) of black carbon particle as a function of radius for different incident wavelengths: $\lambda=$ 0.55μm (solid line), $\lambda=$ 1.0μm (dashed line), $\lambda=$ 1.5μm (dotted line) and $\lambda=$ 2.0μm (dashdot line) at m= 1.75 - 0.44i and $\rho=$1.8g/cm^3.

Figure 4.4b Single scattering albedo and asymmetry parameter of black carbon particle as a function of radius for different incident wavelengths: $\lambda = 0.55\mu m$ (solid line), $\lambda = 1.0\mu m$ (dashed line), $\lambda = 1.5\mu m$ (dotted line) and $\lambda = 2.0\mu m$ (dashdot line) at $m = 1.75 - 0.44i$ and $\rho = 1.8 g/cm^3$.

4.1.2 Single Scattering Properties of Sulfate and Sulfate-Black Carbon Aerosols

Sulfate aerosols are amoung the most dominant species in the atmosphere. The oxidation of sulfur-containing gases in the atmosphere ends as sulfate. The refractive index values of sulfate are not yet available, they have been assumed to be equal to those of sulfuric acid solution (d'Almeida et al., 1991; Chylek et al., 1995b). Figure 4.5a and Figure 4.5b show the imaginary and real refractive index of a 75% H_2SO_4 solution as a function of wavelength in the solar region obtained from Palmer and Williams (1975). It can be seen from Figure 4.5a and 4.5b that the real part of the refractive index varies by a few percent, while the imaginary part of the refractive index runs through several orders of magnitude in the solar spectral region.

As for black carbon particles, the single scattering properties of a sulfate particle can be calculated using Mie scattering program if we assume the sulfate particle to be spherical. Figure 4.6a and Figure 4.6b show the numerical results of σ_{abs}/m, σ_{sca}/m, σ_{ext}/m, ω and g as a function of the sulfate aerosol radius for different incident wavelengths. A sulfate mass density of $1.8g/cm^3$ is used in the calculations. As in the case of the black carbon particle, all the parameters of sulfate aerosol exhibit a strong dependence on incident wavelengths. It can be seen from Figure 4.6a that the
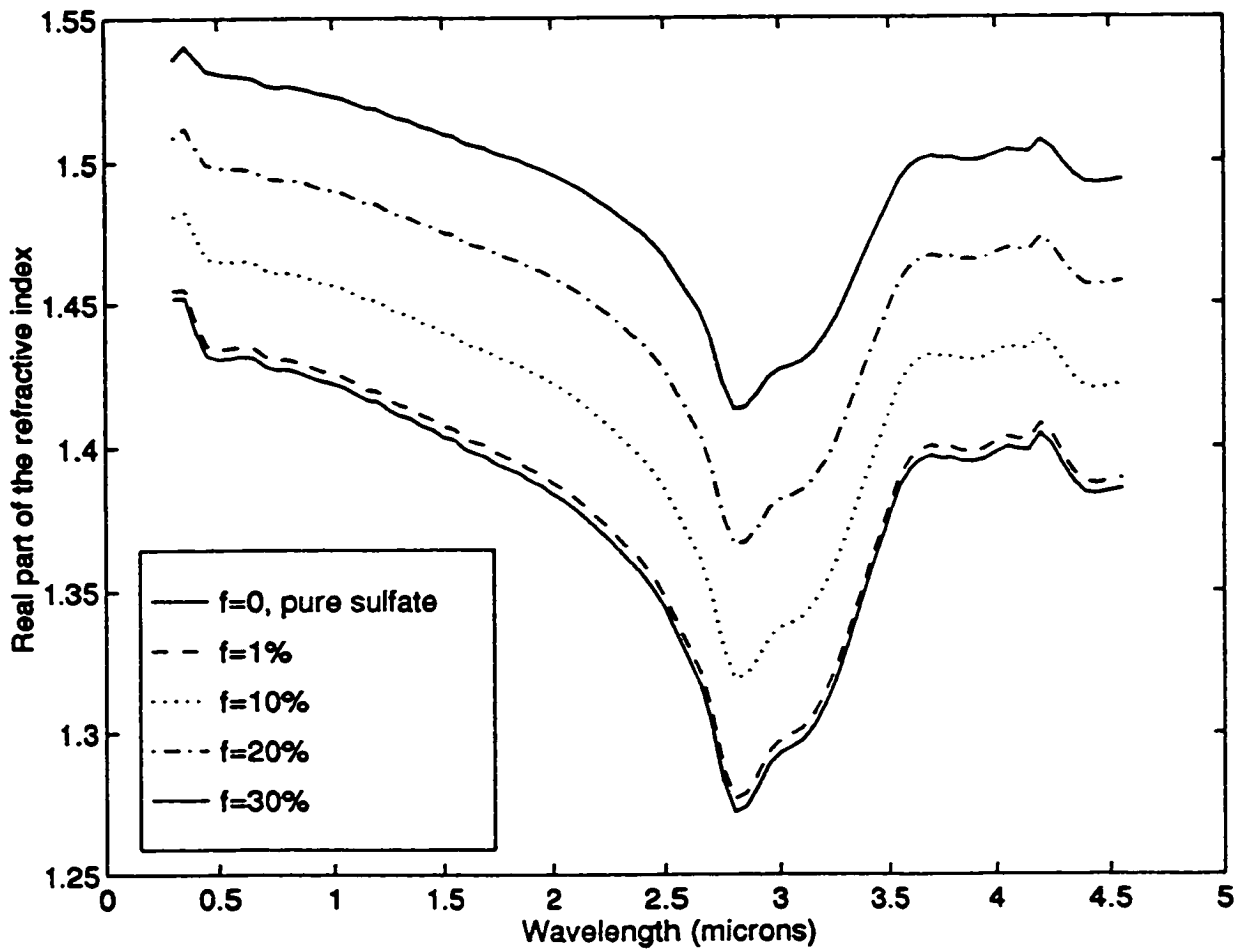
Figure 4.5a The real part of the refractive index of sulfate-black-carbon as a function of wavelength for different black carbon volume fractions: f=0, pure sulfate (lower solid line); f=1% (dashed line); f=10% (dotted line); f=20% (dashdot); f=30% (upper solid line).
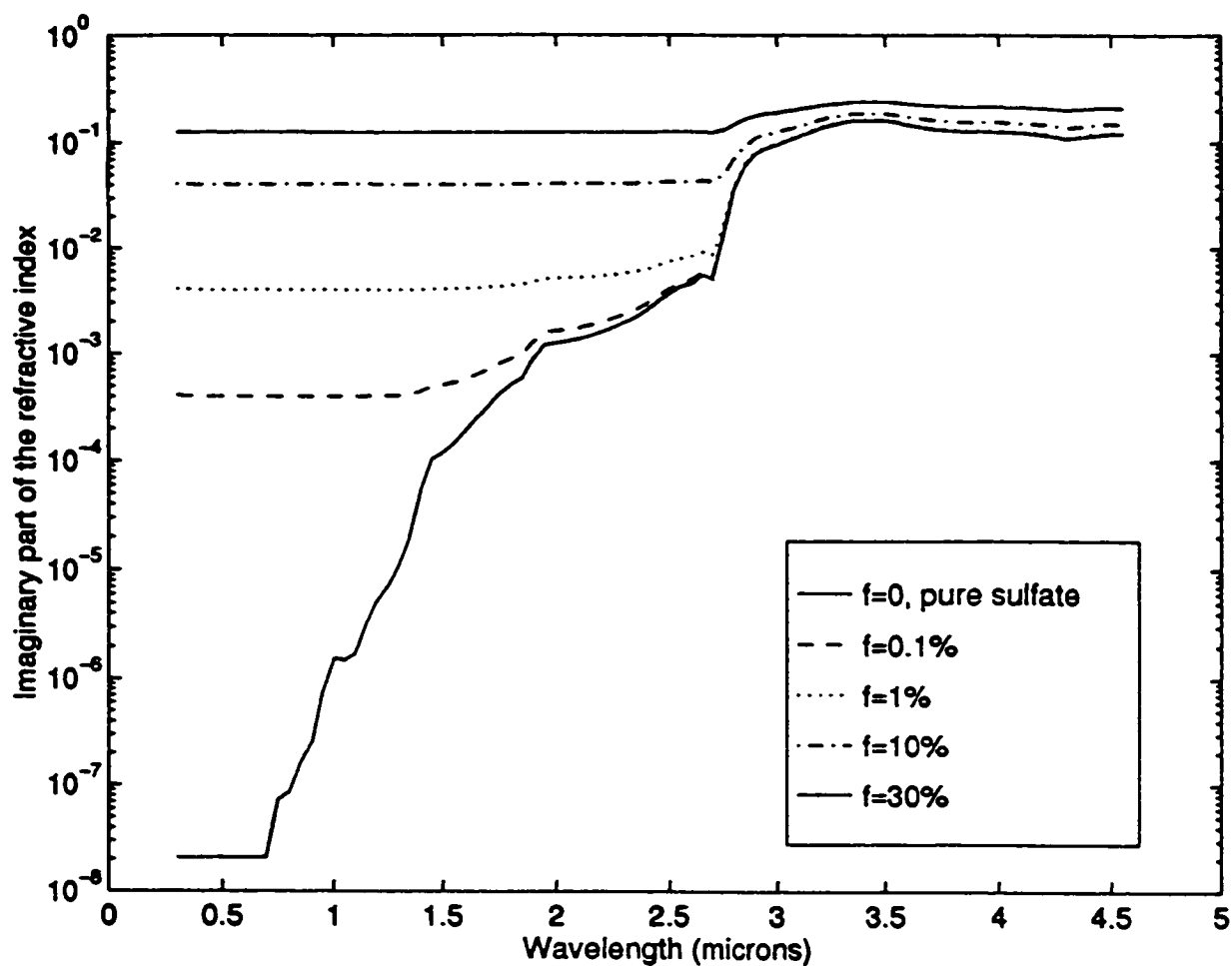
Figure 4.5b The imaginary refractive index of sulfate-black-carbon as a function of wavelength for different black carbon volume fractions: f=0, pure sulfate (lower solid line); f=0.1% (dashed line); f=1% (dotted line); f=10% (dashdot); f=30% (upper solid line).

Figure 4.6a   Specific absorption cross section, specific scattering cross section and specific extinction cross section (in units of m^2/g) of sulfate aerosol as a function of radius for different incident wavelengths: λ= 0.55μm (solid line), λ= 1.0μm (dashed line), λ= 1.5μm (dotted line) and λ= 2.0μm (dashdot line) at ρ=1.8g/cm^3.
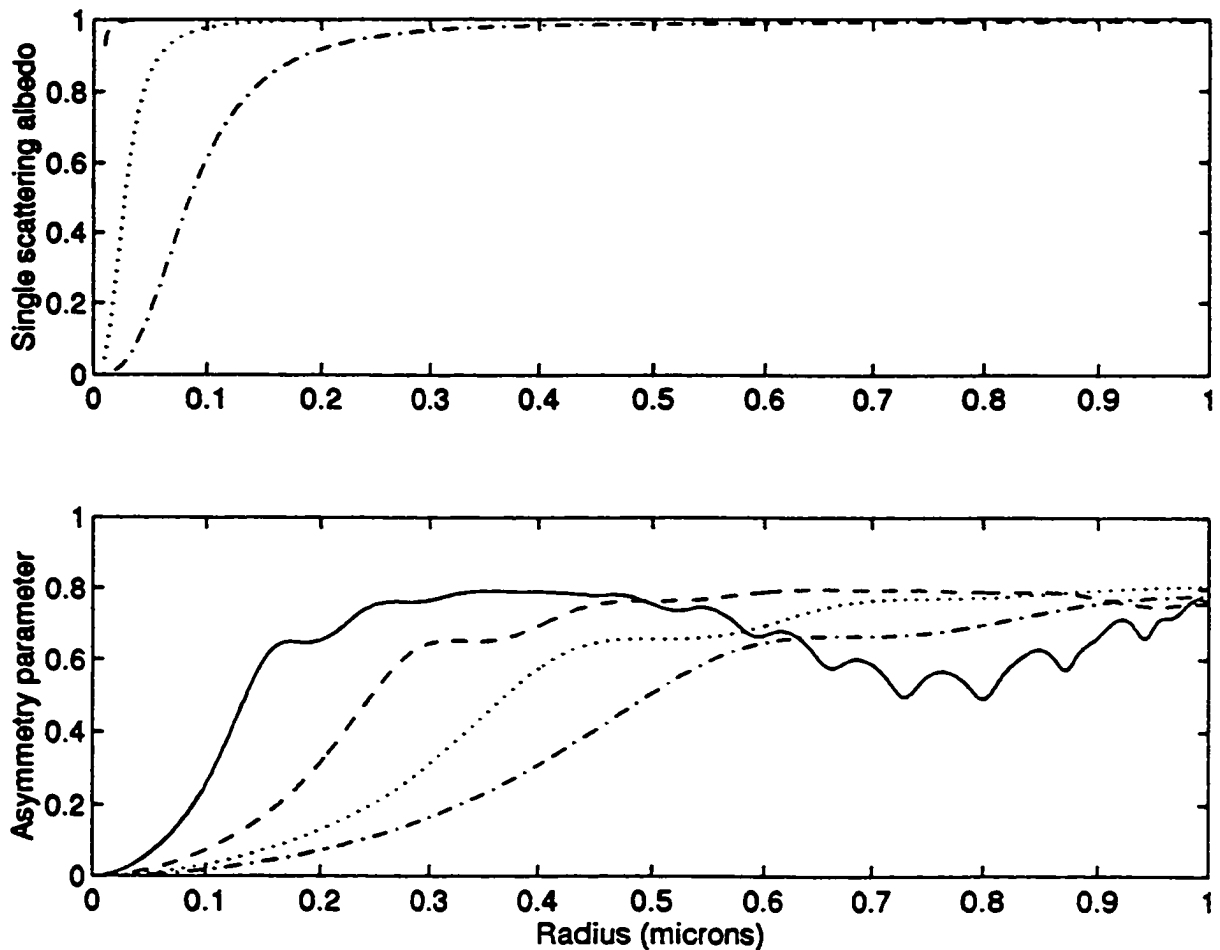
Figure 4.6b Single scattering albedo and asymmetry parameter of sulfate aerosol as a function of radius for different incident wavelengths: λ= 0.55μm (solid line), λ= 1.0μm (dashed line), λ= 1.5μm (dotted line) and λ= 2.0μm (dashdot line) at ρ=1.8g/cm^3.

specific extinction cross section is dominated by the specific scattering cross section. The contribution of absorption is very small. The weak absorption property of sulfate aerosol is also shown in Figure 4.6b, where the single scattering albedo is almost equal to one at shorter wavelengths.

The measurement results in Chapter 3 indicate that black carbon can be internally mixed in small aerosol particles which are too small to be activated, such as sulfate aerosols. If we consider the aerosol to consist of a black carbon grain incorporated inside a sulfate aerosol and dispered randomly, the effective refractive index of such a sulfate-black-carbon aerosol with a black carbon fraction f can be calculated from the Bruggeman effective medium approximation (see Section 2.3.2). Figure 4.5a and 4.5b show the refractive index of the sulfate-black-carbon composite aerosol as a function of wavelength in the solar spectral region. Because a density of $1.8g/cm^3$ is used for both sulfate and black carbon, the volume fraction is equal to the mass fraction as well. It can be seen that black carbon inclusions in sulfate aerosols affect the sulfate refractive index significantly. The imaginary refractive index of the composite aerosol increases with black carbon fraction, ultimately aproaching the value of 0.44 corresponding to a pure black carbon aerosol. It is noteworthy that even for a black carbon fraction as small as 0.1%, the imaginary refractive index is 10^{-4} at visible wavelengths. This is a jump of almost 4 orders of magnitude from the imaginary refractive index of pure sulfate aerosol. The largest

difference occurs across the visible part of the solar spectrum, where sulfates have negligible absorption. Just as for the pure black carbon and sulfate aerosols, the single scattering properties of the sulfate-black-carbon aerosol, including specific absorption, scattering, and extinction cross sections, single scattering albedo, and asymmetry parameter, can be obtained using Mie theory.

4.2 Optical Properties of a Layer of Black Carbon Aerosols

The extinction, scattering, and absorption coefficients, K_{ext}, K_{sca}, and K_{abs}, for a layer of aerosols, are defined as the corresponding cross sections (σ_{ext}, σ_{sca}, and σ_{abs}) of the individual particles integrated over a size distribution $n(r)$; ie,

$$K_{ext} = \int \sigma_{ext} n(r) dr,$$

$$K_{sca} = \int \sigma_{sca} n(r) dr,$$

$$K_{abs} = \int \sigma_{abs} n(r) dr. \qquad (4\text{-}4)$$

All of the coefficients have units of $[m]^{-1}$, and indicate the attenuation of the incident radiation as it passes through the layer. The single scattering albedo is $\omega = K_{sca} / K_{ext}$. The specific absorption and specific scattering coefficients are defined as the corresponding coefficient divided by the mass density M of the aerosol in the aerosol layer, and are denoted Ψ_{abs} and Ψ_{sca}, respectively. The

mass density is the integral of the mass over the size distribution and has units of micrograms per cubic meter.

$$M = \frac{4\pi\rho}{3} \int r^3 n(r) dr$$

where ρ is the density (gram/cm^3) of the aerosol material. If n(r) is a log-normal function, M can be obtained as

$$M = \frac{4\pi\rho}{3} \{N_0 \, r_g^3 \exp[\frac{(3\ln\sigma)^2}{2}]\}. \qquad (4\text{-}5)$$

The optical depth of the aerosol layer, τ, is defined as the integration of the corresponding coefficient over a path length through the atmosphere. For the case of an uniformly distributed aerosol layer of depth ΔZ, the optical depth can be obtained as

$$\tau_{ext} = \Delta Z \, K_{ext},$$

$$\tau_{sca} = \Delta Z \, K_{sca},$$

$$\tau_{abs} = \Delta Z \, K_{abs}, \qquad (4\text{-}6)$$

where $\tau_{ext} = \tau_{sca} + \tau_{abs}$. Using specific coefficients instead of the general coefficients, the optical depth can be expressed in another form:

$$\tau_{ext} = L \, K_{ext}/M = L \, \Psi_{ext},$$

$$\tau_{sca} = L \, K_{sca}/M = L \, \Psi_{sca},$$

$$\tau_{abs} = L \, K_{abs}/M = L \, \Psi_{abs}, \qquad (4\text{-}7)$$

where L (L= ΔZ M) is the aerosol loading with units of $\mu g/m^2$.

The bulk asymmetry factor, G, is defined as

$$G = \frac{1}{K_{sca}} \int g(r) \sigma_{sca} n(r) dr \, , \qquad (4\text{-}8)$$

where g is the asymmetry parameter for an individual particle of radius r. The isotropic back-scattering fraction, B, is related to G by an approximation relation (Wiscombe and Grams, 1976):

$$B = \frac{1}{2} (1 - \frac{7G}{8}). \qquad (4\text{-}9)$$

To reduce the computational time, the entire solar radiation spectrum is divided into 14 bands (Winter 1994), which is listed in Table 4.1. The average values of refractive index of sulfate and sulfate-black-carbon aerosols at each individual band for different black carbon fractions are listed in Table 4.1 as well.

Table 4.2a - d lists the calculated optical parameters, including Ψ_{ext}, Ψ_{sca}, Ψ_{abs}, ω, G, and B, for black carbon particles with mean radii of $r=0.05\mu m$ and $r=0.10\mu m$ at $\sigma=1.5$ and $\sigma=1.1$. Some of the optical parameters are also presented graphically in Figure 4.7a and Figure 4.7b.

It can be seen from Figure 4.7a that both Ψ_{abs} and Ψ_{sca} show a very dramatic decrease in the wavelength region of $0.5\mu m$ to $2\mu m$. Relatively speaking, the size dependence of the specific absorption coefficient is smaller than the specific scattering coefficient. Ψ_{sca} has a higher value for larger size particles at a fixed wavelength.

Table 4.1 The average effective refractive index of a sulfate-black-carbon aerosol in the solar spectral bands at different black carbon fractions (f=0 is for sulfate aerosol)

Band	Range(μm)	Mid-point	f=0		f=1%		f=5%		f=30%	
			n	k	n	k	n	k	n	k
1	0.3 - 0.5	0.4	1.44	2.07E-08	1.45	4.03E-03	1.46	2.03E-02	1.54	1.25E-01
2	0.5 - 0.7	0.6	1.43	2.07E-08	1.43	4.00E-03	1.45	2.01E-02	1.53	1.25E-01
3	0.7 - 0.9	0.8	1.43	1.01E-07	1.43	4.00E-03	1.44	2.01E-02	1.53	1.25E-01
4	0.9 - 1.1	1.0	1.42	1.12E-06	1.43	3.98E-03	1.44	2.00E-02	1.52	1.24E-01
5	1.1 - 1.35	1.23	1.41	8.45E-06	1.42	3.97E-03	1.43	2.00E-02	1.52	1.24E-01
6	1.35 - 1.45	1.4	1.41	5.60E-05	1.41	4.01E-03	1.43	2.00E-02	1.51	1.24E-01
7	1.45 - 1.75	1.6	1.40	2.10E-04	1.40	4.15E-03	1.42	2.00E-02	1.51	4.15E-01
8	1.75 - 1.95	1.85	1.39	7.41E-04	1.39	4.64E-03	1.41	2.04E-02	1.50	1.24E-01
9	1.95 - 2.1	2.03	1.38	1.29E-03	1.39	5.17E-03	1.40	2.09E-02	1.50	1.24E-01
10	2.1 - 2.3	2.2	1.37	1.57E-03	1.38	5.49E-03	1.39	2.11E-02	1.49	1.24E-01
11	2.3 - 2.5	2.4	1.36	2.62E-03	1.36	6.53E-03	1.38	2.20E-02	1.48	1.25E-01
12	2.5 - 2.9	2.7	1.30	3.94E-02	1.31	2.71E-02	1.33	4.14E-02	1.44	1.38E-01
13	2.9 - 3.3	3.1	1.30	1.07E-01	1.31	1.18E-01	1.32	1.29E-01	1.43	2.05E-01
14	3.3 - 4.0	3.65	1.38	1.40E-01	1.39	1.45E-01	1.40	1.56E-01	1.49	2.26E-01

Table 4.2a Optical parameters of BC particles (r_g=0.05μm, σ=1.5)

Band	Ψ_{ext} m²/kg	Ψ_{sca} m²/kg	Ψ_{abs} m²/kg	ω	G	B
1	9.536E+03	3.605E+03	5.931E+03	3.780E-01	4.582E-01	2.995E-01
2	5.628E+03	1.569E+03	4.060E+03	2.787E-01	3.082E-01	3.652E-01
3	3.611E+03	7.010E+02	2.910E+03	1.941E-01	2.089E-01	4.086E-01
4	2.549E+03	3.353E+02	2.214E+03	1.315E-01	1.424E-01	4.377E-01
5	1.888E+03	1.601E+02	1.728E+03	8.480E-02	9.594E-02	4.580E-01
6	1.569E+03	9.597E+01	1.473E+03	6.118E-02	7.341E-02	4.679E-01
7	1.316E+03	5.682E+01	1.260E+03	4.316E-02	5.610E-02	4.755E-01
8	1.099E+03	3.187E+01	1.067E+03	2.900E-02	4.190E-02	4.817E-01
9	9.865E+02	2.219E+01	9.643E+02	2.249E-02	3.495E-02	4.847E-01
10	8.959E+02	1.591E+01	8.800E+02	1.776E-02	2.960E-02	4.871E-01
11	8.115E+02	1.121E+01	8.003E+02	1.381E-02	2.487E-02	4.891E-01
12	7.120E+02	6.979E+00	7.050E+02	9.802E-03	1.965E-02	4.914E-01
13	6.129E+02	4.003E+00	6.089E+02	6.531E-03	1.491E-02	4.935E-01
14	5.153E+02	2.076E+00	5.132E+02	4.028E-03	1.076E-02	4.953E-01

Table 4.2b Optical parameters of BC particles (r_g=0.05μm, σ=1.1)

Band	Ψ_{ext} m²/kg	Ψ_{sca} m²/kg	Ψ_{abs} m²/kg	ω	G	B
1	8.363E+03	2.026E+03	6.337E+03	2.423E-01	1.610E-01	4.295E-01
2	4.184E+03	4.416E+02	3.742E+03	1.056E-01	6.828E-02	4.701E-01
3	2.754E+03	1.398E+02	2.614E+03	5.075E-02	3.819E-02	4.833E-01
4	2.068E+03	5.688E+01	2.011E+03	2.751E-02	2.445E-02	4.893E-01
5	1.626E+03	2.511E+01	1.601E+03	1.545E-02	1.632E-02	4.929E-01
6	1.398E+03	1.467E+01	1.383E+03	1.050E-02	1.251E-02	4.945E-01
7	1.207E+03	8.578E+00	1.199E+03	7.105E-03	9.584E-03	4.958E-01
8	1.033E+03	4.787E+00	1.028E+03	4.635E-03	7.175E-03	4.969E-01
9	9.388E+02	3.339E+00	9.355E+02	3.548E-03	5.991E-03	4.974E-01
10	8.607E+02	2.389E+00	8.583E+02	2.775E-03	5.078E-03	4.978E-01
11	7.862E+02	1.685E+00	7.845E+02	2.143E-03	4.268E-03	4.981E-01
12	6.962E+02	1.051E+00	6.951E+02	1.509E-03	3.374E-03	4.985E-01
13	6.043E+02	6.041E-01	6.037E+02	9.997E-04	2.560E-03	4.989E-01
14	5.117E+02	3.141E-01	5.114E+02	6.137E-04	1.848E-03	4.992E-01

Table 4.2c Optical parameters of BC particles (r_g=0.10μm, σ=1.5)

Band	Ψ_{ext} m²/kg	Ψ_{sca} m²/kg	Ψ_{abs} m²/kg	ω	G	B
1	7.459E+03	3.456E+03	4.004E+03	4.632E-01	6.807E-01	2.022E-01
2	6.172E+03	2.630E+03	3.542E+03	4.262E-01	5.598E-01	2.551E-01
3	4.768E+03	1.802E+03	2.966E+03	3.780E-01	4.582E-01	2.995E-01
4	3.640E+03	1.192E+03	2.448E+03	3.275E-01	3.754E-01	3.358E-01
5	2.729E+03	7.446E+02	1.985E+03	2.728E-01	3.007E-01	3.685E-01
6	2.226E+03	5.204E+02	1.705E+03	2.338E-01	2.535E-01	3.891E-01
7	1.805E+03	3.505E+02	1.455E+03	1.941E-01	2.089E-01	4.086E-01
8	1.438E+03	2.191E+02	1.219E+03	1.524E-01	1.641E-01	4.282E-01
9	1.251E+03	1.605E+02	1.090E+03	1.283E-01	1.391E-01	4.392E-01
10	1.104E+03	1.193E+02	9.848E+02	1.081E-01	1.187E-01	4.481E-01
11	9.723E+02	8.650E+01	8.858E+02	8.897E-02	9.996E-02	4.563E-01
12	8.241E+02	5.524E+01	7.689E+02	6.703E-02	7.898E-02	4.655E-01
13	6.856E+02	3.221E+01	6.534E+02	4.697E-02	5.980E-02	4.738E-01
14	5.586E+02	1.683E+01	5.418E+02	3.012E-02	4.306E-02	4.812E-01

Table 4.2d Optical parameters of BC particles (r_g=0.10μm, σ=1.1)

Band	Ψ_{ext} m²/kg	Ψ_{sca} m²/kg	Ψ_{abs} m²/kg	ω	G	B
1	1.046E+04	4.707E+03	5.754E+03	4.500E-01	5.650E-01	2.528E-01
2	6.817E+03	2.383E+03	4.434E+03	3.495E-01	3.051E-01	3.665E-01
3	4.182E+03	1.013E+03	3.169E+03	2.423E-01	1.611E-01	4.295E-01
4	2.821E+03	4.492E+02	2.372E+03	1.592E-01	9.959E-02	4.564E-01
5	2.026E+03	2.035E+02	1.822E+03	1.005E-01	6.547E-02	4.714E-01
6	1.659E+03	1.195E+02	1.539E+03	7.202E-02	4.995E-02	4.782E-01
7	1.377E+03	6.988E+01	1.307E+03	5.075E-02	3.819E-02	4.833E-01
8	1.139E+03	3.894E+01	1.100E+03	3.418E-02	2.857E-02	4.875E-01
9	1.018E+03	2.705E+01	9.914E+02	2.656E-02	2.386E-02	4.896E-01
10	9.218E+02	1.937E+01	9.024E+02	2.102E-02	2.022E-02	4.912E-01
11	8.325E+02	1.364E+01	8.189E+02	1.639E-02	1.700E-02	4.926E-01
12	7.280E+02	8.493E+00	7.196E+02	1.167E-02	1.345E-02	4.941E-01
13	6.249E+02	6.249E+02	6.200E+02	7.798E-03	1.021E-02	4.955E-01
14	5.240E+02	2.528E+00	5.215E+02	4.824E-03	7.372E-03	4.968E-01

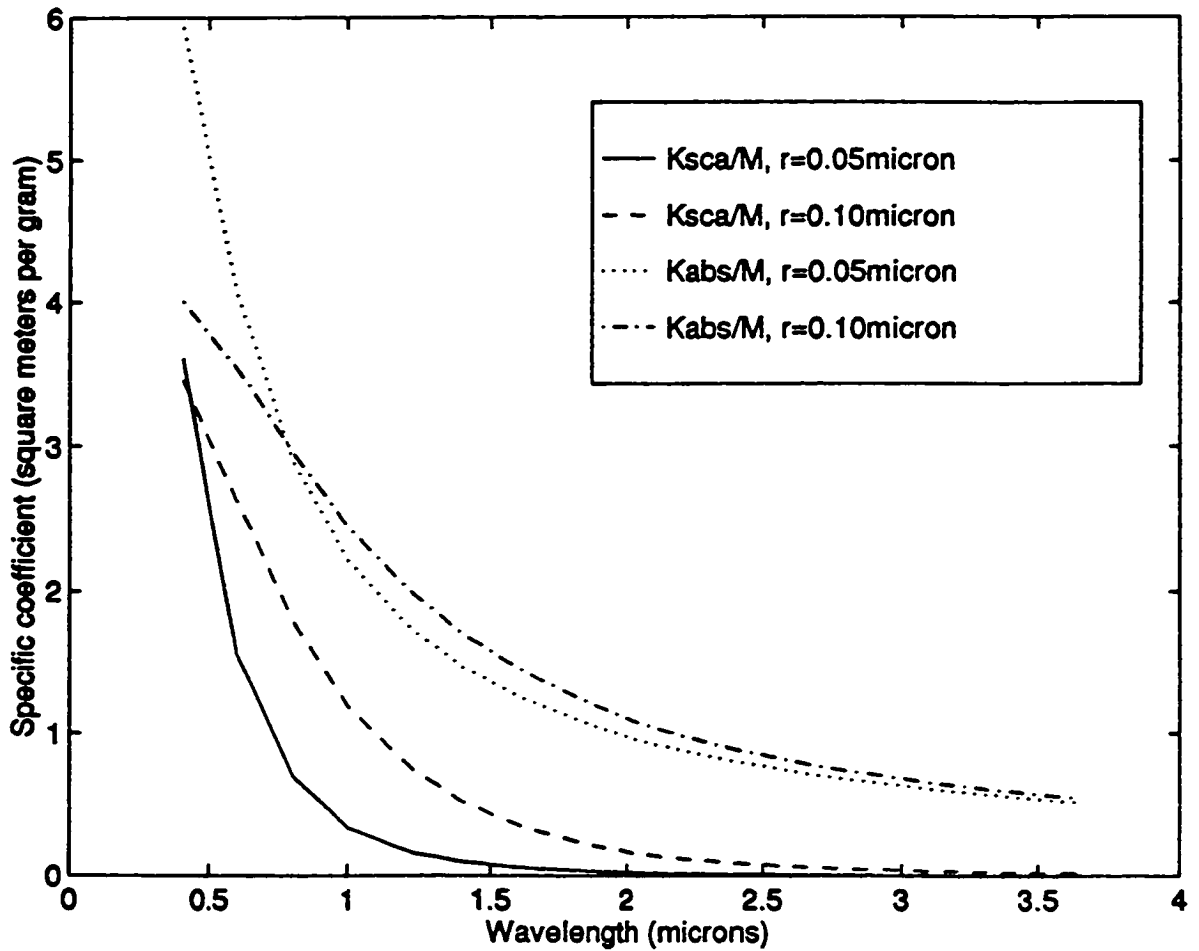Figure 4.7a Specific scattering coefficient ($\Psi_{sca} = K_{sca}/M$) and specific absorption coefficient ($\Psi_{abs} = K_{abs}/M$) of black carbon particles in the solar spectrum for two geometric mean radii and $\sigma=1.5$: Ψ_{sca} at $r_g=0.05\mu m$ (solid line); Ψ_{sca} at $r_g=0.10\mu m$ (dashed line); Ψ_{abs} at $r_g=0.05\mu m$ (dotted line); Ψ_{abs} at $r_g=0.10\mu m$ (dashdot line).
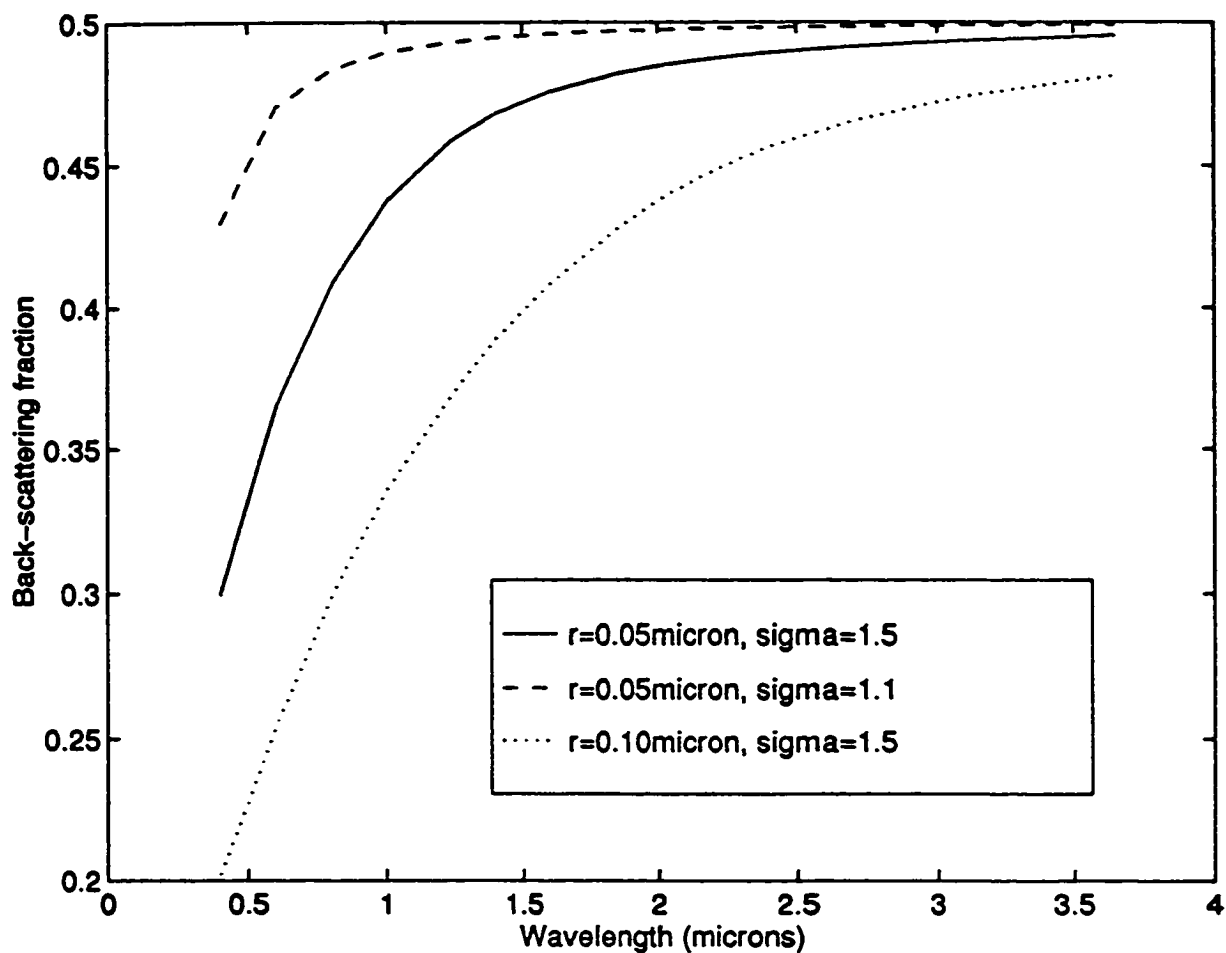
Figure 4.7b Backscattering fraction of black carbon particles in the solar spectrum for different size distributions: B at $r_g=0.05\mu m$ and $\sigma=1.5$ (solid line); B at $r_g=0.05$ and $\sigma=1.1$ (dashed line); B at $r_g=0.10\mu m$ and $\sigma=1.5$ (dotted line).

Figure 4.7a also shows Ψ_{abs} is generally higher than Ψ_{sca}, especially at longer wavelengths, which indicates that the absorption of the incident radiation by a layer of black carbon particles contributes more to the extinction than scattering. Consequently, the absorption optical depth is higher than scattering optical depth for a fixed aerosol loading; i.e., $\tau_{abs} > \tau_{sca}$. Figure 4.7b shows that the back-scattering fraction B has a very strong dependence on both size and wavelength. B increases with increasing wavelength for fixed-size particles, and decreases with increasing particle radius for certain wavelengths. The back scattering fraction approaches 0.5 for small particle in Rayleigh scattering region.

The calculated optical parameters for sulfate-black-carbon aerosols are listed in Table 4.3a - d. Table 4.3a shows the optical parameters of sulfate aerosols. Tables 4.3b - d shows the optical parameters for black carbon volume fractions of 1%, 5%, and 30% at mean radius of $0.10\mu m$ with $\sigma=1.5$.

The variation in the optical parameters of sulfate-black-carbon aerosols can be seen in Figure 4.8a - c, where the black carbon volume fraction f = 1 corresponds to a pure black carbon aerosol. It can be seen that the specific absorption coefficient is very sensitive to the black carbon fraction, it increases dramatically with increasing f, especially at lower fraction (see Figure 4.8a). For example, a black carbon fraction of 5% differs by five orders of magnitude from that of pure sulfate at visible wavelengths. Figure 4.8b shows that the dependence of specific scattering on the black

Table 4.3a Optical parameters of sulfate particles ($r_g = 0.10 \mu m$, f=0)

Band	Ψ_{ext} m²/kg	Ψ_{sca} m²/kg	Ψ_{abs} m²/kg	ω	G	B
1	4.863E+03	4.863E+03	5.810E-04	1.000E+00	7.048E-01	1.917E-01
2	2.133E+03	2.132E+03	3.340E-04	1.000E+00	6.084E-01	2.338E-01
3	1.017E+03	1.017E+03	1.079E-03	1.000E+00	4.993E-01	2.816E-01
4	5.217E+02	5.217E+02	8.640E-03	1.000E-01	3.964E-01	3.266E-01
5	2.636E+02	2.636E+02	4.942E-02	9.998E-01	2.997E-01	3.689E-01
6	1.650E+02	1.648E+02	2.742E-01	9.983E-01	2.384E-01	3.957E-01
7	1.007E+02	9.987E+01	8.680E-01	9.914E-01	1.852E-01	4.190E-01
8	5.895E+01	5.638E+01	2.568E+00	9.564E-01	1.395E-01	4.390E-01
9	4.294E+01	3.892E+01	4.014E+00	9.065E-01	1.167E-01	4.490E-01
10	3.164E+01	2.719E+01	4.454E+00	8.592E-01	9.884E-02	4.568E-01
11	2.459E+01	1.782E+01	6.766E+00	7.248E-01	8.273E-02	4.638E-01
12	9.938E+01	7.984E+00	9.140E+01	8.034E-02	6.397E-02	4.720E-01
13	2.187E+02	5.226E+00	2.135E+02	2.389E-02	4.881E-02	4.786E-01
14	2.274E+02	4.408E+00	2.230E+02	1.938E-02	3.669E-02	4.840E-01

Table 4.3b Optical parameters of sulfate-black-carbon particles(f=1%)

Band	Ψ_{ext} m²/kg	Ψ_{sca} m²/kg	Ψ_{abs} m²/kg	ω	G	B
1	4.985E+03	4.873E+03	1.118E+02	9.776E-01	7.045E-01	1.918E-01
2	2.202E+03	2.138E+03	6.398E+01	9.710E-01	6.087E-01	2.337E-01
3	1.063E+03	1.021E+03	4.236E+01	9.602E-01	4.997E-01	2.814E-01
4	5.563E+02	5.256E+02	3.072E+01	9.448E-01	3.967E-01	3.264E-01
5	2.919E+02	2.688E+02	2.316E+01	9.207E-01	3.005E-01	3.685E-01
6	1.862E+02	1.666E+02	1.958E+01	8.948E-01	2.389E-01	3.955E-01
7	1.187E+02	1.016E+02	1.712E+01	8.558E-01	1.857E-01	4.187E-01
8	7.343E+01	5.741E+01	1.603E+01	7.818E-01	1.398E-01	4.388E-01
9	5.575E+01	3.966E+01	1.609E+01	7.114E-01	1.169E-01	4.488E-01
10	4.300E+01	2.744E+01	1.556E+01	6.381E-01	9.897E-02	4.567E-01
11	3.485E+01	1.800E+01	1.685E+01	5.165E-01	8.283E-02	4.638E-01
12	7.123E+01	8.551E+00	6.268E+01	1.201E-01	6.429E-02	4.719E-01
13	2.402E+02	5.590E+00	2.346E+02	2.327E-02	4.898E-02	4.786E-01
14	2.357E+02	4.504E+00	2.312E+02	1.911E-02	3.673E-02	4.839E-01

Table 4.3c Optical parameters of sulfate-black-carbon particles (f=5%)

Band	Ψ_{ext} m²/kg	Ψ_{sca} m²/kg	Ψ_{abs} m²/kg	ω	G	B
1	5.214E+03	4.686E+03	5.278E+02	8.988E-01	7.081E-01	1.902E-01
2	2.460E+03	2.148E+03	3.120E+02	8.732E-01	6.100E-01	2.331E-01
3	1.258E+03	1.048E+03	2.094E+02	8.335E-01	5.008E-01	2.809E-01
4	6.996E+02	5.469E+02	1.527E+02	7.817E-01	3.983E-01	3.258E-01
5	3.978E+02	2.824E+02	1.153E+02	7.100E-01	3.026E-01	3.676E-01
6	2.734E+02	1.767E+02	9.666E+01	6.464E-01	2.414E-01	3.944E-01
7	1.896E+02	1.077E+02	8.195E+01	5.678E-01	1.876E-01	4.179E-01
8	1.314E+02	6.139E+01	7.002E+01	4.672E-01	1.412E-01	4.382E-01
9	1.069E+02	4.252E+01	6.436E+01	3.978E-01	1.180E-01	4.484E-01
10	8.876E+01	2.951E+01	5.925E+01	3.325E-01	9.985E-02	4.563E-01
11	7.579E+01	1.965E+01	5.614E+01	2.592E-01	8.360E-02	4.634E-01
12	1.044E+02	9.590E+00	9.478E+01	9.188E-02	6.486E-02	4.716E-01
13	2.608E+02	6.251E+00	2.545E+02	2.397E-02	4.935E-02	4.784E-01
14	2.510E+02	4.853E+00	2.462E+02	1.933E-02	3.696E-02	4.838E-01

Table 4 3d Optical parameters of sulfate-black-carbon particles (f=30%)

Band	Ψ_{ext} m²/kg	Ψ_{sca} m²/kg	Ψ_{abs} m²/kg	ω	G	B
1	6.2314E+03	3.927E+03	2.304E+03	6.302E-01	7.144E-01	1.875E-01
2	3.818E+03	2.220E+03	1.598E+03	5.815E-01	6.075E-01	2.342E-01
3	2.379E+03	1.222E+03	1.157E+03	5.139E-01	4.995E-01	2.815E-01
4	1.569E+03	6.929E+02	8.764E+02	4.415E-01	4.018E-01	3.242E-01
5	1.056E+03	3.800E+02	6.757E+02	3.599E-01	3.105E-01	3.642E-01
6	8.166E+02	2.468E+02	5.698E+02	3.022E-01	2.523E-01	3.896E-01
7	6.371E+02	1.553E+02	4.818E+02	2.437E-01	1.984E-01	4.132E-01
8	4.951E+02	9.129E+01	4.038E+02	1.844E-01	1.495E-01	4.346E-01
9	4.280E+02	6.463E+01	3.634E+02	1.510E-01	1.248E-01	4.454E-01
10	3.764E+02	4.616E+01	3.303E+02	1.226E-01	1.055E-01	4.539E-01
11	3.327E+02	3.181E+01	3.009E+02	9.561E-02	8.820E-02	4.614E-01
12	3.150E+02	1.780E+01	2.972E+02	5.652E-02	6.848E-02	4.700E-01
13	3.898E+02	1.135E+01	3.785E+02	2.911E-02	5.183E-02	4.773E-01
14	3.446E+02	7.397E+00	3.372E+02	2.146E-02	3.848E-02	4.832E-01

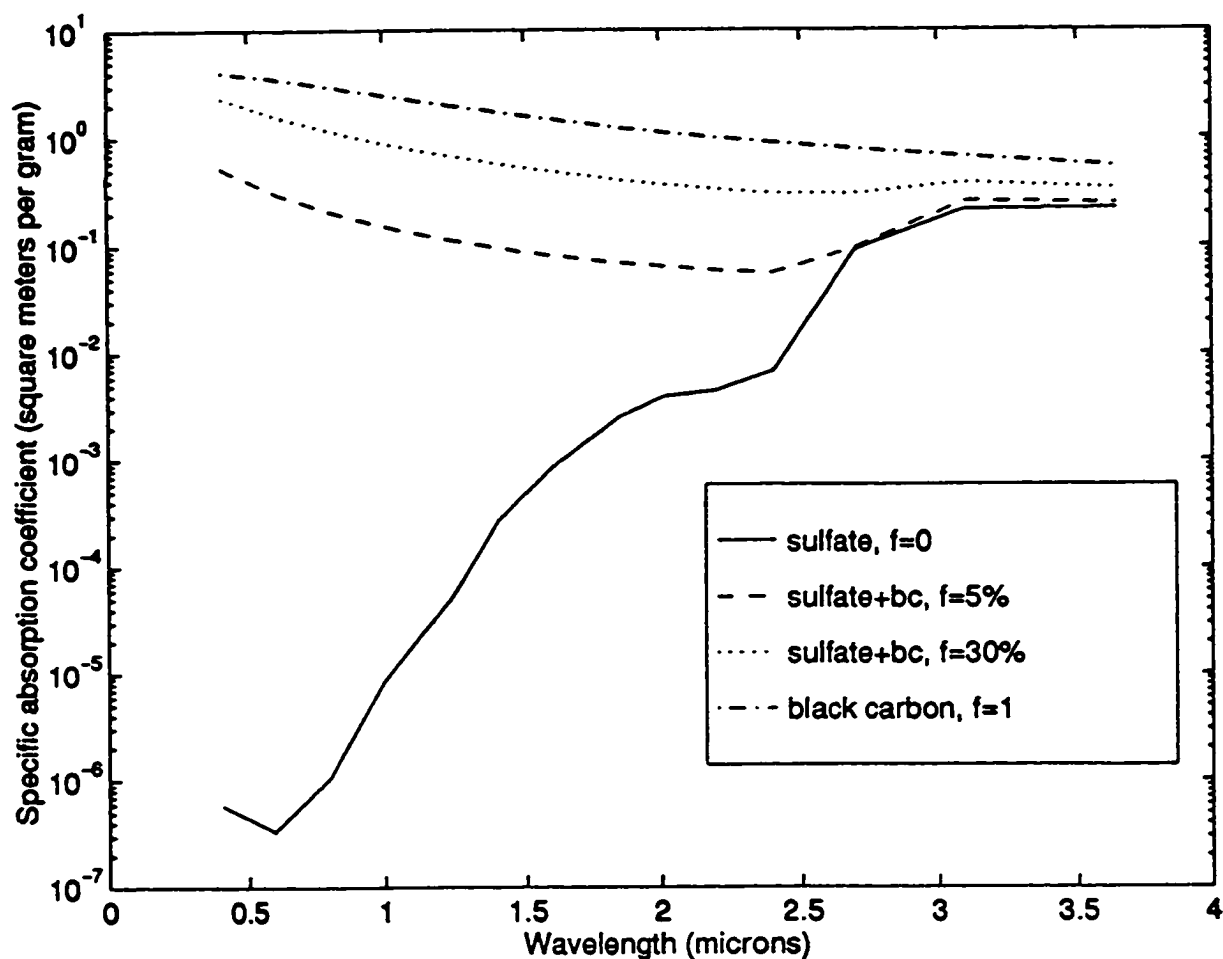Figure 4.8a Specific absorption coefficient (m²/g) of sulfate-black-carbon aerosols in the solar spectrum for different black carbon fractions: f=0, pure sulfate (solid line); f=5% (dashed line); f=30% (dotted line); and f=1, pure black carbon (dashdot line).at r_g=0.10μm and σ=1.5.
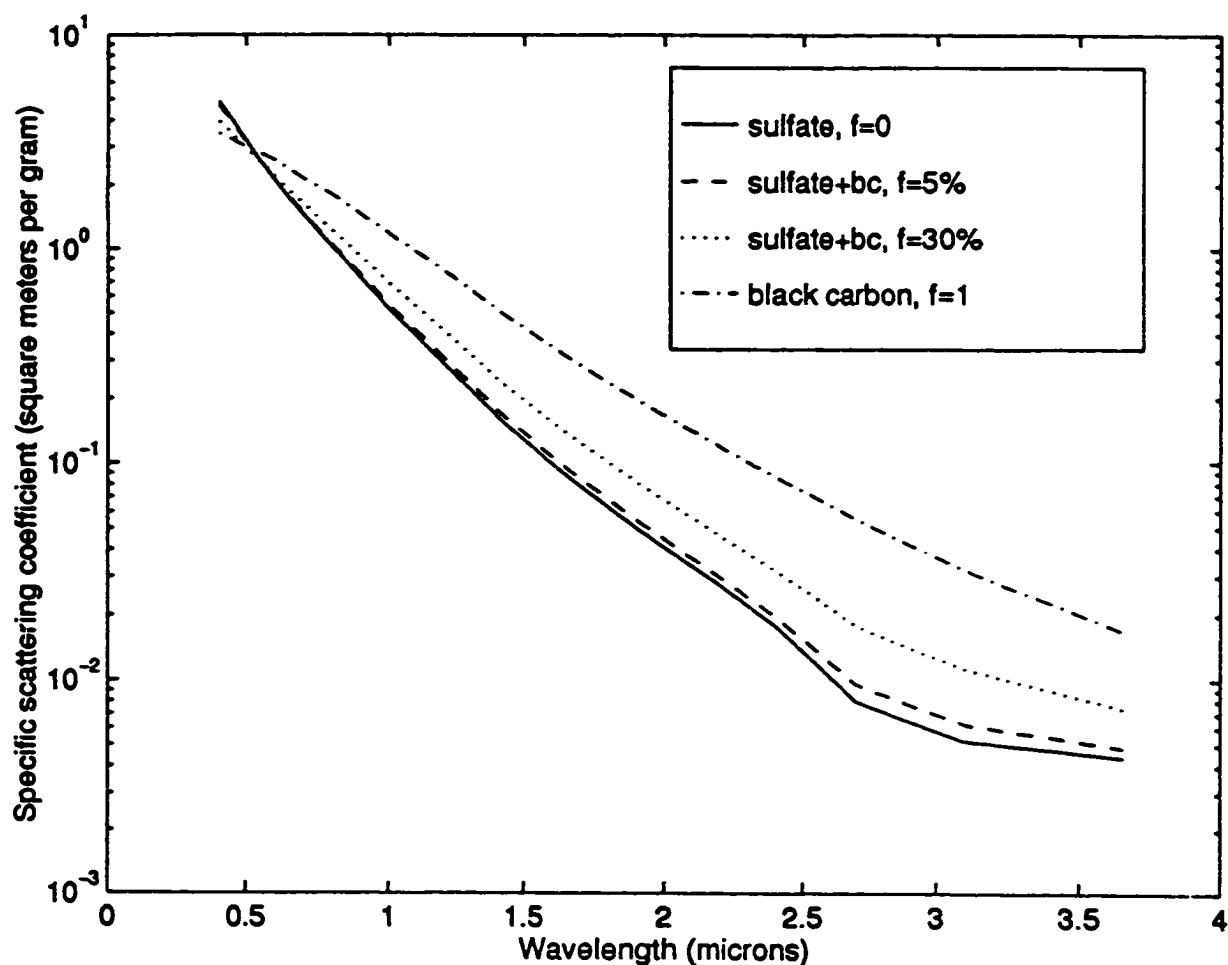
Figure 4.8b Specific scattering coefficient (m²/g) of sulfate-black-carbon aerosols in the solar spectrum for different black carbon fractions: f=0, pure sulfate (solid line); f=5% (dashed line); f=30% (dotted line); and f=1, pure black carbon (dashdot line) at r_g=0.10μm, σ=1.5.
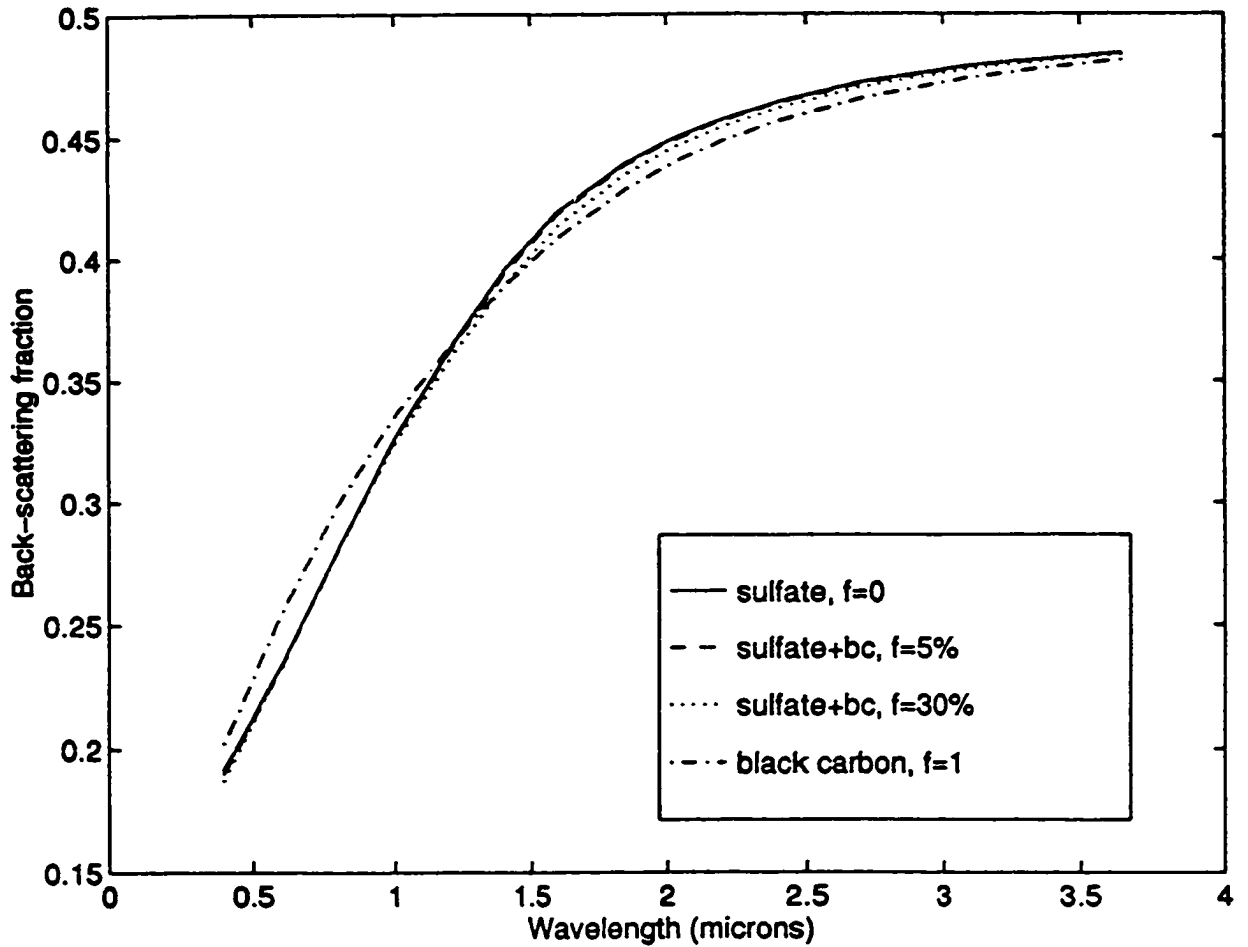
Figure 4.8c Backscattering fraction of sulfate-black-carbon aerosols in the solar spectrum for different black carbon fractions: f=0, pure sulfate (solid line); f=5% (dashed line); f=30% (dotted line); and f=0, pure black carbon (dashdot line) at r_g=0.10μm σ=1.5.

carbon volume fraction is relatively weak. As a result, the absorption optical depth responds significantly to an increase in the black carbon fraction in sulfate-black carbon aerosol, while the scattering optical depth does not. It can be seen in Figure 4.8c that the back-scattering fraction has only a small dependence on f , for both black carbon and sulfate aerosols. This infers that B is more sensitive to the size and wavelength than the refractive index.

4.3 Radiative Transfer Model

4.3.1 Radiative Transfer Equation

When an aerosol layer of optical thickness τ_a, is placed in an earth-atmosphere system with albedo R, the combined earth-atmosphere-aerosol system albedo R_a is affected by multiple reflections between the surface of the earth and the aerosol layer. The change in albedo ΔR is defined as

$$\Delta R = R_a - R ,$$ (4-10)

which can be obtained using the two-steam approximation to the radiative transfer equation (Chylek and Coakley, 1974). The radiative transfer equation in a plane-parallel atmosphere for solar wavelengths, is,

$$\mu \frac{dI(\mu, \tau)}{d\tau} = I(\mu, \tau) - \frac{\omega}{2} \int_{-1}^{1} p(\mu, \mu')I(\mu', \tau)d\mu' , \qquad (4\text{-}11)$$

where $I(\mu, \tau)$ is the intensity at optical depth τ and zenith angle $\Theta = \arccos(\mu)$, $p(\mu', \mu)$ is the scattering phase function, and ω is the single scattering albedo.

In the two-stream approximation, the intensity is assumed isotropic over the upper hemisphere ($\mu > 0$) with the value $I^+(\tau)$, and over the lower hemisphere ($\mu < 0$) with a corresponding value of $I^-(\tau)$. ie,

$\mu > 0$: $I(\mu, \tau) = I^+(\tau)$,

$\mu < 0$: $I(\mu, \tau) = I^-(\tau)$.

Consequently, the radiation transfer equation (4-11) can be changed into a set of two coupled first order differential equations with solutions $I^+(\tau)$ and $I^-(\tau)$:

$$\frac{1}{2} \frac{dI^+(\tau)}{d\tau} = I^+(\tau) - \omega B \, I^-(\tau) - \omega(1-B)I^+(\tau), \qquad (4\text{-}12)$$

$$-\frac{1}{2} \frac{dI^-(\tau)}{d\tau} = I^-(\tau) - \omega B \, I^+(\tau) - \omega(1-B)I^-(\tau), \qquad (4\text{-}13)$$

where B is the backscattering fraction of the aerosol layer. The original albedo R and the albedo for the combined system, R_a, can be expressed by $I^+(\tau)$ and $I^-(\tau)$:

$$R = \frac{I^+(\tau_a)}{I^-(\tau_a)} , \qquad (4\text{-}14)$$

$$R_a = \frac{I^+(0)}{I^-(0)} , \qquad (4\text{-}15)$$

where $\tau=0$ is at the top of the aerosol layer; and $\tau = \tau_a$ is at the bottom of the aerosol layer. The change in albedo is then given by (Chylek and Coakley, 1974):

$$\Delta R = R_a - R = \frac{[(1 - R_s)^2 \omega B - 2R_s(1- \omega)]2\tanh(\alpha\tau)}{[(1- \omega)+(1 - R_s)\omega B]2\tanh(\alpha\tau) + \alpha} \qquad (4\text{-}16)$$

where R_s is the surface albedo and

$$\alpha = 2\sqrt{(1- \omega)(1- \omega + 2\omega B)} \ . \qquad (4\text{-}17)$$

For an optically thin layer, $\tau_a \ll 1$, $\tanh(\alpha\tau_a) \to \alpha\tau_a$ (Chylek and Wong, 1995), ΔR becomes

$$\Delta R = 2\tau_a [(1 - R_s)^2 B \omega - 2R_s (1 - \omega)] \ . \qquad (4\text{-}18)$$

Finally, considering $\omega = \dfrac{\tau_{sca}}{\tau_{ext}}$, $1- \omega = \dfrac{\tau_{abs}}{\tau_{ext}}$, and $\tau_a = \tau_{ext}$, ΔR can be expressed as

$$\Delta R = 2(1 - R_s)^2 B \ \tau_{sca} - 4 \ R_s \ \tau_{abs} \ . \qquad (4\text{-}19)$$

4.3.2 Aerosol Radiative Forcing

The presence of a black carbon aerosol layer in the atmosphere will have an effect on the radiation budget of the earth- atmosphere system. This effect is generally quantified by the aerosol radiative

forcing ΔF. The aerosol radiative forcing is defined as the difference in outgoing shortwave flux at the top of the atmosphere (TOA) for an atmosphere with and without aerosol. i.e.,

$$\Delta F = F\uparrow^{SW}_{TOA}(background) - F\uparrow^{SW}_{TOA}(with\ aerosol) \qquad (4\text{-}20)$$

According to Charlson (1992), the global averaged direct radiative forcing due to an aerosol layer is

$$\Delta F = -\frac{S_0}{4} T_a^2(1-N_c)\ \Delta R, \qquad (4\text{-}21)$$

where S_0 is the solar constant, T_a is the transmittance of the atmosphere above the aerosol layer, N_c is the fraction of sky covered by clouds, and ΔR represents the albedo increase, $\Delta R = R_a - R$, due to the presence of the aerosol layer.

The sign of Equation 4-21 determines whether an aerosol layer will heat or cool the earth-atmosphere system. When $\Delta R > 0$, the albedo increases due to the additional aerosol layer, consequently, more radiation is reflected by the aerosol-surface system than the surface alone and the net radiative effect is cooling ($\Delta F < 0$). Whereas, when $\Delta R < 0$, less radiation is reflected, the aerosol layer leads to a heating effect ($\Delta F > 0$). It can be seen from Equation 4-18 that the sign of ΔR is determined by

$$\frac{(1 - R_s)^2}{2R_s} = \frac{(1 - \omega)}{\omega B} \qquad (4\text{-}22)$$

If the left side of Equation 4-22 is greater than right side, $\Delta R > 0$, otherwise, $\Delta R < 0$. The ratio of the fraction of radiation absorbed (1-ω), to the fraction of the radiation scattered back to the hemisphere (ωB) is the critical ratio (Chylek and Coakley, 1974). Equation 4-22 indicates that the surface albedo R_S plays a very important role in determining whether a cooling or heating effect is due to the aerosol layer. The same aerosol layers have different effects over surfaces with different surface albedos. The surface albedo determined by Equation 4-22 is defined as the critical surface albedo R_{SC}.

By substituting Equation (4-19) into (4-21), the direct radiative forcing can be expressed as

$$\Delta F_\lambda = -\frac{S_{o\lambda}}{4} T_{a\lambda}^2 (1 - N_c) [(1 - R_{s\lambda})^2 2B_\lambda \tau_{sca\lambda} - 4R_{s\lambda} \tau_{abs\lambda}]. \qquad (4\text{-}23)$$

The radiative forcing for each individual spectral band can be calculated by

$$\Delta F_i = \int \Delta F_\lambda \, d\lambda \approx \Delta F_{\lambda i} \Delta\lambda, \qquad (4\text{-}24)$$

where $\Delta F_{\lambda i}$ is the average forcing in the band (i), which is calculated using Equation 4-23 with the average values of parameters in the band and $\Delta\lambda$ is the bandwidth. The total aerosol forcing of the solar radiation (0.3 - 4.0μm) is the sum of the radiative forcing from all 14 bands:

$$\Delta F = \sum \Delta F_i \qquad i=1, 2...14. \qquad (4\text{-}25)$$

4.4 Radiative Effect of Black Carbon Aerosols

4.4.1 Radiative Forcing Calculation

The effect of a black carbon aerosol or a sulfate-black-carbon aerosol layer to solar radiation can be estimated theoretically using Equation (4-23). The calculations involve determining:

1) Environmental Parameters: $S_{o\lambda}$, N_c, $T_{a\lambda}$ and R_s:

The solar constant S_0 is defined as the flux of solar energy of all wavelengths received per unit time across a surface of unit area normal to the solar beam at the mean distance between the sun and the earth. The globally averaged incident solar flux at the top of the atmosphere is $S_0/4$. The solar spectrum, $S_{o\lambda}$, is the distribution of the solar energy flux at wavelength λ (Thekaekara, 1973). The incident solar irradiance contained in each band, S_{oi}, and the percentage, S_{oi}/S_o, are listed in Table 4.4. A value of $S_0 = 1368 W/m^2$ is used in this study (Winter, 1994).

Cloud cover N_c varies with latitude and the value ranges from 0.45 to 0.7 (Winter, 1994; Paltridge and Platt, 1976). A value of $N_c = 0.6$ (Charlson et al., 1992; Chylek et al, 1995) is taken for the following calculations.

The transmittance through the atmosphere, $T_{a\lambda}$, is a function of wavelength. The average value for each spectral band, T_{ai}, are taken from Winter (1994) and listed in Table 4.4. These were calculated using a model developed by Brine and Iqbal (1983), where the absorption of ozone, water vapour and mixed-gas of CO_2 and O_2 were considered. A solar zenith angle of 60°, which is often used as a representative average value over all zenith angles, was used in the model.

Table 4.4   Solar irradiance and atmospheric transmittance at each band in solar spectrum

Band	Range (μm)	S_{oi} (W/m^2)	S_{oi}/S_o	T_{ai}
1	0.3 - 0.5	295.37	21.39	0.69
2	0.5 - 0.7	332.17	24.28	0.89
3	0.7 - 0.9	225.52	16.49	0.93
4	0.9 - 1.1	151.44	11.07	0.83
5	1.1 - 1.35	98.73	7.22	0.89
6	1.35 - 1.45	53.06	3.88	0.22
7	1.45 - 1.75	74.37	5.44	0.91
8	1.75 - 1.95	29.02	2.12	0.20
9	1.95 - 2.1	15.24	1.11	0.72
10	2.1 - 2.3	16.03	1.17	0.95
11	2.3 - 2.5	12.54	0.92	0.49
12	2.5 - 2.9	17.69	1.29	0.02
13	2.9 - 3.3	10.79	0.79	0.26
14	3.3 - 4.0	9.38	0.68	0.83

The albedo R_s, is determined by the surface underlying the aerosol layer. A typical value $R_s = 0.15$ for land, $R_s = 0.06$ for the ocean surface, and $R_s = 0.10$ for the average, are used in the calculation. No wavelength dependence of R_s is considered in the present study.

2) Characteristic parameters of the aerosol layer: τ_{sca}, τ_{abs} and B

A refractive index of m = 1.75 -0.44i is used for black carbon aerosols in the calculation. The refractive index for sulfate and sulfate-black-carbon aerosol has been discussed in Section 4.2. The values listed in Table 4.1 are the arithmetically averaged results of all values contained in each individual band, which are then used as the representative values for the band.

The absorption, scattering cross section and asymmetry factor for each band, σ_{abs}, σ_{sca} and g, are obtained using Mie theory, where the average refractive index in each band are the input parameters. Assuming a log-normal size distributions, Ψ_{sca}, Ψ_{abs} and G are calculated by integration over the size distribution.

The optical depths τ_{sca}, τ_{abs} and back-scattering fraction B for each band are calcualated using Equation 4-7 and Equation 4-9. The aerosol loading L is determined for the specified case. For a black carbon aerosol layer, the mass density M is the measured black carbon concentration (see Chapter 3) in the air and ΔZ is the thickness of the aerosol layer.

3) Radiative forcing due to the aerosol layer

The radiative forcing for each band can be obtained from Equation 4-23. The total solar radiative forcing due to the presence of the aerosol layer is found from Equation 4-25.

4.4.2 Case Studies and Discussion

Equation 4-23 indicates that the radiative forcing by an aerosol layer is proportional to the aerosol loading. A higher forcing is expected for a higher aerosol loading case. Therefore the day of the forest fire is the case chosen to estimate the upper limit of the radiative effect over the study region.

1) Effect of Black Carbon Aerosols

Two aerosol samples have been collected on the forest fire day and the average black carbon concentration found is $M = 1.04 \mu g/m^3$. The thickness of the aerosol layer is about 1500m based on the vertical profile of the total aerosol number concentration on that day. Consequently, the black carbon aerosol loading is $L= 1.56 \times 10^{-6} kg/m^2$. The calculated radiative forcing from each band and the total forcing are listed in Table 4.5a. A total radiative forcing of $\Delta F= 0.09W/m^2$ is obtained, which means a heating effect is caused by the black carbon aerosols. The forcing from each individual band versus wavelengths
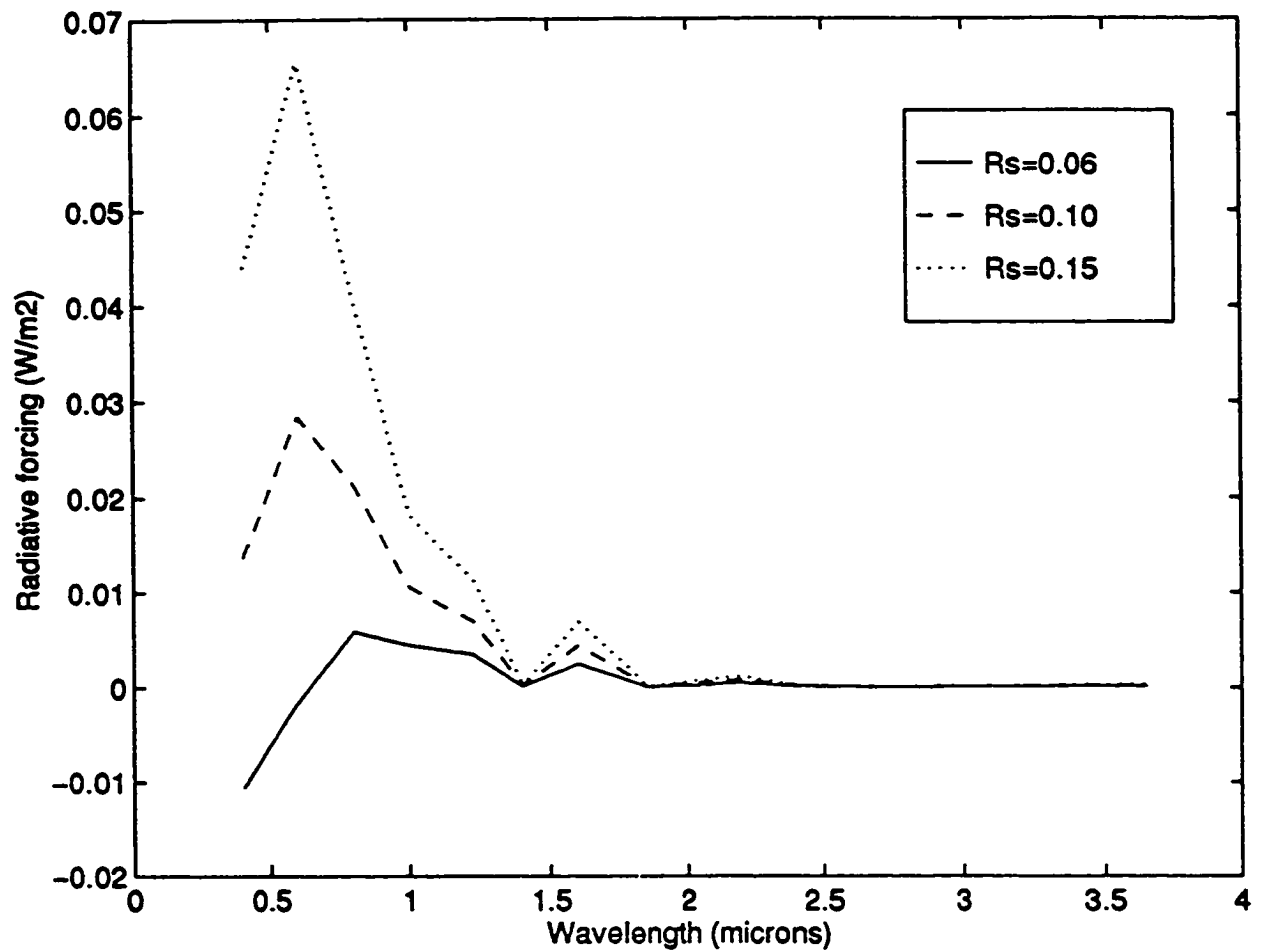
Figure 4.9 Radiative forcing (W/m²) of black carbon aerosols in the solar spectrum for different surface albedo: R_s=0.06 (solid line); R_s=0.10 (dashed line); and R_s=0.15 (dotted line) at r_g=0.05μm, σ=1.5 and L=1.56 x 10⁻⁶kg/m².
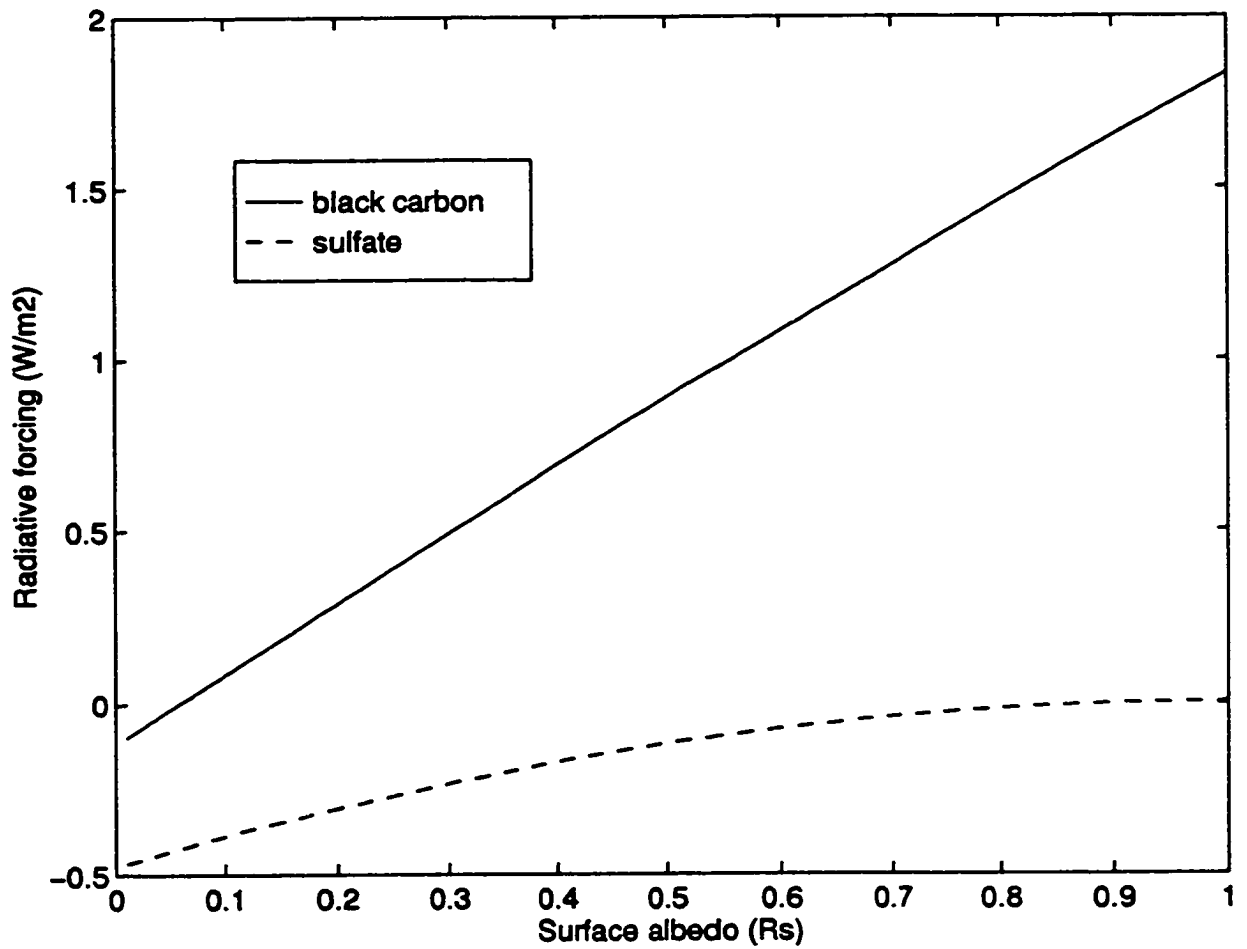
Figure 4.10   The relationship between the radiative forcing (W/m^2) and   the surface albedo R_s for black carbon and sulfate aerosols: black carbon aerosols (solid line, $L=1.56$ x $10^{-6}kg/m^2$); sulfate aerosols (dashed line, $L= 6.87x10^{-6}kg/m^2$).

Table 4.5b Radiative forcing of black carbon and sulfate aerosols at $R_S=0.06$, $R_S=0.15$ and $\sigma=1.5$.

	black carbon $r=0.05\mu m$	$L=1.56\times10^{-6}kg/m^2$	sulfate $r=0.1\mu m$	$L=6.87\times10^{-6}kg/m^2$
band	$\Delta F_i(W/m^2)$ $R_S=0.06$	$\Delta F_i(W/m^2)$ $R_S=0.15$	$\Delta F_i(W/m^2)$ $R_S=0.06$	$\Delta F_i(W/m^2)$ $R_S=0.15$
1	-1.07E-02	4.40E-02	-1.60E-01	-1.30E-01
2	-1.55E-03	6.56E-02	-1.58E-01	-1.29E-01
3	5.86E-03	4.06E-02	-6.79E-02	-5.55E-02
4	4.43E-03	1.82E-02	-2.16E-02	-1.76E-02
5	3.45E-03	1.13E-02	-9.15E-03	-7.48E-03
6	1.14E-04	3.40E-04	-2.11E-04	-1.72E-04
7	2.46E-03	6.92E-03	-3.13E-03	-2.55E-03
8	4.19E-05	1.13E-04	-3.47E-05	-2.76E-05
9	2.60E-04	6.88E-04	-1.61E-04	-1.23E-04
10	4.47E-04	1.17E-03	-2.08E-04	-1.52E-04
11	8.67E-05	2.25E-04	-2.72E-05	-1.65E-05
12	2.18E-07	5.58E-07	8.98E-08	2.90E-07
13	1.62E-05	4.13E-05	2.35E-05	6.24E-05
14	1.23E-04	3.11E-04	2.22E-04	5.84E-04
ΔF	5.07E-03	1.89E-01	-4.20E-01	-3.43E-01

is plotted in Figure 4.9. In addition to the case of $R_s = 0.10$ (average), the cases of $R_s = 0.6$ (ocean), and $R_s = 0.15$ (land) are also presented in Figure 4.9 and the results are listed in Table 4.5b. It can be seen that the radiative forcing caused by the black carbon aerosol layer is mainly due to the visible spectral regions since more solar radiation energy is stored in this region. The radiative effect due to the black carbon aerosol layer is almost zero for the longer wavelengths ($\lambda > 2\mu m$). Figure 4.9 also shows that the forcing is very sensitive to the value of surface albedo. The higher suface albedo enhances multiple reflectance which results in a high absorption by the aerosol layer. Therefor, the heating effect is more significant if the surface underlying the black carbon aerosol layer has higher albedo. Figure 4.10 shows the relationship between the surface albedo and the total radiative forcing of the black carbon aerosols.

2) Effect of Sulfate Aerosols

The radiative effects due to sulfate aerosols can be estimated using the same techniques used for black carbon aerosols. The measured average sulfate aerosol concentration is $2.29\mu g/m^3$ on the day of the forest fire, which is the dry sulfate mass. Considering the fact of sulfate aerosol growing by a factor of two (mass) under the usual humidity level (Wong et al., 1996), a sulfate aerosol loading $L = 6.87 \times 10^{-6} kg/m^2$ is used in the estimation. The calculated radiative forcing results are plotted in Figure 4.11 for $R_s = 0.06$, $R_s = 0.10$ and $R_s = 0.15$, and they are listed in Table 4.5b, except the result for $R_s = 0.10$ which is listed in Table 4.5a. A mean radius of $0.1\mu m$ and a
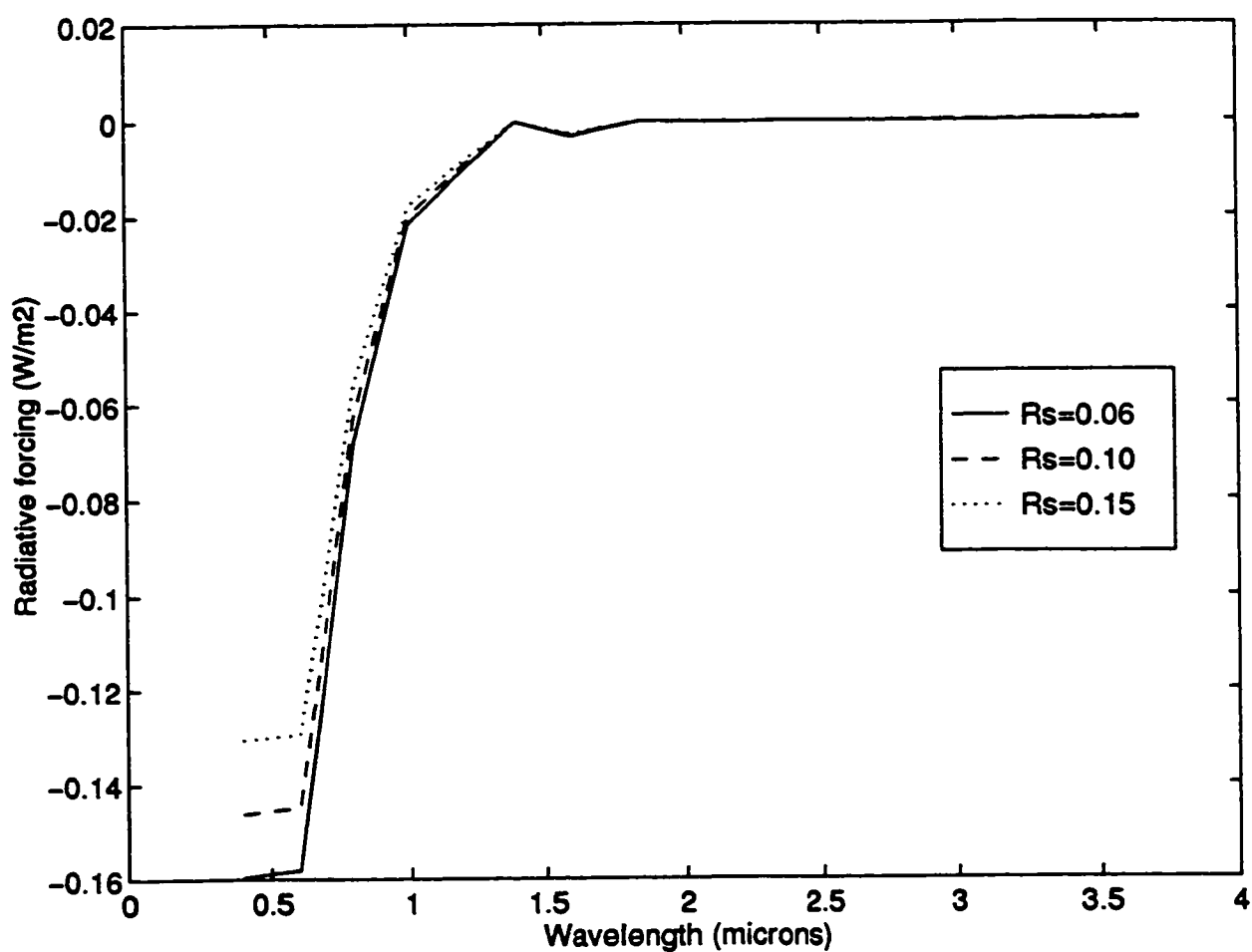
Figure 4.11   Radiative forcing (W/m²) of sulfate aerosols in the solar spectrum for different surface albedo: R_s=0.06 (solid line); R_s=0.10 (dashed line); and R_s=0.15 (dotted line) at r_g=0.10µm, σ=1.5 and L=6.87 x 10⁻⁶kg/m².

standard deviation of $\sigma = 1.5$ are used for the estimation. The total radiative forcing due to the sulfate aerosols is -0.39W/m^2 in the case of $R_s = 0.10$. As in the case of black carbon aerosols, Figure 4.11 shows the sulfate cooling effect is also mainly due to the visible spectral region. The total radiative forcing as a function of surface albedo is plotted in Figure 4.10. It can be seen that the lower values R_s cause a greater cooling effect, but the dependence on R_s is much smaller than in the case of black carbon aerosols.

3) Effect of Sulfate-Black Carbon Aerosols

Assuming the black carbon aerosols are internally mixed with the sulfate aerosols on the day of the forest fire, with average black carbon fraction of 20%, the radiative forcing of this sulfate-black-carbon aerosol can be calculated. The calculated results are listed in Table 4.5a, which shows the forcing is $\Delta F = -0.19$W/m^2 at $R_s = 0.10$. This is approximately a half reduction of the forcing caused by the pure sulfate aerosols (-0.39W/m^2). The other calculated results for black carbon fractions of 1%, 5%, 30% and 40% at Rs=0.10 are listed in Table 4.5c. These results indicate that the black carbon inclusions in sulfate aerosols significantly decrease the sulfate cooling effect and even change to a heating effect for high black carbon fraction aerosol loading. The radiative forcing in the solar spectrum for different black carbon fractions are plotted in Figure 4.12, where a pure sulfate aerosol (f = 0) is also plotted for comparison purpose. The dependence of forcing on the black carbon fraction is shown in Figure 4.13. For a small fraction of black carbon, the reduction of

Table 4.5c Radiative forcing of sulfate-black-carbon aerosols for different black carbon fractions at $R_s=0.10$, $r=0.1\mu m$, $\sigma=1.5$, and $L=8.43 \times 10^{-6} kg/m^2$.

| band	ΔF_i (W/m²) f=1%	ΔF_i (W/m²) f=5%	ΔF_i (W/m²) f=30%	ΔF_i (W/m²) f=40%
1	-1.75E-01	-1.47E-01	-3.22E-02	-5.58E-03
2	-1.73E-01	-1.51E-01	-4.48E-02	-1.45E-02
3	-7.39E-02	-6.48E-02	-1.56E-02	-5.65E-05
4	-2.34E-02	-2.00E-02	-1.18E-03	5.29E-03
5	-9.88E-03	-7.98E-03	3.01E-03	6.91E-03
6	-2.22E-04	-1.66E-04	1.62E-04	2.82E-04
7	-3.24E-03	-2.09E-03	4.63E-03	7.11E-03
8	-3.40E-05	-1.54E-05	9.62E-05	1.38E-04
9	-1.48E-04	-3.40E-05	6.52E-04	9.10E-04
10	-1.72E-04	2.31E-05	1.20E-03	1.65E-03
11	-1.74E-05	1.98E-05	2.48E-04	3.35E-04
12	1.34E-07	2.21E-07	7.60E-07	9.67E-07
13	5.51E-05	5.96E-05	8.77E-05	9.84E-05
14	4.88E-04	5.20E-04	7.09E-04	7.80E-04
ΔF	-4.58E-01	-3.92E-01	-8.30E-02	3.36E-03
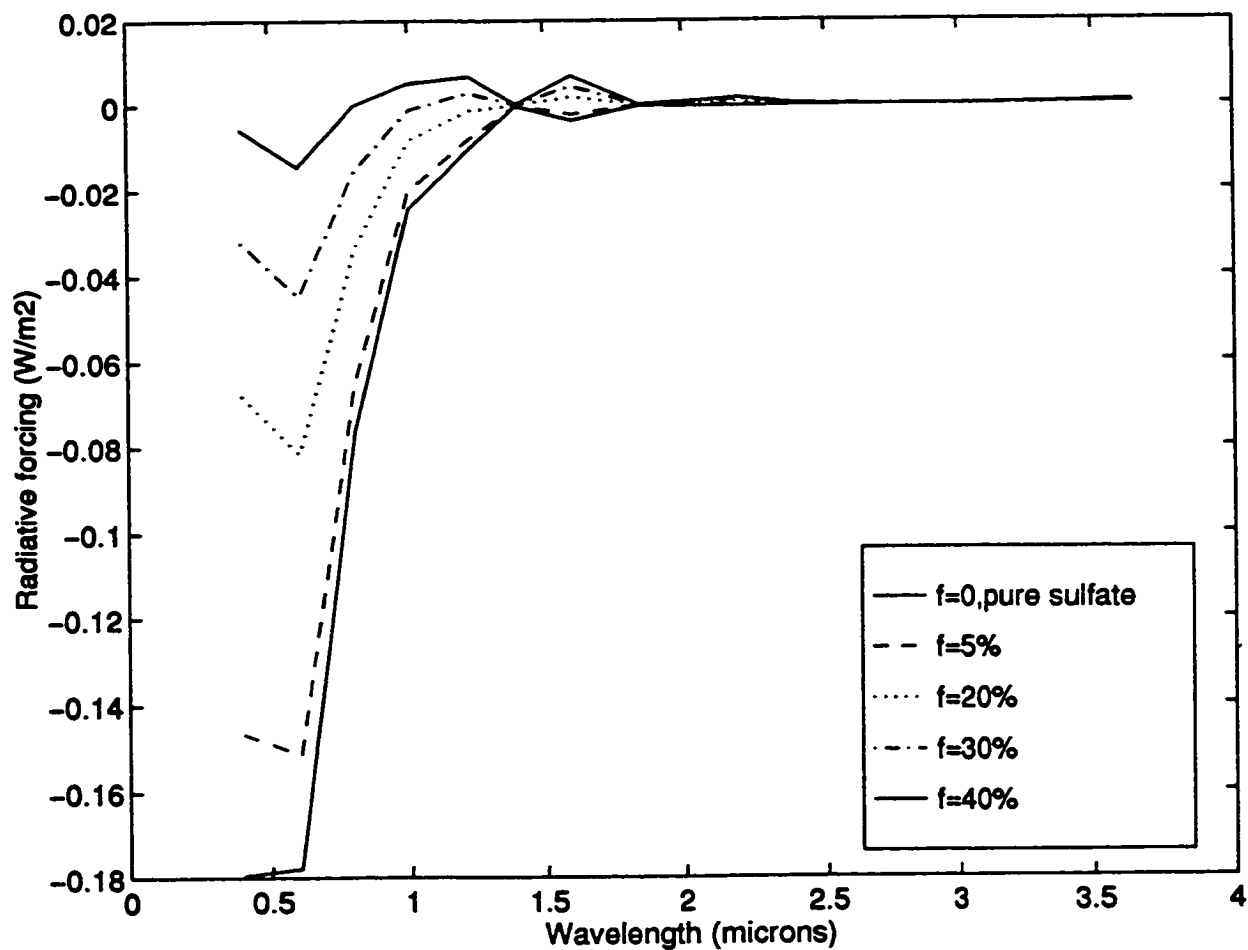
Figure 4.12 Radiative forcing (W/m²) of sulfate-black-carbon aerosols in the solar spectrum for different black carbon fractions: f=0, pure sulfate (lower solid line); f=5% (dashed line); f=20% (dotted line); f=30% (dashdot line); and f=40% (upper solid line) at r_g=0.10μm, σ=1.5, L=8.43 x 10⁻⁶kg/m², and Rs=0.10.
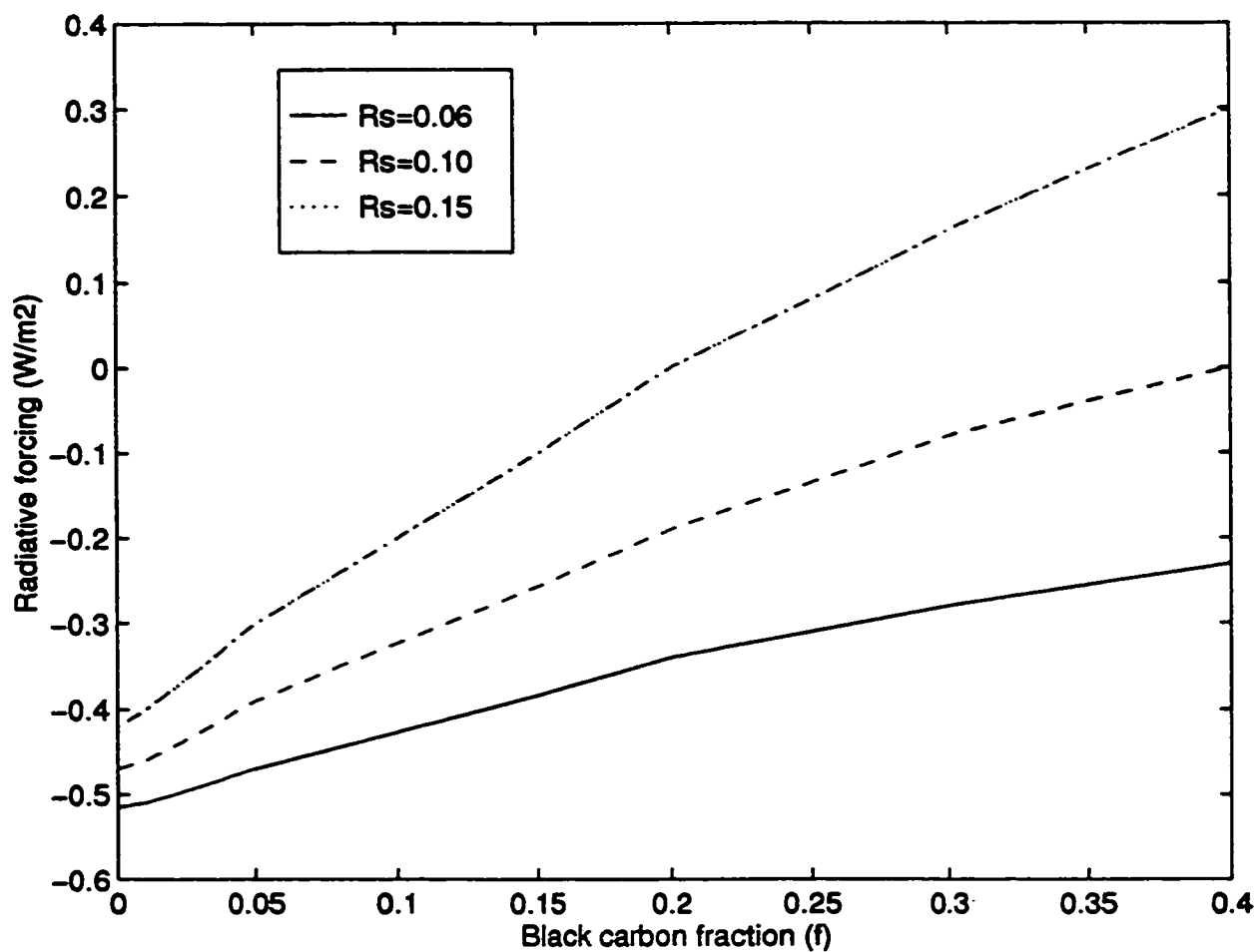
Figure 4.13 The relationship between the radiative forcing (W/m²) of sulfate-black-carbon aerosols and the black carbon volume fraction for three different values of surface albedo: Rs=0.06 (solid line); Rs=0.10 (dashed line); Rs=0.15 (dotted line) at L=8.43 x10⁻⁶ kg/m².

the sulfate cooling effect is approximately proportional to the volume fraction f, but the rate of the cooling effect reduction is reduced when f increases. Figure 4.13 shows that the radiative forcing of sulfate-black-carbon is also very sensitive to the surface albedo R_s. The calculated total radiative forcing at various black carbon fractions and surface albedos, and the critical surface albedo R_{sc}, are shown in Table 4.6. On the forest fire case ($R_s=0.10$; f=20%), R_{sc} is 0.15. This means for the region with surface albedo $R_s < 0.15$, this sulfate-black-carbon aerosol layer will cause a cooling effect. For the other region with $R_s > 0.15$, the same aerosol layer will cause a heating effect. For example, a heating effect ($\Delta F \geq 1.24 W/m^2$) will be lead by this sulfate-black-carbon aerosol layer if it is above a snow surface ($R_s \geq 0.5$).

Table 4.6 The total radiative forcing of sulfate-black-carbon aerosols for different black carbon fractions (f) and surface albedos at $r=0.1\mu m$, $\sigma=1.5$, and $L=8.43 \times 10^{-6} kg/m^2$.

f	ΔF_i (W/m²) $R_s=0.06$	ΔF_i (W/m²) $R_s=0.10$	ΔF_i (W/m²) $R_s=0.15$	ΔF_i (W/m²) $R_s=0.50$	R_{sc}
1%	-0.51	-0.46	-0.40	-0.06	0.60
5%	-0.47	-0.39	-0.30	0.24	0.34
20%	-0.34	-0.19	0.00	1.24	0.15
30%	-0.28	-0.08	0.16	1.80	0.12
40%	-0.23	0.00	0.30	2.29	0.10

Chapter 5

Radiative Effect: Black Carbon and Clouds

5.1 Optical Properties of Water-Black-Carbon Cloud

As mentioned in Section 2.2.2, black carbon particles by themselves are not very good CCN, but if they become coated with some soluble substance, the composite particles can be efficient CCN. Indeed black carbon has been found inside cloud droplets. The cloud water samples collected from Twin Otter during RACE show that the average black carbon content in cloud water over the Nova Scotia region is about 26 ± 3 μg, which corresponds to a black carbon mass fraction of 2.6×10^{-8} and volume fraction of 1.4×10^{-8}. The highest black carbon content found in cloud water during RACE is 220μg/kg (see Table 3.11), which yields a black carbon volume fraction of 1.2×10^{-7}. Using the black carbon concentration found in air for urban winter conditions, and considering that all the black carbon is incorporated inside a cloud, the upper limit of black carbon volume fraction over Nova Scotia is 10^{-6}.
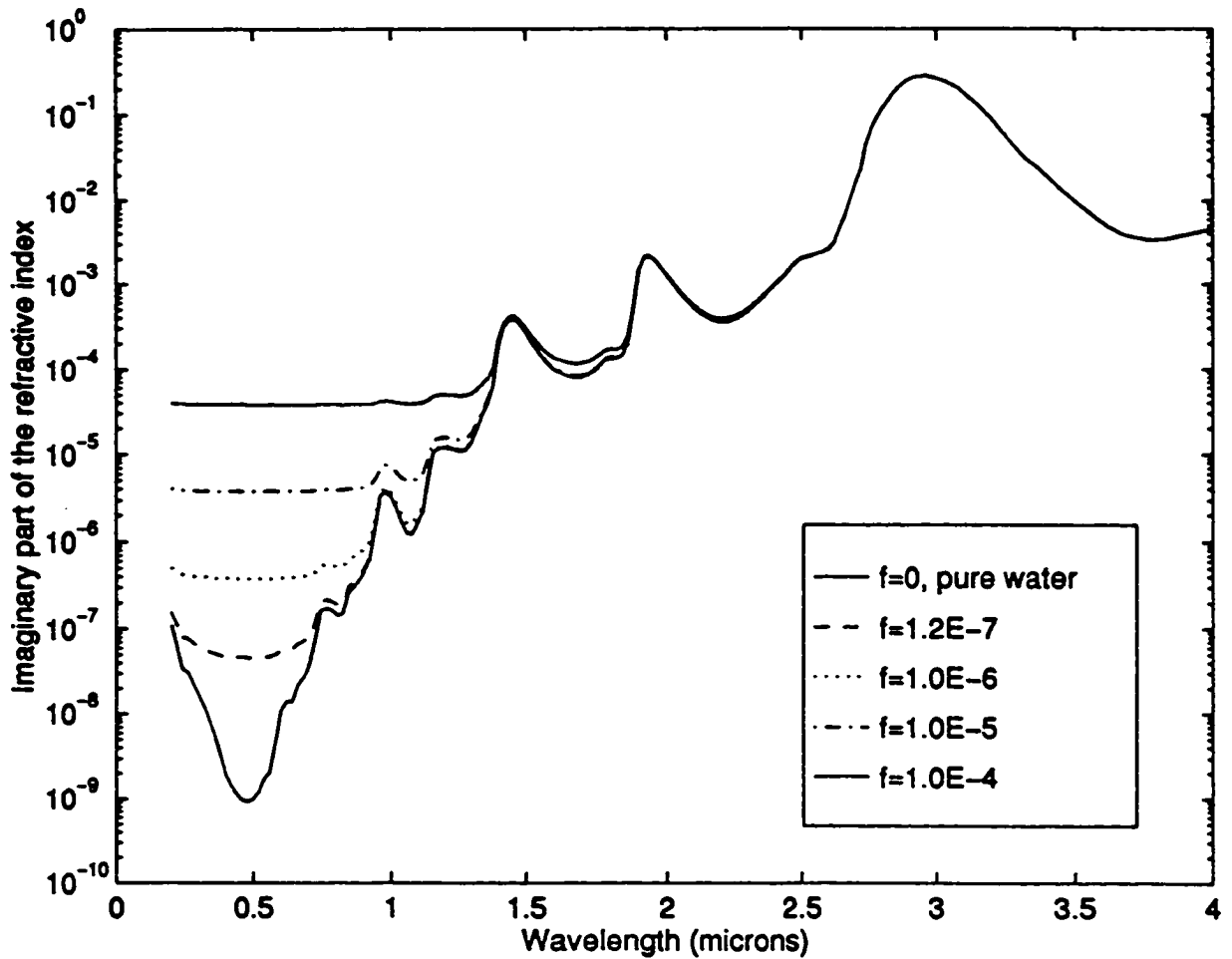
Figure 5.1 The imaginary refractive index of water-black-carbon drop as a function of wavelength for different black carbon volume fractions: f=0, pure water (lower solid line); f=1.2 x10⁻⁷ (dashed line); f= 1.0 x10⁻⁶ (dotted line); f=1.0 x10⁻⁵ (dashdot); f=1.0 x10⁻⁴ (upper solid line).

Assuming that the black carbon particles are dispersed randomly inside the water drops, the effective refractive index of this water-black-carbon drop can be calculated using Bruggeman formula (Equation 2-1). Figure 5.1 shows the imaginary part of the refractive index of such a water-black-carbon drop as a function of wavelength for different black carbon volume fractions. The refractive indices of water as a function of wavelengths in solar region is obtained from a compilation of available data (Hale and Querry,1984; Kou et al. 1993; Palmer and William, 1974; Downing and Williams, 1975). The refractive index of black carbon is taken to be $m=1.75-0.44i$. The black carbon fraction, 10^{-4}, is corresponding to the highest atmospheric black carbon concentration ($20\mu g/m^3$) reported in the literature.

It is noteworthy from Figure 5.1 that, across the visible spectrum, the imaginary refractive indices change drastically with black carbon fraction. For example, a black carbon fraction of 10^{-6} (0.0001%) will increase the imaginary refractive index by two orders of magnitude from the pure water drop. The largest change occurs around $\lambda= 0.5\mu m$. Figure 5.1 also shows that the different black carbon fraction curves converge to the values of pure water as the wavelength approaches the near-infrared regime. At longer wavelengths, even for $f=10^{-4}$, the effective imaginary refractive index exhibits no variation with pure water. This is because the imaginary refractive index of water itself begins to increases as wavelength approaches $1\mu m$. The real part of the effective refractive index differs very slightly from the real refractive index of pure

water within the black carbon fraction range of interest: $f=10^{-8}$ to $f=10^{-4}$.

5.2 Absorptance and Reflectance of Water-Black-Carbon Cloud

The presence of black carbon particles in a cloud alters the optical properties of the cloud droplets, consequently the absorptance and reflectance of clouds are expected to be affected. Calculations of absorptance and reflectance involve determining: a) the effective refractive index of water-black-carbon droplet for particular black carbon fraction; b) the single scattering albedo, asymmetry parameter and extinction coefficient; and c) the reflectance and absorptance.

To a good approximation, water droplets in clouds can be assumed to be spherical. Therefore, the single scattering properties of pure water and water-black-carbon droplets can be calculated using Mie program as described in Chapter 4. A log-normal size distibution is assumed for the calculation of the specific extinction coefficients, single scattering albedo, and asymmetry parameter. The effective radius, r_{eff}, which is defined as

$$r_{eff} = \frac{\int r^3 n(r) dr}{\int r^2 n(r) dr} \qquad (5\text{-}1)$$

is commonly used to characterize the size distribution of cloud droplets. Table 3.11 (see Chapter 3) shows that the effective radius of the cloud droplets ranges between $6\mu m$ and $14\mu m$. If $n(r)$ is a log-normal distribution, the effective radius and geometric mean radius, r_g, is related by

$$r_{eff} = r_g \exp\left(\frac{5\ln^2\sigma}{2}\right) \qquad (5\text{-}2)$$

The cloud droplets with three different effective radii are going to be discussed: a) $r_{eff}=8\mu m$, corresponding to $r_g=2.4\mu m$; b)$r_{eff}=6\mu m$, corresponding to $r_g=1.8\mu m$; c)$r_{eff}=12\mu m$, corresponding to $r_g=3.6\mu m$. The standard deviation, σ, is taken to be 2 in the calculation.

The absorptance, A, and reflectance, R, for a homogeneous cloud layer with an optical thickness τ, are defined as

$$A = \frac{F^{\downarrow}(0) - F^{\uparrow}(0) + F^{\uparrow}(\tau) - F^{\downarrow}(\tau)}{F^{\downarrow}(0)} \qquad (5\text{-}3)$$

$$R = \frac{F^{\uparrow}(0)}{F^{\downarrow}(0)} \qquad (5\text{-}4)$$

where $F^{\downarrow}$ is the downward flux and $F^{\uparrow}$ is the upward flux. The flux F is defined as the normal component of intensity integrated over the entire spherical solid angle and may be expressed as

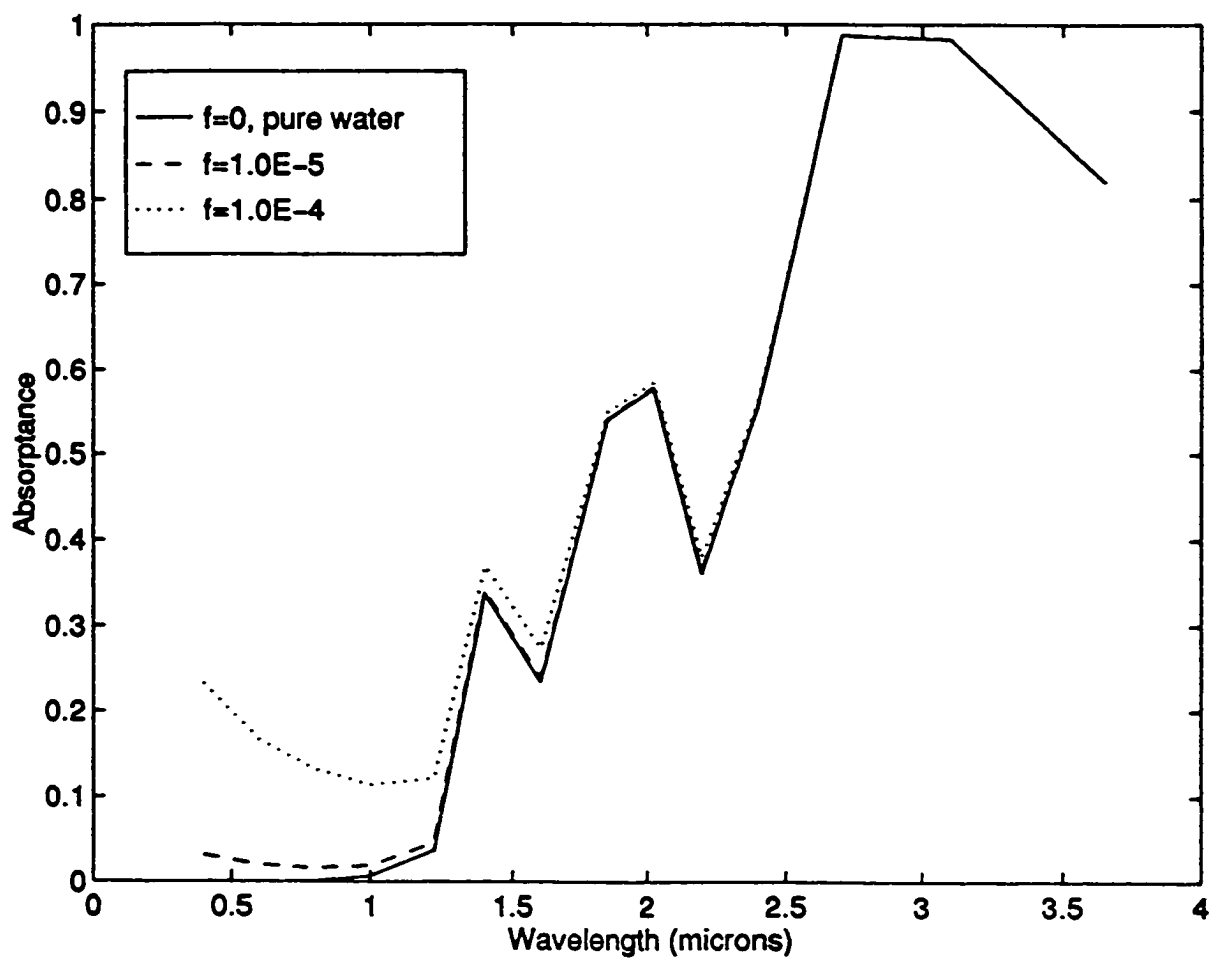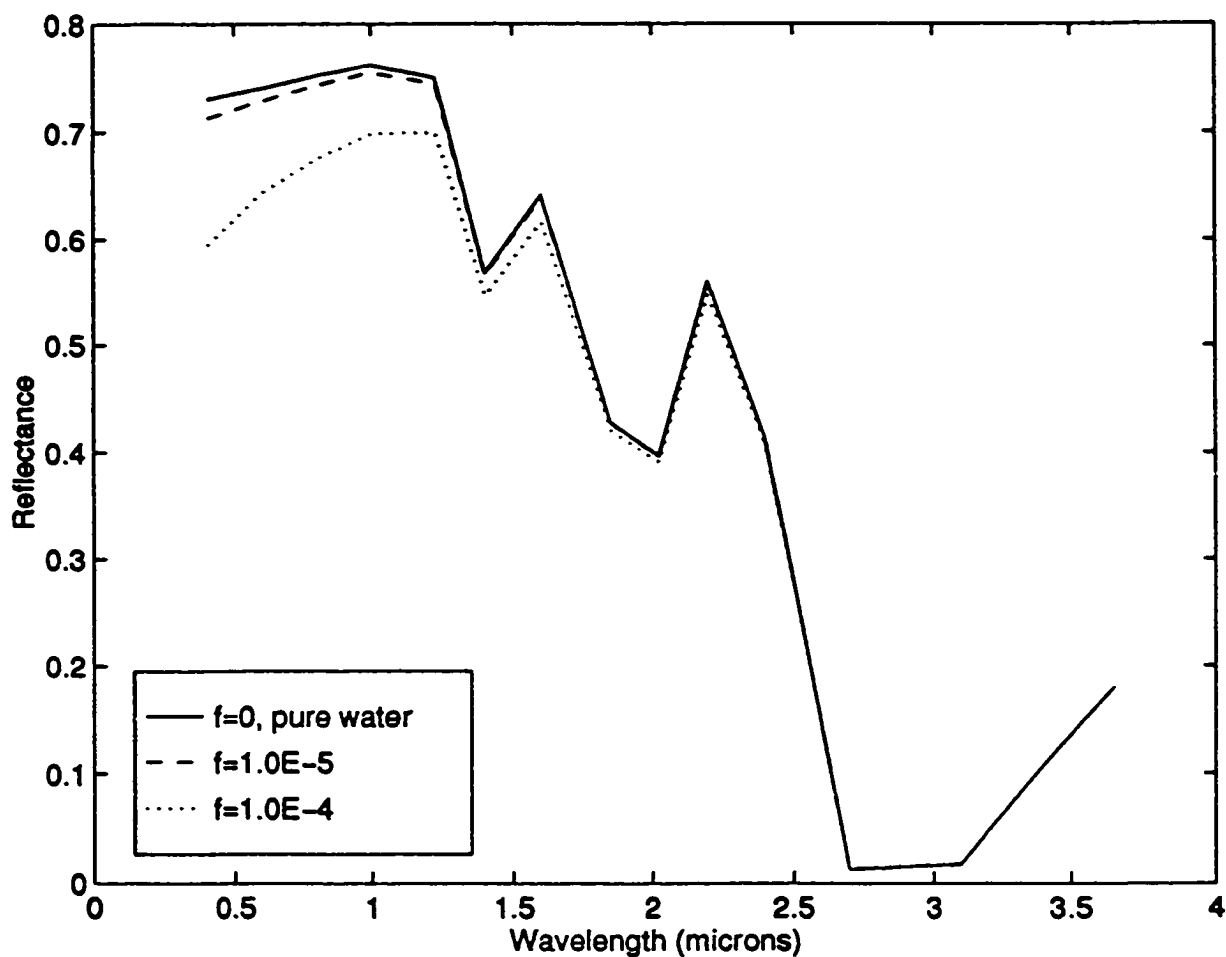$$F = \int_{4\pi} I\cos\theta d\Omega \qquad (5\text{-}5)$$

Figure 5.2a Absorptance of water-black-carbon cloud in the solar spectrum at different black carbon fractions: f=0, pure water (solid line); f=10^{-5} (dashed line); f=10^{-4} (dotted line) at Θ=60°, R$_s$=0, τ=20 and r$_{eff}$=8μm.
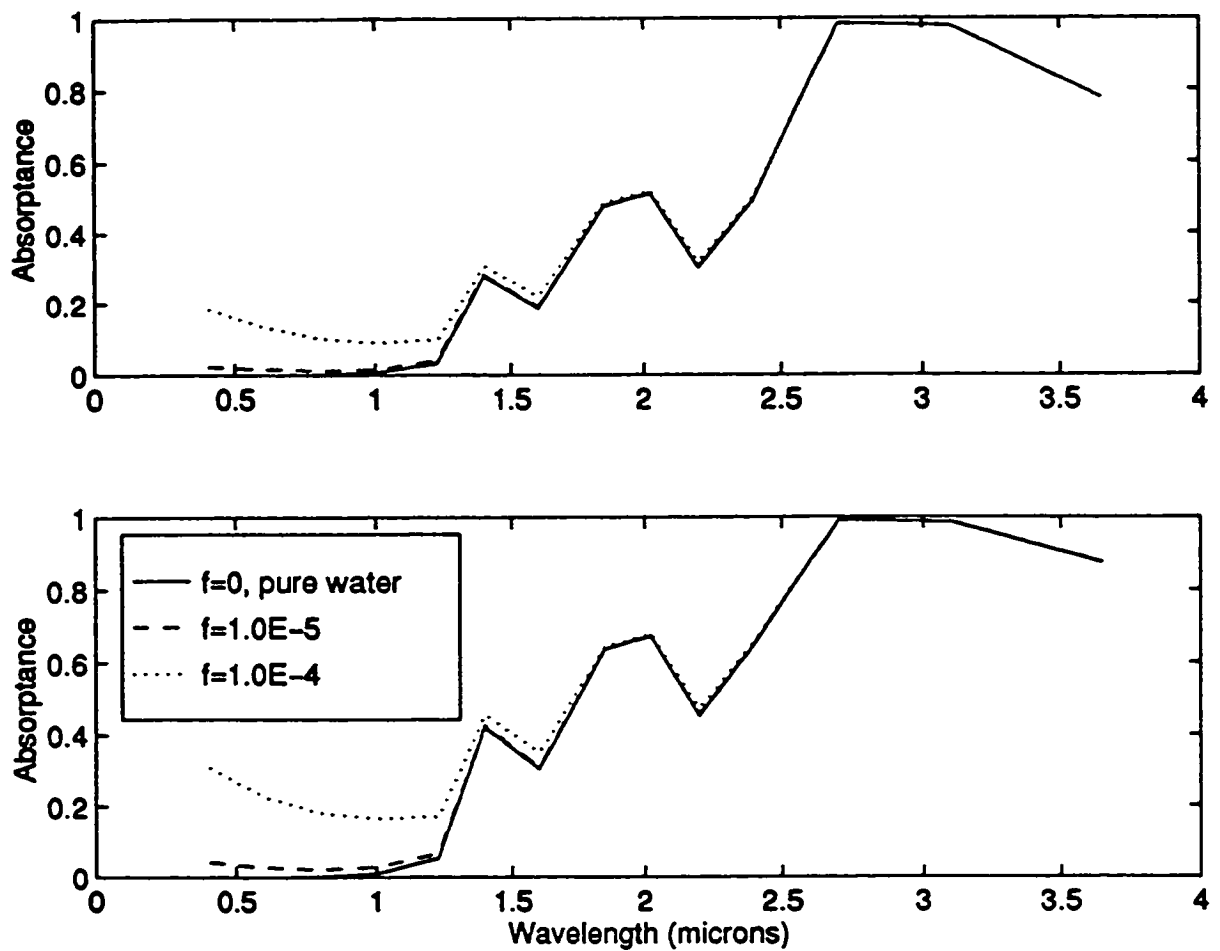
Figure 5.2b Reflectance of water-black-carbon cloud in the solar spectrum at different black carbon fractions: f=0, pure water (solid line); f=10^{-5} (dashed line); f=10^{-4} (dotted line) at Θ=60°, R$_s$=0, τ=20 and r$_{eff}$=8μm.

Figure 5.3a Absorptance of water-black-carbon cloud in the solar spectrum at different black carbon fractions: f=0, pure water (solid line); f=10⁻⁵ (dashed line); f=10⁻⁴ (dotted line) at $\Theta=60^\circ$, $R_s=0$, $\tau=20$. The upper one is for $r_{eff}=6\mu m$ and the lower one is for $r_{eff}=12\mu m$.
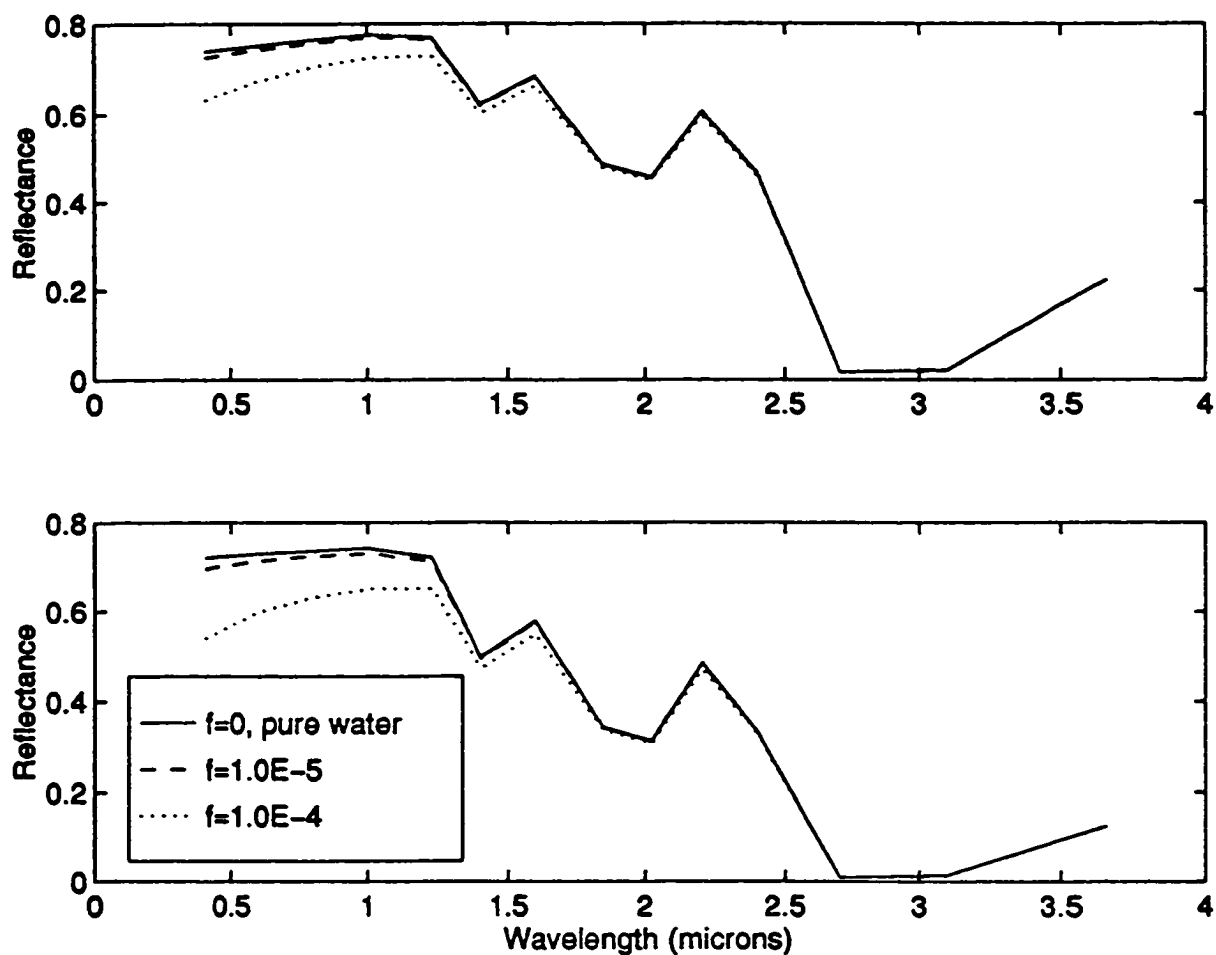
Figure 5.3b Reflectance   of water-black-carbon cloud in the solar spectrum at different black carbon fractions: f=0, pure water (solid line); f=10^{-5} (dashed line); f=10^{-4} (dotted line) at Θ=60°, R$_s$=0, τ=20 and the upper one is for r$_{eff}$=6μm and the lower one is for r$_{eff}$=12μm.

The intensity, I, can be solved using the appropriate approximation to the radiative transfer equation (4-11). As discussed in Chapter 4, the entire solar radiation spectrum ($0.2\mu m$ - $4\mu m$) is divided into 14 bands (see Table 4.1) to reduce the computational time.

Figure 5.2a and Figure 5.2b show the calculated reflectance and absorptance for each band at different black carbon fractions using Delta-Eddington approximation (Joseph et al., 1976; Meador and Weaver, 1980). A solar zenith angle of $\Theta=60^\circ$ and $R_s=0$, $\tau=20$, and $r=8\mu m$, are used in the calculation. It can be seen from Figure 5.2a and Figure 5.2b that the reflectance of the water-black-carbon cloud is lower than the pure water cloud because of the increasing of absorptance with increasing black carbon fraction. With high black carbon fraction, the differences between pure water cloud and "dirty" cloud is quite large. For example, with a black carbon fraction of 10^{-4}, the absorptance of the "dirty" cloud is increased to 22% while the pure water cloud is 8%, and the reflectance is decreased to 62% while the pure water cloud is 70%. However the black carbon impact on the cloud radiative properties is negligible over the Nova Scotia region even with the upper limit of black carbon fractions ($f=10^{-6}$).

Similar to the aerosol effect discussed in Chapter 4, the black carbon effect on the cloud radiative properties is mainly over the shorter wavelengths spectral region. There is basically no differences in the absorptance and reflectance between pure water cloud and "dirty" cloud when wavelength approaches $2\mu m$, even for the highest black carbon fraction 10^{-4}. Figure 5.3a and Figure 5.3b show the

comparison of the calculated absorptance and reflectance for two different effective radius of water-black-carbon clouds. The same solar zenith angle, optical depth and surface albedo as for r=8μm are applied. The total absorptance and reflectance in solar spectrum for different black carbon fractions are listed in Table 5.1. Both Table 5.1 and Figure 5.3a and Figure 5.3b show that the larger the water-black-carbon droplet, the larger the black carbon effect to the cloud for a particular black carbon fraction.

Table 5.1 The Absorptance and Reflectance of water-black-carbon cloud at $\Theta=60°$, $\tau=20$, and $R_s=0$.

Radius	$f=0$ pure water		$f=10^{-5}$		$f=10^{-4}$	
(r_{eff})	R	A	R	A	R	A
6μm	0.713	0.075	0.706	0.088	0.648	0.184
8μm	0.696	0.084	0.686	0.101	0.615	0.221
12μm	0.673	0.099	0.659	0.123	0.564	0.284

Chapter 6

Summary and Conclusions

Atmospheric black carbon concentrations have been measured in air, cloud, rain and snow samples collected over Nova Scotia during the summer of 1995 and the winter of 1996. A thermo-optical method has been employed to analyze the amount of black carbon. A summary of the black carbon concentration measurement results are listed in Table 6.1.

The amount of black carbon found in the atmosphere at 100m to 1700m altitude, collected by the Twin Otter varies from zero to $1.08\pm0.06\mu g/m^3$. The overall average is $0.13\pm0.02\mu g/m^3$. The highest black carbon concentration is found on the day of the forest fire. An average black carbon concentration of $0.22\pm0.02\mu g/m^3$ has been found in air near-the sea surface collected by the ferry Bluenose. In the Halifax urban area, the black carbon concentration ranges from 0.43 ± 0.02 to $3.1\pm0.2\mu g/m^3$ with an overall average of $0.89\pm0.06\mu g/m^3$. Air in winter has a much higher black carbon

Table 6.1 Summary of the black carbon measurements

Sample	BC conc. $\mu g/m^3$ or $\mu g/kg$	Scaveng -ing ratio	B.C. / Total aerosol	BC/SO$_4^{-2}$
air above ground (Twin Otter)	0.13 ± 0.01		2%	14%
air near- sea surface	0.22 ± 0.02			
air near-surface (urban summer)	0.54 ± 0.03		0.9± 0.2%	
air near-surface (urban winter)	1.69 ± 0.08		1.8± 0.3%	
cloud water	26 ± 3	50 - 1050		
rain (urban)	3.8 ± 0.3			
rain (rural)	2.7 ± 0.2			
snow (urban)	10.1 ± 0.5			
snow (rural)	1.7 ± 0.2			

concentration than in summer and it is probably due to residential heating. The average black carbon mass fraction in the aerosol is 0.9±0.2% in summer and 1.8±0.3% in winter. These results are within the range of the previous black carbon measurements in air over remote and urban areas (See Table 2.1). Using the typical value of black carbon concentration in air over Nova Scotia of $0.13\mu g/m^3$, and assuming the black carbon aerosols are uniformly distributed within a 1500m thick layer, then the total amount of black carbon in air is $1 \times 10^{11} g$. Taking 6 days as the black carbon resident time, the total black carbon released to atmosphere is estimated about $6 \times 10^{12} g$

per year. The result agrees with the estimation made by Crutzen and Andreae (1990).

With two exceptions, the mass fraction of black carbon found in the total aerosol fluctuates between 0.1% and 3% for Twin Otter air samples. The average black carbon: SO_4^{-2} mass ratio for air samples collected on the Twin Otter is about 14% when averaged over all the samples and 6% when averaged excluding the samples from the day of the forest fire. An extremely high fraction of black carbon: SO_4^{-2} of 85% was reached on the forest fire day.

The average value of black carbon in marine stratus clouds is about $26 \pm 3 \mu g/kg$ of cloud water, which is comparable to previous measurements (See Table 2.2b). An extremely high black carbon content obtained in a cloud-haze mixture sample on a polluted day is $220 \pm 10 \mu g/kg$. The measurements show that less than 6% of the black carbon fraction is within the internal mixture in clouds. Most (>90%) of the black carbon particles are outside cloud droplets, which indicates that black carbon is not effectively scavenged by clouds. A similar conclusion was obtained in NARE (Chylek et al., 1996) as well.

The amount of black carbon found in rain on average is about $3.8 \pm 0.3 \mu g/kg$ over the urban area and $2.7 \pm 0.2 \mu g/kg$ over the rural area, while the average black carbon concentration in snow is $10.1 \pm 0.5 \mu g/kg$ over the urban area and $1.7 \pm 0.2 \mu g/kg$ over the rural area. The black carbon concentration found in snow and rain are in the range of the previous measurements, however, it is at the lower

bound (See Table 2.2a). There is no obvious trend of black carbon concentration variation found during rainfall or snowfall. It is noteworthy that the black carbon content is much higher in the snow sample over the urban area than the snow over the rural area and the rain samples in both areas. Compared with cloud water samples, rain samples contain considerably lower black carbon concentrations.

The radiative effect of black carbon aerosol has been studied using a simple model. In general, the presence of a black carbon aerosol layer leads to a heating effect, which is mainly due to the visible wavelengths. The radiative forcing due to the black carbon aerosols is proportional to the black carbon loading. The estimated normalized forcing, defined as $\Delta G = \Delta F/L$, is about 55.8W/g, i.e., 55.8Watt radiative forcing per gram of black carbon loading. On the day of the forest fire, the black carbon loading was $L = 1.56 \times 10^{-3}$ g/m^2 and the radiative forcing was about 0.09W/m^2 (for $R_s = 0.10$). A conservative value of 0.44 for the imaginary refractive index, and 1.8g/cm^3 for the density have been chosen for black carbon aerosols in calculations. Had a higher imaginary refractive index or a lower density been chosen, the effect of black carbon would increase. For example, for an imaginary refractive index of 0.88, and density of 0.9g/cm^3, the black carbon radiative forcing will be increased by approximately a factor of 4. The black carbon aerosol radiative forcing depends on the surface albedo as well. The higher the surface albedo, the more significant the heating effect for the same aerosol layer.

Just as for most of the aerosols in the atmosphere, sulfate aerosols act to scatter solar radiation and have a cooling radiative effect. Unlike the black carbon aerosol case, the lower the surface albedo, the more significant the cooling effect, and the dependence on R_s is relatively low. The estimated sulfate radiative forcing was about -0.39W/m^2 on the forest fire day.

Comparing with the sulfate aerosol effect, the black carbon aerosol effect is significant. Assuming sulfate aerosols and black carbon aerosols are externally mixed in the aerosol layer, the total radiative forcing due to the mixed aerosol layer is $\Delta F = -0.30$W/m^2 for the forest fire case at $R_s = 0.10$, which is about 20% deduction of the sulfate cooling effect.

The radiative effect of an internally mixed sulfate and black carbon aerosol layer has been discussed as well. The presence of black carbon in sulfate aerosols alters the refractive index of the sulfate aerosols, and the resulting optical parameters, such as the specific absorption and single scattering albedo, especially in visible wavelengths. It is noted that the back-scattering fraction does not change much because it is more sensitive to the aerosol size and wavelength, than the refractive index. Overall, black carbon inclusions reduce the sulfate cooling effect. The reduction depends on both the aerosol loading and the surface albedo. For a small fraction of black carbon in sulfate, the reduction of the cooling effect is proportional to the black carbon fraction. For a particular aerosol

loading, there is a critical surface albedo, R_{sc}. When $R_s < R_{sc}$, there is a cooling effect; when $R_s > R_{sc}$, there is a heating effect. The estimated results show that on the day of the forest fire, the black carbon inclusions in sulfate aerosols reduce the radiative cooling from -0.39 to -0.19W/m². A heating effect could result instead of cooling if the aerosol layer is over a region with surface albedo greater than 0.15 (see Table 4.6).

In conclusion, it is very important to include the effect of black carbon aerosols on the radiative balance of earth-atmosphere system. Black carbon aerosols act to reduce the cooling effect of sulfate aerosols and for instances of high surface albedo or high black carbon loading it can sometimes result in a net heating.

The effect of black carbon on the radiative properties of clouds has been briefly studied as well. Across the visible spectrum, the optical properties of cloud drops change drastically with the fraction of black carbon. At longer wavelengths ($\lambda > 2\mu$m), pure water itself dominates the absorption of the incident radiation, thus the radiative effect of black carbon inclusion is almost negligible. Finally it is concluded that the effect of black carbon aerosols on the radiative properties of clouds is insignificant over the Nova Scotia region. However it might be significant in very polluted regions or biomass burning areas.
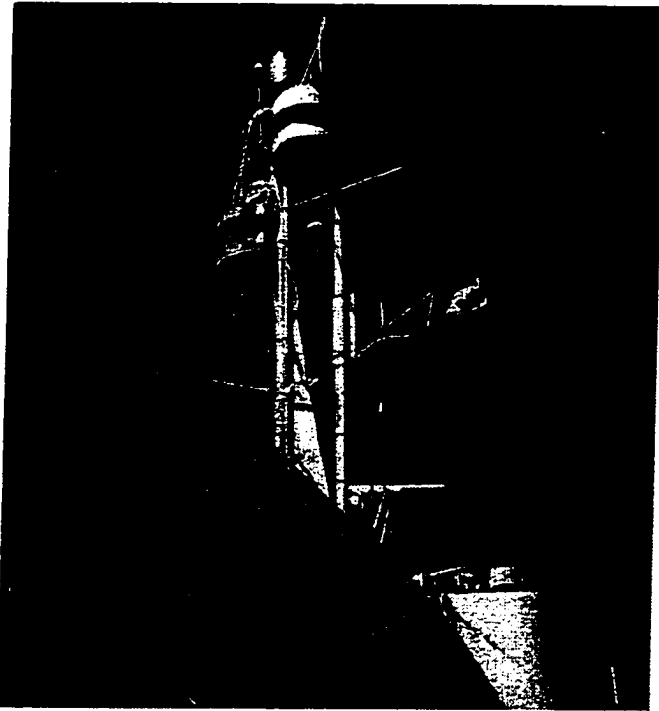
Appendix
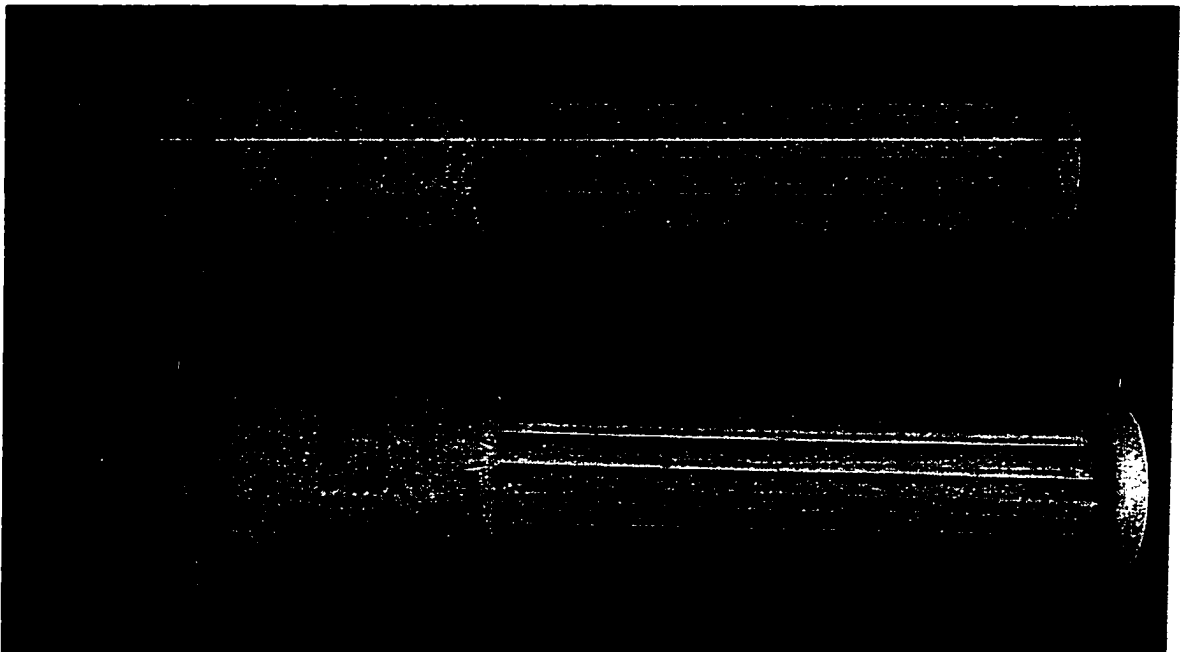
A: Twin Otter aircraft

B: Air sample holder housing on Twin Otter
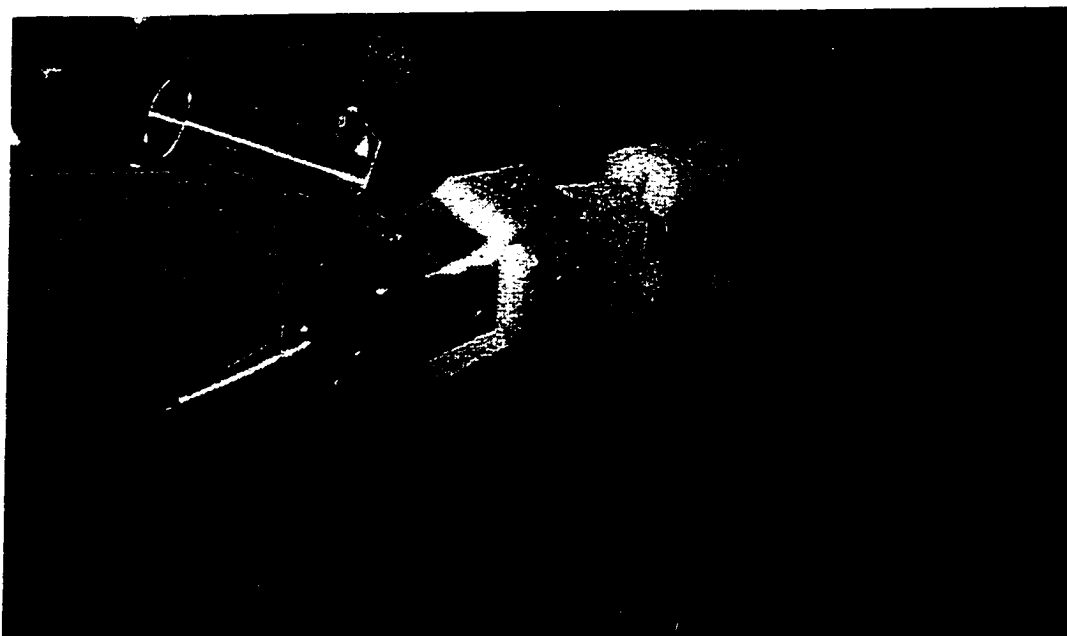
C: Air sampling inlet on Bluenose Ferry

D: Cloud water Collector

References

Ackerman, T. P., and O. B. Toon, Absorption of visible radiation in atmospheres containing mixtures of absorbing and nonabsorbing particles, Appl. Opt., 20, 3661-3668, 1981.

Adams, K. M. and L. I. Davis et al., Real-time, in situ measurements of atmospheric optical absorption in the visible via photoacoustic spectroscopy-ii. Validation for atmospheric elemental carbon aerosol, Atmospheric Environment, 23, 693-700,1989.

Benner, W. H., Brodznsky R. and Novakov T., Oxidation of SO_2 in droplets which contain soot perticles, Atmospheric Environment, 16, 1333-1339, 1982.

Bockhorn, H., F. Fetting, et al., Measurement of the soot concentration and soot particle sizes in propane oxygen flames, Eighteenth Symposium(International) on Combustion, The Combustion Institute, 1137-1146, 1981.

Bodhaine, B. A., and E. G. Dutton, et al. Surface aerosol measurements at Barrow during AGASP -2, J. Atmos. Chem., 9, 213-224, 1989.

Bohren, C. F., and D. R. Huffman, *Absorption and Scattering of Light by Small Particles*, John Wiley, New York, 1983.

Brine, D. and Iqbal, M., Diffuse and global spectral irradiance under cloudless skies. Solar Energy, 30(5):447-453, 1983.

Broecker, W. S., and T. H. Peng, Tracers in the sea, pp. 26-27, Lamont-Doherty Geol. Obs., Columbia Univ., New York, 1982.

Cachier, H., M. P. Bremond, and P. Buat-Menard, Determination of atmospheric soot carbon with a simple thermal method, Tellus, 41(B), 379-390, 1989.

Cadle, S. H., and J. M. Dasch, Wintertime concentrations and sinks of atmospheric particulate carbon at a rural location in northern Michigan, Atmos. Environ., 22, 1373-1381, 1988

Cass, G. R. and M. H. Conklin et al., Elemental carbon concentration: Estimation of a historical data base, Atmos. Environ., 18, 153-162, 1984.

Charalampopoulos, T. T., and J. D. Felske, Refractive indices of soot particles deduced from In-Situ laser light scattering measurements, Combust. Flame, 68, 283-293, 1987.

Charalampopoulos, T. T., H. Chang, and B. Stagg, The effects of temperature and composition on the complex referactive index of flame soot, Fuel, 68, 1173-1179,1989.

Charlson, R. J., S. E. Schwartz, J. M. Hales, R. D. Cess, J. A. Coakley, Jr., J. E. Hanson, D. J. Hofmann, Climate forcing by anthropogenic aerosols, Science, 255, 423-430, 1992.

Chippet, S., and W. A. Gray, The size and optical properties of soot particles, Combust. Flame 31, 149-159, 1978.

Chuan, R. L., and D. C. Woods, The appearance of carbon aerosol particles in the lower stratosphere, Geophys., Res. Lett., 11, 553-556, 1984.

Chylek, P. and J. A. Coakley, Aerosol and Climate, Science, 183, 75-77, 1974.

Chylek, P., V. Ramaswamy, and V. Srivastava, Albedo of soot-contaminated snow, J. Geophys. Res., 88, 10,837-10,843,1983.

Chylek, P., and V. Srivastava, et al., Aerosol and Graphite Carbon Content of snow, J. Geophys. Res. 92, 9801-9809, 1987.

Chylek, P., B. Johnson, and H. Wu, Black carbon Concentration in a Greenland Dye-3 ice core, Geophys. Res. Lett., 19, 1951-1953, 1992.

Chylek, P., B. Johnson, and P. A. Damiano, Biomass burning record and black carbon in GISP2 ice core, Geophys. Res. Lett., 22, 89-92, 1995a.

Chylek, P., G. Videen, D. Ngo, R. G. Pinnick, and J. D. Klett, Effect of black carbon on the optical properties and climate forcing of sulfate aerosols, J. Geophys. res., 100, 16,325-16,332,1995b.

Chylek, P., and J. Wong, Effect of absorbing aerosols on global radiation budget, Geophysical Research Letters, 22, 929-931, 1995.

Chylek, P., and P. A. Damiano, B. Johnson, D. Ngo, F. Said, B. Winter, C. M. Banic, W. R. Leatch, P. S. K. Liu and G. A. Isaac, Black carbon: Atmospheric concentration and cloud water content measurement over Southern Nova Scotia, J. Geophys. Res., accepted, 1996.

Chylek, P. Personal communication, 1996.

Clarke, A. D., Integrating sandwich: a new method of measurement of the light absorbtion coefficient for atmospheric particles, Appl. Opt., 21, 3011-3020, 1982.

Clarke, A. D. and K. J. Noone, Soot in the Arctic snowpack: A cause for perturbationa in radiative transfer, Atmos. Environ., 19, 2045-2053, 1985.

Clarke, A. D., K. J. Noone, J. Heintzenberg, S. G. Warren, and D. S. Covert, Aerosol light absorption measurement techniques: Analysis and intercomparisons, Atmospheric Environment, 21, 1455-1465, 1987.

Clarke, A. D., Aerosol light absorption by soot in remote environments, Aerosol Sci. Technol., 10, 161-171, 1989.

Coakley, J. A. Jr. and P. Chylek, The two-stream approximation in radiative transfer: including the angle of the incident radiation, J. Atmos. Sci. 32, 409-418, 1975.

Countess R. J., G. T. Wolff, and S. H. Cadle, The Denver winter aerosol: a comprehensive chemical characterization, J. Air Pollut. Control Ass. 11, 1194-1200, 1980.

Crutzen, P. J., and M. O. Andreae, Biomass burning in the tropics: Impact on atmospheric chemistry and biochemical cycles, Science, 250, 1669-1678, 1990.

d'Alessio, A., et al., Sixteenth Symposium (International) on Combustion, The Combustion Institute, 695-, 1977.

d'Almeida, G.A., P. Koepke and E. P. Shettle, *Atmospheric aerosols Global Climatology and Radiative Characteristics*, Deepak, Hampton, Va., 1991.

Dalzell, W. H., and A. F. Sarofim, Optical constants of soot and their application to heat-flux calculations, J. Heat Transfer, 91, 100-104, 1969

Dasch, J. M. and S. H. Cadle, Atmospheric carbon particles in the Detroit urban area: Wintertime sources and sinks, Aerosol Sci. Technol., 16, 236-248, 1989.

Downing, H. D., and D. Williams, Optical constants of water in the infrared, J. Geophys. Res. 80, 1656-1161, 1975.

Foster, P. J. and C. R. Howarth, Optical constants of carbons and coals in the infrared, 6, 719-729, 1967.

Gaffney J. S., R. L. Tanner, and M. Phillips, Seperating carbonaceous aerosol source terms using thermal evolution, carbon isotopic measurements, and C/N/S determinations, Sci. Total Environ. 36, 53-60, 1984.

Grenfell, T. C., D. K. Perovich, and J. A. Ogren, Spectral albedos of an alpine snowpack, Cold Reg. Sci. Technol., 4, 121-127, 1981.

Gundel, L. A., R. L. Dod, H. Rosen and T. Novakov, The relationship between optical attenuation and black carbon concentration for ambient and source particles, Sci/ Tot. Environ., 36, 197-202, 1984.

Hale, G., and M. Querry, Optical constants of water in the 200nm to 200μm wavelength region, Applied Optics, 23, 1206-1225,1984.

Hansen, J. E., A. A. Lacis, P. Lee, and W. C. Wang, Climatic effects of atmospheric aerosols, Ann. New York Acad. Scien., 575-587, 1980.

Hansen A. D. A., H. Rosen, and T. Novakov, Real time measurement of the absorption coefficient of aerosol particles. Appl. Opt. 21, 3060-3062, 1982.

Hansen A. D. A., H. Rosen, and T. Novakov, The aethalometer-an instrument for the real-time measurement of optical absorption by aerosol particles. Sci. total Envir. 36, 191-196, 1984.

Hansen, A. D. A., and B. A. Bodhaine et al., Aerosol black carbon measurement at the South Pole, Geophys. Res. Lett., 15, 1193-1196, 1988.

Hansen, A. D. A., V. N. Kapustin, V. M. Kopeikin, D. A. Gillette and B. A. Bodhaine, Optical absorption by aerosol black carbon and dust in desert region of central Asia, Atmos. Environ., 27A, 2527-2531, 1993.

Hallberg, A., et al., Phase partitioning for different aerosol species in fog, Tellus Ser. B, 44, 545-555, 1992.

Heintzenberg, J., Size-segregated measurement of particulate elemental carbon and aerosol light absorption at remote arctic locations, Atmos. Environ., 16, 2461-2469, 1982.

Heintzenberg. J. and P. Winkler, Elemental carbon in the urban aerosol:results of a seventeen months study in Hamburg, FGR, Sci. Total Environ. 36, 27-38, 1984a.

Heintzenberg. J. and D. S. Covert, Size distribution of elememtal carbon, sulphur and total mass in the radius range 10^{-6} to10^{-4}cm, The Science of the Total Environment, 36, 289-297, 1984b.

Heintzenberg. J. and A. Meszaros, Elemental carbon, sulfur and metals in aerosol samples at a Hungarian region air pollution station, Idojaras, 89, 313-319, 1985

Heintzenberg, J., A processor-controlled multi-sample soot photometer, Aerosol Sci. Technol., 8, 227-233, 1988.

Heintzenberg J. and P. Winkler, Elemental carbon in the atmosphere: Challenges for the trace analyst, Fresenius J. Anal. Chem. 340, 540-543, 1991.

Hopper, J. F., D. E. J. Worthy, L. A. Barrie and N. B. A. Trivett, Atmospheric observations of aerosol black carbon, carbon dioxide, and methane in the high arctic, Atmospheric Environment, 28, 3047-3054, 1994.

Huntzicker, J. J., and E. K. Heyerdahl et al., Combustion as the principal source of carbonaceous aerosol in the Ohio River Valley, JAPCA, 36, 705-709, 1986

Johnson, B., L. Kou, P. Chylek et al., An improved method for measuring black carbon, to be submitted, 1996

Joseph, J. H., W. J. Wiscombe and J. A. Weinman, The delta-Eddington approximation for radiative flux transfer, J. Atmos. Sci. 33, 2452-2459, 1976.

Keeler, G. J. , Japar S.M., Barchaczek R.A. et al. The source of aerosol elemental carbon at Allegheny mountain, Atmospheric Environment 24A, 2795-2805, 1990

Kou, L., D. Labrie, and P. Chylek, Refractive indices of water and ice in the 0.65 - to 2.5-μm spectral range, Applied Optics, 32, 3531-3540, 1992.

Larson, S. M., G. R. Cass, and H. A. Gray, Atmospheric carbon particles and the Los Angeles visibility problem, Aerosol Sci. Technol., 10, 118-130, 1989.

Leaitch, W. R., G. A. Isaac, J. W. Strapp, C. M. Banic and H. A. Wiebe, The relationship between cloud droplet number concentrations and anthropogenic pollution: observations and climatic implications, J. Geophys. Res., 97, 2463-2447, 1992.

Leaitch, W. R., C. M. Banic, G. A. Isaac, M. D. Couture, P. S. K. Liu, I. Gultepe , and S. M. Li, Physical and chemical observations in marine stratus during the 1993 NARE: factors controlling cloud droplet number concentrations, J. Geophys. Res., accepted, 1996.

Lee, S. C., and C. L. Tien, Optical constants of soot in hydrocarbon flames, Eighteenth Symposium(International) on Combustion, The Combustion Institute, 1159-1166, 1981.

Levine, J. S., Global biomass burning:atmospheric, climate and biospheric implications, Eos, Sept. 11, 1990.

Li, S. M., C. M. Banic, W. R. Leatch, P. S. K. Liu, G. A. Isaac, X. L. Zhou, and Y. N. Lee, Water-soluble fractions of aerosol and their relations to number size distributions based on aircraft measurements from the North Atlantic Regional Experiment, J. Geophys. Res., accepted, 1996.

Lindbergh, J. D. and L. S. Laude, Measurement of the absorption coefficient of atmospheric dust, Appl. Opt., 13, 1923-1927, 1974.

Liu, P. S. K., W. R. Leaitch, C. M. Banic, and S. M. Li, D. Ngo, W. J. Megaw, Aerosol observations at Chebogue Point during the 1993 North Atlantic Regional Experiment: Relationships among cloud concentration nuclei, size distribution, and chemistry, J. Geophys. Res., accepted, 1996.

Malissa, H., H. Puxbaum and E. Pell, Zur Simaltanen RelativKonduktometrischen Kohlenstoff und Schwefelbestimmung in Stauben, Z. Anal. Chem. 282, 109-113, 1976.

McMurry, P. H., and X. Q. Zhang, Size distributions of ambient organic and elemental carbon, Aerosol Science and Technology, 10, 430-437, 1989.

Meador W. E. and W. R. Weaver, Two-stream approximations to radiative transfer in planetary atmospheres: a unified description of existing methods and a new improvement, J. Atmos. Sci., 37, 630-643, 1980.

Mullins, J., and A. Williams, Fuel, 66, P277 , 1987

Noone, K. J., J. A. Ogren, A. Hallberg, H.-C. Hansson, A. Wiedensohler, and E. Swietlicki, A statistical examination of the chemical differences between interstitial and scavenged aerosol, Tellus Ser. B, 44, 581-592, 1992.

Ohta, S., and T. Okita, Measurements of particulate carbon in urban and marine air in Japanese areas, Atmos. Environ., 18, 2439-2445, 1984.

Ogren, J. A., R. J. Charlson, Elemental carbon in the atmosphere: cycle and lifetime., Tellus, 35B, 241-254, 1983.

Ogren, J. A., R. J. Charlson, and P. J. Groblicki, Determination of elemental carbon in rainwater, Anal. Chem. 55, 1569-1572, 1983.

Ogren, J. A., and R. J. Charlson, Wet deposition of elemental carbon and sulfate in Sweden, Tellus, 36B, 225-271,1984.

Palmer, K. F., and D. Williams, Optical properties of water in the near infrared, J. Opt. Soc. Am., 64, 1107-1110, 1974.

Palmer, K. F., and D. William, Optical constants of sulfuric acid; application to the clouds of Venus? Applied Optics, 14, 208-219, 1975.

Parungo, F., C. Nagamoto, M. Zhou, A. D. A. Hansen, and J. Harris, Aeolian transport of aerosol black carbon from China to the ocean, Atmos. Eviron. 28, 3251-3260, 1994.

Paltridge, G. and Platt, C., Radiative Processes in Meteorology and Climatology, volume 5 of Developments in Atmospheric Science. Elsevier Scientific Publishing Co., Amsterdam, 1976.

Patterson, E. M., D. A. Gillette, and B. H. Stockton, Complex index of refraction between 300 and 700 nm for Saharan aerosols, J. Geophys. Res. 82, 3153-3160, 1977.

Penner, J. E., H. Eddleman and T. Novakov, Towards the development of a global inventory for black carbon emissions, Atmos. Eviron. 27A, 1277-1295, 1993.

Pinnick, R. G., G. Fernandez, E. Martinez-Andazola, B. D. Hinds, A. D. A. Hansen, and K. Fuller, Aerosol in the arid southwestern United States: Measurements of mass loading, volatility, size distribution, absorption characteristics, black carbon content, and vertical structure to 7 km above sea level, J. Geophys. Res. 98, 2651-2666, 1993.

Pollack, J. B., B. N. Khare, Optical properties of some terrestrial rocks and glasses, Icarus, 19, 372-389, 1976.

Pusechel R. F. and D.F. Blake et al., Black carbon (soot) aerosol in the lower stratosphere and upper troposphere, Geophysical Research Letters, 19, 1659-1662, 1992.

Roessler, D. M., and F. R. Faxvog, Optoacoustic measurement of optical absorption in acetylene smoke, J. Opt. Soc. Am., 69, 1699-1704,1979.

Roessler, D. M., and F. R. Faxvog, Optical properties of agglomerated acetylene smoke particles at 0.5145μm and 10.6μm wavelengths, J. Opt. Soc. Am., 70, 230-235,1980.

Rosen, H., T. Novakov, and B. A. Bodhaine, Soot in the Arctic, Atmospheric Environment 15, 1371-1374, 1981.

Shah, J. J., and R. L. Johnson, et al., Carbonaceous aerosol at urban and rural sites in the United States, JAPCA, 36, 254-257, 1986

Sisler, J. F. and W. C. Malm, The ralative importance of soluble aerosols to spatial and seasonal trends of impaired visibility in the United States, Atmos. Environ. 28, 5-18, 1994.

Stagg, B. J., and T. T. & Charalampopoulos, Refractive indices of pyrolytic graphite, amorphous carbon, and flame soot in the temperature range 25° to 600°C, Combustion and Flame, 94, 381-396, 1993.

Szkarlat, A. C. and S. M. Japar, Light absorption by airborne aerosols: comparison of integrating plate and spectrophone techniques, Appl. Opt., 20, 1151-1155, 1981.

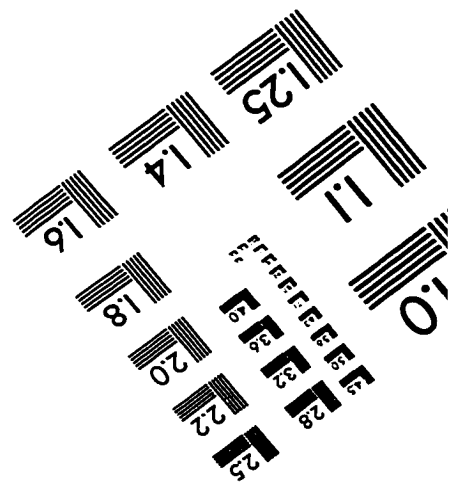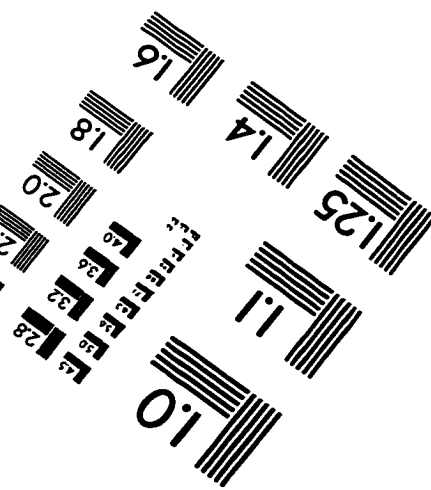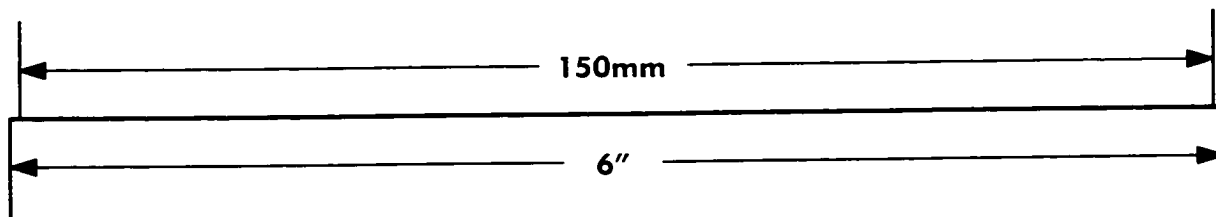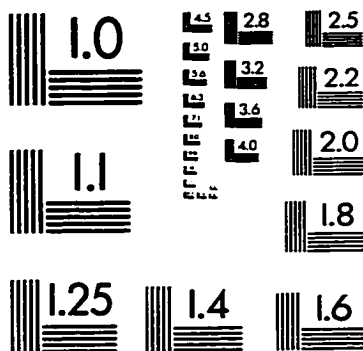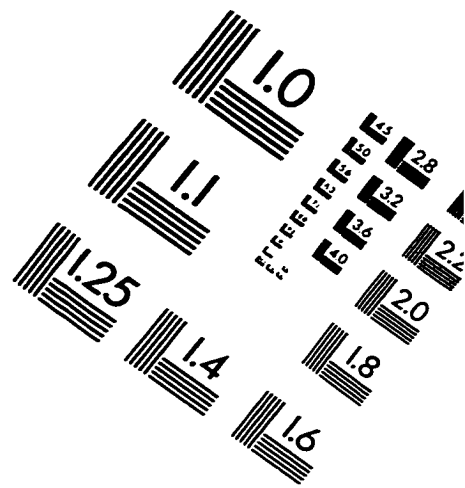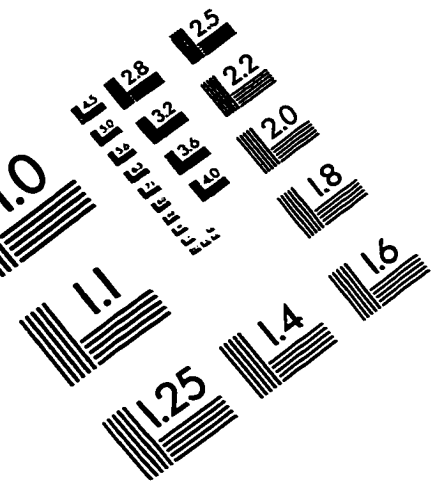Thekaekara, M., Solar energy outside the earth's atmosphere, Solar Energy, 14, 109-127, 1973.

Truex, T. J., and J. E. Anderson, Mass monitoring of carbonaceous aerosols with a spectrophone, Atmos. Environ., 13, 507-509, 1979.

Twohy, C. H., and A. D. Clark et al., Light- absorbing material extracted from cloud droplets and it's effect on cloud albedo, J. Geophys. Res., 94, 8623-8631, 1989.

Vaglieco, B. M., F. Beretta, and A. D'Alessio, In situ evaluation of the soot refractive index in the UV-Visible from the measurement of scattering and extinction coefficients in rich flames, 79, 259-271, 1990.

Valaoras, G., J. J. Huntzicker and W. H. White, Atmos. Environ., 22, 965-971, 1988.

Warneck, P., *Chemistry of the Natural Atmosphere*, Academic Science, 1988.

Warren, S. G. and A. D. Clarke, Soot in the atmosphere and snow surface of Antarctica, J. Geophys. Res., 95, 1811-1816, 1990.

Weiss, R. E. and A. P. Waggoner, Particulate carbon (edited by Wolff G. T. and Klimsch R. L.), Plenum, New York.

Whitby, K. T. Size distribution and physical properties of combustion aerosols. Proc. Conf. on Carbonaceous Particles in the Atmosphere, Lawrence Berkeley Laboratory, Berkeley, California. NTIS document LBL-9037, 1979.

Winter, B., Light Scattering by a sea salt aerosol layer, Master thesis, Dalhousie University, 1994.

Wiscombe, W. J., and G. W. Grams, The backscattered fraction in two-stream approximation, J. Atmos. Sci., 33, 2440-2451, 1976.

Wolff, G. T., N. A. Kelly, et al., Measurement of sulfur oxide, nitrogen oxides, haze and fine particles at a rural site on the Atlantic coast, J. Air Pollut. Control Ass. 36, 585-591, 1986.

Wong, J. G. D., J. T. Kiehl, B. P. Briegleb, and P. Chylek, Effect of relative humidity on the optical properties and radiative forcing of sulfate aerosols, submission to J. Atmos. Sci., 1996.

Wu, H., Black Carbon in polar ice cores: the Palaeo-record of forest fire activity over the past 13,000 years, Master thesis, Dalhouse University, 1992.

IMAGE EVALUATION
TEST TARGET (QA-3)

150mm

6"